THEORETICAL AND NUMERICAL ANALYSIS OF THERMAL RUNAWAY PROPAGATION IN LI-ION BATTERY PACKS

by

DHANANJAY MISHRA

DISSERTATION

Submitted in partial fulfillment of the requirements

For the degree of Doctor of Philosophy at

The University of Texas at Arlington

May 2023

Arlington, Texas

Supervising Committee:

Dr. Ankur Jain (Committee Chairperson)
Dr. Judith Jeevarajan
Dr. Hyejin Moon
Dr. Liwei Zhang
Dr. Sunand Sanathanagopalan

KARTA KARE NA KAR SAKE, GURU KARE SO HOYE
TEEN LOK NOU KHAND MEIN GURU SE BADA NA KOI

ACKNOWLEDGEMENTS

This journey has been a truly amazing and life-changing experience for me. I would like to take this opportunity to express my deepest gratitude to people without whom it would not have been possible.

I wish to express my sincere gratitude to my supervising professor Dr. Ankur Jain. Without his able guidance and supervision, this work would not have been possible. His unparallel expertise in this field motivated me right from the first day of my MAE 5316 class. He has always been too kind, helpful and supportive throughout the journey. He not only inculcated subject matter understanding but also taught me qualities like persistence, perseverance, and patience. In all honesty, it is extremely rare to find someone so learned who would always walk by your side.

I would like to thank Dr. Krishna Shah, Dr. Mohammad Arash Parhizi, Dr. Darshan Ravoori, Dr. Vallabha Rao, Dr. Hardik Prajapati, Dr. Amirhossein Mostafavi, Dr. Swapnil Suryakant Salvi, Dr. Tapesh Joshi, Mr. Raghavender Tummala, Mr. Todd Brigmon, Mr. Francisco Hernandez, Ms. Holly Myers, and everyone at Microscale Thermophysics Laboratory for providing constructive criticism and helping me at various stages of research.

I would like to express my sincere gratitude to Dr. Peng Zhao and Dr. Judith Jeevarajan for collaborations and critical feedbacks. I am thankful to my dissertation committee for their time, guidance, and support. Without their valuable suggestion and advice, I would not have been able to finish my Dissertation.

I dedicate this work to my parents, who supported me mentally, emotionally, and financially throughout the journey.

Financial support from the MAE department at the University of Texas at Arlington is truly appreciated. Without their support, this journey could not have accomplished.

May 1, 2023.

List of figures

Figure 5.6. Color plots showing temperature distribution at multiple times on an XY cross-section plane 1 mm above the top end of cells. Problem parameters correspond to Fig. 4.

Figure 5.7. Impact of combustion modeling: Temperature plots for the case of 2 s venting from a 7 mm2 vent placed at center of top surface of cell 1. (a) and (b) present results for cases in which venting and combustion are both modeled, and in which, only venting is modeled, respectively. In both cases, overhead gap and cell-cell gap are 5 mm and 4 mm, respectively.

Figure 5.8. Effect of location of vent: Temperature plots for 1 mm overhead and cell-to-cell gap, 2 s venting time and 7 mm^2 vent placed at 62.5 mm height on curved surface of trigger cell directly facing cell 2. For comparison, temperature plots for the baseline case are presented in Fig. 7a.

Figure 5.9. Colorplots at different timesteps for the two vent locations presented in Fig. 8.

Figure 5.10. Impact of speed of vent gases: Temperature plots for the case of 2 s venting from a 7 mm2 vent placed at center of top surface of cell 1, with twice the vent speed compared to the baseline case presented in Fig. 7a. Overhead gap and cell-cell gap are 5 mm and 4 mm, respectively.

Figure 5.11. Impact of speed of vent gases: OH concentration colorplots at multiple times on an XY cross-section plane 1 mm above the top end of cells. Problem parameters correspond to Fig. 10.

Figure 5.12. Impact of location of trigger cell: Temperature plots for the case of 2 s venting from a 7 mm2 vent placed at center of top surface of the cell at the center of the pack (cell 13). All other parameters are the same as the baseline simulation.

ABSTRACT

THEORETICAL AND NUMERICAL ANALYSIS OF THERMAL RUNAWAY PROPAGATION IN LI-ION BATTERY PACKS

Dhananjay Mishra, Ph.D.

The University of Texas at Arlington, 2023

Supervising Professor: Dr. Ankur Jain

Strategies to prevent or minimize propagation of thermal runaway in a pack of Li-ion cells are critically needed to ensure safe operation, storage and transportation. While significant literature already exists on thermal runaway simulations, several key questions of practical relevance have remained unaddressed. This work presents multi-mode heat transfer simulations to predict the onset and propagation of thermal runaway in a pack of cylindrical Li-ion cells. The impact of inter-cell gap and thermal properties of the interstitial material on onset and propagation of thermal runaway is studied. It is shown that high interstitial thermal conductivity promotes thermal runaway propagation. However, too low a thermal conductivity results in heat localization in the trigger cell, also leading to thermal runaway. An optimum range of interstitial material thermal conductivity is thus identified. The impact of trigger cell position on propagation is investigated. It is shown that, depending on external conditions, either the center or the corner position may be more susceptible to propagation. Finally, it is shown that radiation and natural convection play a key role in thermal runaway propagation. It is expected that the trade-offs identified here will help minimize the onset and propagation of thermal runaway in Li-ion battery packs.

The venting of hot gases due to rupture of a Li-ion cell during thermal runaway may rapidly transfer thermal energy to neighboring cells in a battery pack and cause propagation of thermal runaway. While thermal runaway has been studied extensively through both measurements and simulations, there is a lack of research on the impact of the venting process on thermal runaway propagation. This work presents a non-linear thermal-fluidic simulation of supersonic turbulent flow of hot gases ejecting from a trigger cell and spreading to neighboring cells. Assuming isentropic flow, temperature and speed of the gas flow as functions of time are estimated based on past measurements. These data are used in simulations to determine the thermal impact of the venting process on neighboring cells. The impact of various geometrical parameters of the battery pack on the spreading of venting gases is investigated. Results indicate that cell-to-cell gap, overhead gap and the location of the vent hole strongly influence the nature of propagation of thermal runaway to neighboring cells. This work develops a fundamental understanding of an important process during thermal runaway and may help in the design and optimization of safe Li-ion battery packs for energy conversion and storage.

Understanding the nature of onset and propagation of thermal runaway in a Li-ion battery pack is critical for ensuring safety and reliability. This paper presents thermal runaway simulations to understand the impact of radiative heat transfer on thermal runaway onset and propagation in a pack of cylindrical Li-ion cells during transportation/storage. It is shown that radiative properties of the internal partition walls between cells commonly found in battery packs for transportation/storage play a key role in determining whether thermal runaway propagation occurs or not. Surface emissivity of the internal partitions is shown to drive a key balance between radiative heat absorbed from the trigger cell and emitted to neighboring cells. It is shown that a high thermal conductivity partition may greatly help dissipate the radiatively absorbed heat, and therefore prevent onset and propagation. Therefore, choosing an appropriate emissivity of the internal partitions may offer an effective thermal management mechanism to minimize thermal runaway. Emissivity of the cells is also shown to play a key role in radiative heat transfer within the battery pack. This work contributes towards the fundamental understanding of heat transfer during thermal runaway in a battery pack and offers practical design guidelines for improved safety and reliability.

Accurate understanding of propagation of thermal runaway is of much importance for developing safe battery pack designs. Combustion of vent gases emerging from a trigger cell undergoing thermal runaway has not been studied in sufficient detail, even though the additional heat generated during combustion likely plays an important role in thermal runaway propagation. This work presents comprehensive numerical modeling and simulation of thermal runaway propagation in a pack of cylindrical cells. The model accounts for multiple coupled non-linear phenomena, including vent gas flow and combustion, radiation, and thermal runaway. Non-premixed combustion of venting gas is modeled using k-ε turbulence model and finite rate chemical kinetics. Simulation results are shown to be in good agreement with experimental data for a benchmark turbulent non-premixed jet flame. Simulations show that hot combustion products are rapidly transported in gaps between cells, leading to self-sustained thermal runaway propagation to adjacent cells. Results demonstrate the critical importance of combustion in determining the nature of propagation of thermal runaway. The vent hole location is identified as an important parameter that influences whether and the extent to which thermal runaway propagation occurs. This work contributes towards the practical understanding of thermal runaway safety of Li-ion battery packs

Thermal runaway in Li-ion cells and battery packs impacts the safety and performance of electrochemical energy conversion and storage systems. Preventing the propagation of thermal runaway in large-scale battery storage and transportation is of much importance. While most of the past work addresses single cells or a small battery pack, only limited literature is available on systems of larger size. This work presents Multiphysics simulations of propagation of thermal runaway during large-scale storage and transportation of Li-ion cells. Through simulations that account for multimode heat transfer, Arrhenius heat generation, turbulent fluid flow and combustion, the propagation of thermal runaway from one pallet of cells to an adjacent pallet is studied. The model quantitatively predicts the temperature field in/around the pallets and predicts whether the adjacent pallet will also catch fire or not. Results indicate that the gap between pallets plays a key role in determining propagation. A sharp threshold value of the gap is found, beyond which, propagation does not occur. Results from this work may be helpful in ensuring thermal safety during large-scale storage and transportation of Li-ion cells, ultimately contributing towards improved electrochemical energy storage and conversion.

TABLE OF CONTENTS

CHAPTER 1

INTRODUCTION

Li-ion cells are used universally for energy conversion and storage in a wide variety of engineering applications. Li-ion cells offer high power density, long cycle life and low self-discharge rate. However, temperature sensitivity of Li-ion cells remains a key technological challenge. When subjected to thermal, mechanical or electrical abuse, such as high temperature, nail penetration or overcharging, Li-ion cells undergo a series of exothermic decomposition reactions, leading to an unsustainable cycle of heat generation and temperature rise, often referred to as Thermal Runaway (TR). Thermal runaway presents serious safety and reliability concerns during the operation, storage and transportation of Li-ion cells. The cell and the battery pack must both be designed to prevent the onset and propagation of thermal runaway. Thermal runaway is known to comprise a series of exothermic decomposition processes, wherein each process generates the heat needed to trigger the next process. Key thermal runaway processes in a Li-ion cell include SEI decomposition, negative and positive electrode decomposition reaction and electrolyte decomposition reaction. Each of these reactions are known to be governed by Arrhenius reaction kinetics, which has been comprehensively studied by experimental and theoretical methods. Thermal modeling and simulations are critical for understanding and mitigating thermal runaway in practical systems, because experimental measurements of thermal runaway in a large battery pack are hazardous, expensive and time-consuming. Due to the non-linear nature of thermal runaway, only a limited number of analytical heat transfer solutions for thermal runaway exist, including a non-dimensional number to predict the onset of thermal runaway,8 non-dimensional analysis of heat transfer during thermal runaway, and semi-analytical thermal modeling of temperature distribution during thermal runaway in realistic conditions. Most of such work is limited to analysis of a single cell, which does not provide sufficient insights into thermal phenomena that may occur when a number of cells are packed together for operation, transportation or storage. In contrast to the limited literature on analytical methods, a wide variety of thermal simulation studies have been presented in the literature. The inherent non-linearity of thermal runaway poses challenges in thermal simulations, particularly when thermal behavior of a large number of cells in a pack is to be studied. A three dimensional lumped thermal abuse model has been developed to predict the spatial distribution of temperature within a battery pack. This work showed that the cell size plays a key role in thermal runaway propagation. Quantitative strategies to prevent thermal runaway propagation in a large format battery pack have been developed using a combination of lumped method simulations and experimental measurements. Cascading propagation of thermal runaway in a battery pack has been studied, showing that pouch cells may be more susceptible than cylindrical cells due to larger area of contact. Statistical distribution of energy released during thermal runaway—an important input parameter for simulations—has been studied. A simulations-based study of the impact of tab configurations, vent locations and intercellular gaps on thermal runaway propagation has been presented. In another study pouch cells were found to propagate more rapidly than cylindrical cells due to greater contact area, and cells connected in parallel showed greater propagation than cells in series. This work also demonstrated the importance of thermal conductivity in deciding the thermal fate of the battery pack. Based on Accelerated Rate Calorimetry and Gaussian approximation curve, a comprehensive numerical model to estimate thermal abuse tolerance of a battery pack has been proposed. A finite-element based electro-thermal runaway model for Lithium Titanate battery pack has been developed for studying the nature of thermal runaway propagation in the pack. Several papers have also investigated various strategies to mitigate the propagation of thermal runaway. A passive strategy for mitigating propagation based on reduction in state of charge and use of metal plates between cells to enhance thermal transport has been presented. A similar mitigation technique by inserting physical barriers of different thermal properties between cells has also been presented. Dividing a large number of cells in a battery pack into smaller groups using thermal barriers has been investigated. A numerical investigation of the extent of thermal runaway mitigation using phase change materials and metal plates around the cell has been presented. An active thermal runaway mitigation system based on conduits and breaches evenly distributed throughout battery pack has also been proposed. Liquid cooling of prismatic cell pack has been shown to prevent thermal runaway. Propagation of thermal runaway in a battery pack, or a group of cells packed together for transportation/storage is likely to be influenced by how the cells are arranged in the pack, properties of the interstitial material and the location of the trigger cell. However, despite the comprehensive literature on thermal simulations on Li ion battery pack in general, there is a lack of robust simulation models that account for all three modes of heat transfer conduction, convection and radiation and predict the impact of such parameters on thermal runaway onset and propagation. The impact of thermal conductivity of the material between cells in a range of thermal abuse conditions has not been sufficiently described. Finally, the impact of the location of the trigger cell in the pack on thermal runaway propagation is also unclear. This work presents a multimodal, non-linear, three-dimensional thermal transport simulation of thermal runaway onset and propagation in an array of cylindrical cells. The simulations account for all three modes of heat transfer between cells, as well as the non-linear Arrhenius kinetics representing multiple exothermic decomposition reactions. The unique contributions of the present work, relative to past literature, include the identification of an optimum range of thermal conductivity of the interstitial material, within which, the risk of both onset and propagation of thermal runaway is lowered. Further, the present work helps understand the impact of the location of trigger cell within the battery pack. The importance of accounting for radiation and natural convection in thermal runaway propagation simulations is also highlighted. This work helps understand the complicated, non-linear interactions between various transport phenomena responsible for the propagation of thermal runaway. This work is expected to be of interest to the battery community since the results obtained here provide practical guidelines for ensuring safety during operation, transportation and storage of Li ion battery packs.

CHAPTER 2

Multi-Mode Heat Transfer Simulations of the Onset and Propagation of Thermal Runaway in a Pack of Cylindrical Li-Ion Cells

Li-ion cells are used universally for energy conversion and storage in a wide variety of engineering applications.[1] Li-ion cells offer high power density, long cycle life and low self-discharge rate.[2] However, temperature sensitivity of Li-ion cells remains a key technological challenge.[3,4] When subjected to thermal, mechanical or electrical abuse, such as high temperature, nail penetration or overcharging, Li-ion cells undergo a series of exothermic decomposition reactions, leading to an unsustainable cycle of heat generation and temperature rise, often referred to as Thermal Runaway (TR).[5,6] Thermal runaway presents serious safety and reliability concerns during the operation, storage and transportation of Li-ion cells. The cell and the battery pack must both be designed to prevent the onset and propagation of thermal runaway. Thermal runaway is known to comprise a series of exothermic decomposition processes, wherein each process generates the heat needed to trigger the next process. Key thermal runaway processes in a Li-ion cell include SEI decomposition, negative and positive electrode decomposition reaction and electrolyte decomposition reaction.[5] Each of these reactions are known to be governed by Arrhenius reaction kinetics, which has been comprehensively studied by experimental and theoretical methods.[5,6] Thermal modeling and simulations are critical for understanding and mitigating thermal runaway in practical systems, because experimental measurements of thermal runaway in a large battery pack are hazardous, expensive and time-consuming.[7] Due to the non-linear nature of thermal runaway, only a limited number of analytical heat transfer solutions for thermal runaway exist, including a non-dimensional number to predict the onset of thermal runaway,[8] non-dimensional analysis of heat transfer during thermal runaway,[9] and semi-analytical thermal modeling of temperature distribution during thermal runaway in realistic conditions.[10] Most of such work is limited to analysis of a single cell, which does not provide sufficient insights into thermal phenomena that may occur when a number of cells are packed together for operation, transportation or storage. In contrast to the limited literature on analytical methods, a wide variety of thermal simulation studies have been presented in the literature. The inherent non-linearity of thermal runaway poses challenges in thermal simulations, particularly when thermal behavior of a large number of cells in a pack is to be studied. A three dimensional lumped thermal abuse model has been developed to predict the spatial distribution of temperature within a battery pack.[11] This work showed that the cell size plays a key role in thermal runaway propagation. Quantitative strategies to prevent thermal runaway propagation in a large format battery pack have been developed using a combination of lumped method simulations and experimental measurements.[12] Cascading propagation of thermal runaway in a battery pack has been studied, showing that pouch cells may be more susceptible than cylindrical cells due to larger area of contact.[13] Statistical distribution of energy released during thermal runaway—an important input parameter for simulations has been studied.[14] A simulations-based study of the impact of tab configurations, vent locations and intercellular gaps on thermal runaway propagation has been presented.[15] In another study highlighting the importance of electrical connectivity and cell form factor, pouch cells were found to propagate more rapidly than cylindrical cells due to greater contact area, and cells connected in parallel showed greater propagation than cells in series.[13] This work also demonstrated the importance of thermal conductivity in deciding the thermal fate of the battery pack. Based on Accelerated Rate Calorimetry and Gaussian approximation curve, a comprehensive numerical model to estimate thermal abuse tolerance of a battery pack has been proposed.[16,17] A finite-element based electro-thermal runaway model for Lithium Titanate battery pack has been developed for studying the nature of thermal runaway propagation in the pack.[18] Several papers have also investigated various strategies to mitigate the propagation of thermal runaway. A passive strategy for mitigating propagation based on reduction in state of charge and use of metal plates between cells to enhance thermal transport has been presented.[19] A similar mitigation technique by inserting physical barriers of different thermal properties between cells has also been presented.[18] Dividing a large number of cells in a battery pack into smaller groups using thermal barriers has been investigated.[20] A numerical investigation of the extent of thermal runaway mitigation using phase change materials and metal plates around the cell has been presented.[21] An active thermal runaway mitigation system based on conduits and breaches evenly distributed throughout battery pack has also been proposed.[22] Liquid cooling of prismatic cell pack has been shown to prevent thermal runaway.[23] Propagation of thermal runaway in a battery pack, or a group of cells packed together for transportation/storage is likely to be influenced by how the cells are arranged in the pack, properties of the interstitial material and the location of the trigger cell. However, despite the comprehensive literature on thermal simulations on Li ion battery pack in general, there is a lack of robust simulation models that account for all three modes of heat transfer conduction, convection and radiation and predict the impact of such parameters on thermal runaway onset and propagation. The impact of thermal conductivity of the material between cells in a range of thermal abuse conditions has not been sufficiently described. Finally, the impact of the location of the trigger cell in the pack on thermal runaway propagation is also unclear. This paper presents a multimodal, non-linear, three-dimensional thermal transport simulation of thermal runaway onset and propagation in an array of cylindrical cells. The simulations account for all three modes of heat transfer between cells, as well as the non-linear Arrhenius kinetics representing multiple exothermic decomposition reactions. The unique contributions of the present work, relative to past literature, include the identification of an optimum range of thermal conductivity of the interstitial material, within which, the risk of both onset and propagation of thermal runaway is lowered. Further, the present work helps understand the impact of the location of trigger cell within the battery pack. The importance of accounting for radiation and natural convection in thermal runaway propagation simulations is also highlighted. This work helps understand the complicated, non-linear interactions between various transport phenomena responsible for the propagation of thermal runaway. This work is expected to be of interest to the battery community since the results obtained here provide practical guidelines for ensuring safety during operation, transportation and storage of Li ion battery packs.

2.1.1 Geometry

The simulation geometry is shown schematically in Fig. 1a. Finite-volume simulations are carried out on a 5 by 5 array of 18650 cells surrounded by an interstitial material with a uniform gap between cells. A 1 mm thick heater is wrapped around one of the cells, referred to as the trigger cell. Joule heating in the heater triggers thermal runaway. The entire array of cells is placed inside a box, with 2.5 mm clearance between the cells and the box. The simulations account for temperature-dependent heat generation due to decomposition reactions coupled with thermal conduction through all materials, natural convection in the air around the cells, as well as cell-to-cell heat transfer due to radiation. Several of these processes are highly non-linear. In contrast to prismatic cells, where a one dimensional simulation is often possible, the cylindrical geometry of cells considered here necessitates a three-dimensional simulation. The governing equations for each of these phenomena are described below in detail.

2.1.2 Governing equations

Heat generation due to four specific decomposition reactions are considered SEI decomposition, negative-solvent reaction, positive-solvent reaction and electrolyte decomposition. Arrhenius expressions for heat generation for each reaction are assumed, as listed in Table I. [24] These expressions account for reactant consumption as the reaction proceeds. Values for various parameters appearing in the heat generation equations are taken from Kim, et al.[11] and listed in Table II. Joule heating in the 1 mm thick heater around the trigger cell due to heating current is modeled as a volumetric heat source.

2.1.3 Thermal conduction

Amongst the three modes of heat transfer, thermal conduction is relatively the easiest to model. The transient energy equation governing thermal conduction in each cylindrical cell is given by

$$\frac{\partial}{\partial \mathrm{x}}\left(\frac{\partial \mathrm{T}}{\partial \mathrm{x}}\right)+\frac{\partial}{\partial \mathrm{y}}\left(\frac{\partial \mathrm{T}}{\partial \mathrm{y}}\right)+\frac{\partial}{\partial \mathrm{z}}\left(\frac{\partial \mathrm{T}}{\partial \mathrm{z}}\right) = \frac{\rho \mathrm{c_p}}{\mathrm{k}}\frac{\partial \mathrm{T}}{\partial \mathrm{t}} \tag{1}$$

Amongst the three modes of heat transfer, thermal conduction is relatively the easiest to model. The transient energy equation governing thermal conduction in each cylindrical cell is given by

$$\frac{1}{\mathrm{r}}\frac{\partial}{\partial \mathrm{r}}\left(\mathrm{k_r}\mathrm{r}\frac{\partial \mathrm{T}}{\partial \mathrm{r}}\right)+\frac{\mathrm{k}_\theta}{\mathrm{r}^2}\frac{\partial^2 \mathrm{T}}{\partial \theta^2}+\mathrm{k_z}\frac{\partial^2 \mathrm{T}}{\partial \mathrm{z}^2}+\mathrm{q}''' = \rho \mathrm{c_p}\frac{\partial \mathrm{T}}{\partial \mathrm{t}} \tag{2}$$

Unlike the Li-ion cell, thermal conductivity of the interstitial material is taken to be isotropic.

2.1.4 Natural convection

Due to the large temperature rise expected on cell surfaces because of thermal runaway, buoyancy-driven natural convection heat transfer may be important to model, even though the time scale for natural convection is probably much larger than the time scale available during thermal runaway. Natural convection is modeled by turning on gravitational effects and implementing a temperature-dependent density of air, which results in convective flow driven by the temperature difference between hot surfaces and the ambient. Convection is, of course, not relevant if the interstitial material between cells is solid. The conservation equations governing convective flow and heat transfer due to natural convection is

$$\frac{\partial \rho}{\partial t} + \nabla.(\rho \mathbf{V}) = 0 \tag{3}$$

$$\rho\left(\frac{\partial \mathbf{V}}{\partial t} + (\mathbf{V}.\nabla \mathbf{V})\right) = -\nabla.p + \mu \nabla^2 \mathbf{V} + \rho \mathbf{g} \beta (T - T_\infty) \tag{4}$$

$$\frac{\partial T}{\partial t} + \mathbf{V}.\nabla T = \alpha \nabla^2 T \tag{5}$$

where viscous effects are neglected in the energy equation due to low velocity of air. Note that the $g \cdot \beta(T - T\infty)$ term in Eq. 4 drives natural convection due to change in density with temperature. Here, β is the volumetric thermal expansion coefficient, which quantifies the rate at which the density of air changes with temperature at constant pressure. By treating air to be an ideal gas, β can be shown to be given by

$$\beta = -\frac{1}{\rho}\frac{\Delta \rho}{\Delta T} = \frac{1}{\rho}\frac{p}{R_u T^2} = \frac{1}{T} \tag{6}$$

2.1.5 Radiation

Similar to natural convection, radiative heat transfer between cells may be an important heat transfer mode due to the large temperature rise expected in the battery pack when thermal runaway occurs. Implementation of radiative heat transfer in the simulation is carried out using the surface-to-surface radiation model in ANSYS Fluent. In this model, radiation exchange between any pair of surfaces within the simulation geometry is governed by the view factor, which accounts for the sizes, separation distance and relative orientation of the two surfaces. The energy flux leaving a surface is composed of emitted energy by virtue of temperature and reflected energy, which is dependent on irradiation flux from surroundings. For any surface i, the amount of energy leaving the surface is[26]

$$q_{out,i} = \varepsilon_i \sigma T_i^4 + b_i q_{in,i} \tag{7}$$

where ei and bi are the emissivity and reflectivity, respectively, of the i th surface, and s is the Boltzmann constant. qin,i is the irradiation flux incident on the surface from the surroundings, which is given by the net sum of energy incident from all other surfaces based on the view factors fji as follows:

$$A_i \cdot q_{in,i} = \sum_{j=1}^{N} A_j \cdot q_{out,j} \cdot f_{ji} \tag{8}$$

$$q_{out,i} = \varepsilon_i \cdot \sigma T_i^4 + b_i \cdot \sum_{j=1}^{N} f_{ij} \cdot q_{out,j} \tag{9}$$

Thus, total radiation flux from a surface comprises of Stefan Boltzmann emission from the surface and sum of the radiation fluxes intercepted and reflected by virtue of other surfaces in the visible surroundings. This radiation flux is included as a heat input term for each cell in computing the energy equation. View factors play a key role in the radiative heat transfer modeling approach used in this work, and are calculated for each face pair in the geometry using ray tracing method.27 In this method, a large number of rays are fired from points on a given object at various angles, and the first object that each ray intersects is recorded. The view factor between any two objects is then computed as the fraction of rays leaving the first object and intersecting the second. For the purposes of simulation of radiative heat transfer, all surfaces in the simulation geometry are considered to be gray and diffuse, with an emissivity of 0.1. The low value of emissivity is justified by the shiny, metallic surface finish of most Li-ion cells, resulting in high reflectivity and low emissivity.

2.2 Meshing and other simulation details

3D polyhedral meshing is used for all simulations in this work due to high resolution and low meshing time compared to other meshing techniques. Surface meshing is carried out with local sizing of 1 cell per gap, scoped to faces, selected by labels and proximity size control type. Volume meshing comprises polyhedral elements with 1.2 growth rate, 30° mesh feature angle and 0.9 quality warning limit. Upwards of 10 Million elements are used in the mesh for the 25-cell geometry, with a maximum orthogonal quality of 0.43. The squish index of the meshing, which characterizes polyhedral mesh quality is 0.31. A solver with fixed time advancement technique with 0.001 s step size and 500 maximum iterations per time step is used with total simulation time being 1000 s. A representative cross-section showing the mesh is presented in Fig. 1b. A comprehensive mesh sensitivity analysis is carried out prior to actual simulations in order to determine the minimum spatial discretization and time step needed to obtain grid-independent results. This analysis is carried out by refining the spatial meshing or time step, one at a time, until the results do not change significantly with further refinement. Relative tolerance for each iteration is set as 0.001. 500 energy iterations per timestep and 3000 faces per surface cluster are used. Thermal conductivity of each cell is treated to be orthotropic, with values of 0.2 $Wm^{-1} K^{-1}$, 32 $Wm^{-1} K^{-1}$ and 32 $Wm^{-1} K^{-1}$ in the radial, axial and circumferential directions, respectively, based on past measurements.28 Density and heat capacity are taken to be 2280 kg m^{-3} and 715 J $kg^{-1} K^{-1}$, [24] respectively, also based on past measurements.[24,28] The baseline interstitial material around cells is taken to be air, which is modeled as an incompressible ideal gas, with constant viscosity, specific heat and thermal conductivity. Variations in the thermal conductivity of the interstitial material are considered in simulations discussed in the next section.

2.3 Results and discussion

2.3.1 Simulation validation

The simulation set up described in the previous Section is validated in multiple ways. Due to the complicated, non-linear nature of the simulation, several elements of the simulation, such as Arrhenius heat generation and radiative heat transfer are validated separately. In order to validate the radiation modeling approach, a radiative heat transfer problem with a simpler but representative geometry is considered. As shown in the inset in Fig. 2, a single cylinder of radius R in located inside a rectangular box of size L by W. The distance between one of the walls and the center of the cylinder is w. For this simplified geometry, the radiative heat exchange between the left wall and cylinder is given by

$$q''_{\mathrm{cyl-wall}} = \frac{1}{\pi}\tan^{-1}\left[\frac{L}{2(w+R)}\right]\sigma\left[T_{\mathrm{cyl}}{}^{4} - T_{\mathrm{wall}}{}^{4}\right] \tag{10}$$

where L is the length of wall and w is the distance between wall and cylinder. Figure 2 presents a comparison of the theoretical radiative heat transfer based on Eq. 10 and one computed using the view factor determined from the ray tracing method described in the previous Section. This comparison, presented as a function of w/W shows that as w/W increases, the radiative flux reduces, as expected, due to the greater distance between the cylinder and the wall. There is excellent agreement between the numerical calculation of the radiative heat flux and the theoretical curve throughout the w/W range. While the single-cylinder geometry used here for validation is fairly simple, it is reasonably representative of the geometry used in actual simulations while still allowing an analytical solution that the numerical calculations can be compared against. Unlike radiation, a well-known theoretical solution is not readily available that can be compared with the simulation's computation of natural convection while still maintaining a geometry representative of a battery pack. Instead, the velocity field computed by the simulation is plotted in order to confirm that natural convection effects are indeed being accounted for by the simulation model. These velocity color plots are shown in Fig. 3 over a cross-section at three different times for a representative simulation. The left-most cell is the trigger cell, and the cell-to-cell gap is 4 mm. Velocity field is plotted only in the air outside the cells, since there is no convection inside the cells. Figure 3 clearly shows generation of a natural convection velocity field over time. Initially, the velocity field is generated in the gap next to the trigger cell due to the high temperature of the walls of the trigger cell. As time passes and thermal runaway takes place in the trigger cell, the cell walls become even hotter, which increases the driving force behind natural convection. This is clearly seen in Figs. 3b and 3c where the natural convection flow spreads out and even propagates downwards in the gap between other cells. Note that Fig. 3 plots the velocity magnitude, and note its direction. For further validation of the computational approach used in this work, results from a single-cell simulation are compared with a semi-analytical model available from the literature.10 For a single cylindrical cell of 18650 configuration with convective cooling on the outer surface, a semi-analytical model based on discrete time stepping and the use of a closed-form temperature solution in each timestep has been presented in the past.10 Four decomposition reactions are modeled in the cell in addition to a fixed Joule heating current for triggering thermal runaway. Under these conditions, numerical simulation is carried out to determine the temperature at the core of the cell as a function of time. Radiation and natural convection are switched off, since the semi-analytical model used for comparison does not account for these effects.10 Figure 4 presents comparison of the numerical simulation with the semi analytical model. Core temperature as a function of time is plotted in Fig. 4a, while reactant concentration parameters are plotted in Fig. 4b. In both cases, there is excellent agreement between the two. Temperature rises slowly at first while the cell is being heated up by Joule current before the exothermic decomposition reactions take over, resulting in very rapid temperature rise. Soon, however, the decomposition reactions fade away due to consumption of reactants, resulting in a gradual reduction in temperature seen in Fig. 4a. The consumption of reactants can be seen clearly in Fig. 4b. The good agreement between numerical simulation results and the semi-analytical model from past work, even though for a simplified geometry, provides further validation of the numerical simulation framework described in Section 2.

2.3.2 Effect of cell gap on TR propagation

The effect of parameters external to the cell on thermal runaway propagation is investigated first. Two key parameters of specific interest are cell-to-cell gap and thermal conductivity of the interstitial material around the cells. Figure 5 presents colormaps of computed temperature distribution at three different times for two cases where the cell-to-cell gap is 4 mm and 1 mm, respectively. A plot of core temperature of the cells as functions of time is presented in Fig. 6. Recognizing the symmetry in the problem, temperatures of only cells in the right half of the geometry are plotted. For cell numbers used in Fig. 6, please refer to the numbering scheme shown in Fig. 5. In these simulations, the thermal conductivity of the interstitial material is held constant at k = 0.02 Wm−1 K−1 (roughly corresponding to air) and the trigger cell is located at a corner. A heating rate of 4 × 105 Wm−2 up to 400 s is implemented in the sleeve heater around the trigger cell. Figures 5 and 6 show two very different outcomes of the battery pack, depending on the value of the cell-to-cell gap. When the cell to-cell gap is 1 mm, the small thermal resistance offered by the interstitial material results in sufficient heat transfer from the trigger cell to its neighbors to cause propagation of thermal runaway, first from the trigger cell to its neighbors and eventually into the entire battery pack. In contrast, a cell-to-cell gap of 4 mm offers large enough thermal resistance and suppression of heat transfer that propagation of thermal runaway does not occur, even though there is some temperature rise in the neighboring cells, as evident from Fig. 6a. Note that the tipping point in the cell-to-cell gap to prevent thermal runaway propagation, which lies between 1–4 mm in this case, depends on various problem parameters, including the thermal conductivity of the interstitial material (0.02 Wm−1 K−1 in this case), the cell size (18650 configuration in this case), the heat generation mechanisms for thermal runaway (standard, four-reaction model as summarized in Table I), etc. For other values of these parameters, the critical value of the cell-to-cell gap will vary and must be calculated separately. Note that the thermal behavior seen in Figs. 5 and 6 represents fairly strong sensitivity of thermal runaway propagation on cell-tocell gap. In practical scenarios of low-cost transportation and storage, it is quite possible that the cell-to-cell gap cannot be controlled to this degree of accuracy as ambient conditions around the cell change, for example, during air transportation of cells. The effect of thermal conductivity of the interstitial medium is investigated next.

2.3.3 Effect of thermal conductivity of interstitial material on TR propagation

In addition to the cell-to-cell gap, thermal conductivity of the interstitial material also impacts thermal conduction from the trigger cell to its neighbors, and therefore, is expected to play a key role in thermal runaway propagation. High value of thermal conductivity may facilitate more heat transfer to neighboring cells, which may cool down the trigger cell, possibly helping to stop the onset of thermal runaway, but may also increase the heat absorbed by neighboring cell, causing propagation of thermal runaway. The opposite is true for low values of thermal conductivity—in this case, neighboring cells may remain thermally shielded from the trigger cell, but, low thermal conductivity also enhances the possibility of onset of thermal runaway by concentrating heat within the trigger cell. These arguments suggest that there may be an optimal window of thermal conductivity of the interstitial material, below or above which, there may be greater likelihood of thermal runaway onset and propagation. A series of simulations are carried out on a 5 by 5 cell matrix in order to systematically investigate these issues. In these simulations, the cell-to-cell gap is held constant at 4 mm, and the trigger cell is always at the corner (Cell 1). Since the trigger cell may experience different amounts of thermal abuse in realistic conditions, two distinct scenarios are considered. In Scenario 1, a heating rate of 4×10^5 Wm^{-2} up to 400 s is considered, along with a value of $h = 10$ Wm^{-2} K^{-1} for the external convective heat transfer coefficient. Within these parameters, simulations are carried out for two values of interstitial thermal conductivity—0.02 Wm^{-1} K^{-1} and 0.3 Wm^{-1} K^{-1} . Results are shown in Figs. 7a and 7b, respectively, in the form of peak temperatures of each cell plotted as functions of time. These results indicate that low thermal conductivity causes thermal localization within the trigger cell, leading to onset of thermal runaway in the trigger cell. Once thermal runaway is initiated, the large amount of heat generated causes propagation into neighboring cells. On the other hand, when the thermal conductivity is 0.3 Wm^{-1} K^{-1} , there is greater heat spreading from the trigger cell. In this case, as shown in Fig. 7b, there is some temperature rise in the trigger cell as well as its neighbors, but not enough to cause thermal runaway. Therefore, under the abuse conditions of Scenario 1, a larger thermal conductivity is desirable. However, this may not be generalized to all possible abuse conditions. A second set of abuse conditions, Scenario 2 is considered, with 5 × 105 Wm^{-2} heating up to 400 s, along with adiabatic boundary conditions on the outside of the battery pack. This represents a greater thermal abuse than Scenario 1. In this case, simulations are carried out for thermal conductivity values of 0.3 Wm^{-1} K^{-1} and 0.6 Wm^{-1} K^{-1} . The resulting temperature curves for cells in the pack are plotted in Figs. 7c and 7d, respectively. These results show a behavior that is opposite of Scenario 1. In this case, the lower value of thermal conductivity causes sufficient reduction in thermal conduction that thermal runaway does not propagate, despite the trigger cell entering thermal runaway, as seen in Fig. 7c. At the higher value of thermal conductivity considered here, Fig. 7d shows that the increased thermal conduction in this case results in propagation of thermal runaway eventually into all cells of the battery pack. These results indicate that a low value of thermal conductivity may be desirable for some thermal abuse conditions, but undesirable for others. An intermediate value of thermal conductivity, such as the 0.3 Wm^{-1} K^{-1} case considered here, appears to present a reasonable balance by preventing propagation of thermal runaway in both scenarios considered here. Therefore, an intermediate value of thermal conductivity of the interstitial material is likely to be most effective in preventing propagation of thermal runaway across a range of abuse scenarios. This desirable, intermediate range of thermal conductivity may be specific to other conditions, such as cell-to-cell gap and cell chemistry, and therefore, may need to be determined specifically for each battery pack. Nevertheless, the existence of this optimal range of thermal conductivity, as demonstrated by simulations described above, is interesting and highlights the critical influence of thermal conductivity of the interstitial material on thermal runaway propagation.

2.3.4 Effect of trigger cell propagation on TR propagation

It is of interest to determine whether thermal runaway propagation is affected by the location of the trigger cell in the battery pack. Two competing considerations appear to be relevant for determining the impact of the trigger cell location. First, if the trigger cell is located at the corner or edge of the battery pack, then it has easier access to external cooling such as convection available on the boundary of the battery pack. In contrast, heat removal from a trigger cell located in the center is much more difficult, and most of the heat is likely to be distributed to the neighboring cells. However, the second consideration is that when located in the center, the trigger cell has more neighbors, and therefore, the heat gained by each neighbor may be lower, thereby lowering the risk of thermal runaway propagation. In contrast, when the trigger cell is located at the corner or along the edge, the fewer number of neighboring cells results in greater heat absorbed by each, and therefore, a greater risk of thermal runaway propagation into the neighbors. The outcome of this trade-off most likely depends on the specific values of parameters such as cell-to-cell gap, interstitial thermal conductivity, heat rate, etc. Numerical simulations are carried out in order to quantitatively investigate these competing considerations and determine if the corner or center location of the trigger cell is preferable to avoid thermal runaway propagation. Two simulations are carried out with the trigger cell either in the center or on the corner of a 5 by 5 array, with a cell-to-cell gap of 4 mm and interstitial thermal conductivity of 0.02 $\mathrm{Wm^{-1}\ K^{-1}}$. A heating rate of $4 \times 10^5\ \mathrm{Wm^{-2}}$ in the sleeve heater up to 400 s is considered along with Arrhenius heat generation for decomposition reactions as summarized in Table I. Under these conditions (Scenario A), Figs. 8 and 9 present temperature colormaps and plots of cell temperatures as functions of time for the two different positions of the trigger cell. These results clearly show that the case with trigger cell in the center sees thermal runaway propagation, with eventual spread to the entire battery pack. On the other hand, thermal runaway is limited only to the trigger cell when located on the corner. These results indicate that under the specific parameters values used here, the effect of closer access to external cooling plays a critical role in preventing the propagation of thermal runaway in the corner trigger cell case. While Figs. 8 and 9 suggest a greater likelihood of propagation from a trigger cell at the center of the pack, this result is by no means universal. It may be possible that the balance between the two competing factors governing thermal runaway propagation may tilt differently in a different thermal abuse scenario. Figures 10 and 11 present results from a similar investigation of the impact of trigger cell location, but with more restricted external cooling conditions. In this case, cell-to-cell gap and interstitial thermal conductivity are the same as Figs. 8 and 9, but heating rate is $3 \times 10^5\ \mathrm{Wm^{-2}}$ and the external boundaries are adiabatic. In this case (Scenario B), Figs. 10 and 11 show that thermal runaway propagation now occurs in the corner trigger cell case but not in the center trigger cell case. Clearly, reduction in the external convective heat transfer coefficient reduces the advantage of the corner trigger cell seen in Figs. 8 and 9. This makes it more likely for thermal runaway to propagate from the corner trigger cell, which shares its heat with a fewer number of neighbors than the center trigger cell, thereby leading to more temperature rise per neighbor.

2.3.5 Impact of radiation and free convection heat transfer

The computational framework developed for simulations described above combines three non-linear thermal processes Arrhenius heat generation, radiation and natural convection—into a single simulation. Inclusion of these non-linear processes likely makes the simulation results more accurate and realistic than if these processes were not modeled. However, the complex interaction between these non-linear processes also makes the computations challenging and increases the computation time. In order to optimize these simulations, it is of interest to determine whether any of these processes can be reasonably neglected, thereby saving on computational cost. While Arrhenius heat generation must clearly be accounted for in any thermal runaway simulation, a set of simulations are carried out to determine the impact of neglecting radiation and natural convection on the accuracy of simulation results. Both radiation and natural convection enhance the rate of heat transfer between cells, and therefore, it is important to understand whether these modes of heat transfer are sufficient to influence the propagation of thermal runaway. In the first set of simulations, the effect of modeling radiative heat transfer is determined. For a representative set of parameter values, Figs. 12a and 12b plot temperature curves for each cell in the pack with and without radiation modeling, respectively. A comparison of these plots shows that the battery pack undergoes severe thermal runaway when radiation is modeled. On the other hand, neglecting radiation leads to a prediction of onset in the trigger cell but no propagation. This shows that radiation modeling is of critical importance, and that neglecting radiation may result in an erroneous prediction of no thermal runaway propagation, when, in fact, propagation may occur. This can, of course, be dangerous from a safety perspective. Similarly, the effect of natural convection, which also facilitates cell-to-cell heat transfer is also characterized. Two simulations—with and without natural convection—are carried out while all other problem parameters are held constant. Natural convection is turned off by setting the value of β to be zero. Figure 13 compares temperature rise as a function of time for full-scale simulations with the one without natural convection. Thermal runaway is found to propagate both with and without natural convection. However, when natural convection is not modeled, a milder propagation is predicted. For example, as shown in Fig. 13a, the neighboring cells 2 and 7 enter thermal runaway roughly 40 s and 90 s after runaway in the trigger cell when natural convection is modeled. In contrast, when natural convection is not accounted for, the reduced inter-cell heat transfer causes a delay in thermal runaway propagation, so that cells 2 and 7 now enter thermal runaway 95 s and 310 s after runaway in the trigger cell, as shown in Fig. 13b. This indicates that neglecting natural convection is also undesirable. Even though neglecting natural convection does not result in the incorrect prediction of no propagation, it still incorrectly predicts a slow propagation of thermal runaway.

List of figures

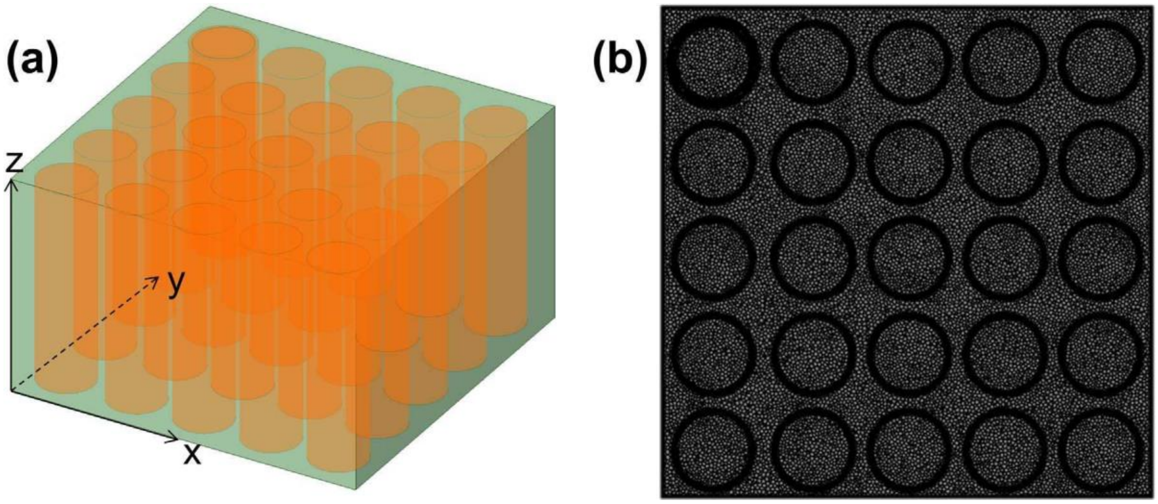

Figure 1. Schematic of 18650 Li-ion battery pack containing 25 cells: (a) Geometry of battery pack with trigger cell at position 1 and intercellular gap of 4 mm. (b) Cross sectional view of the 3D tetrahedral meshing elements used in the simulation.

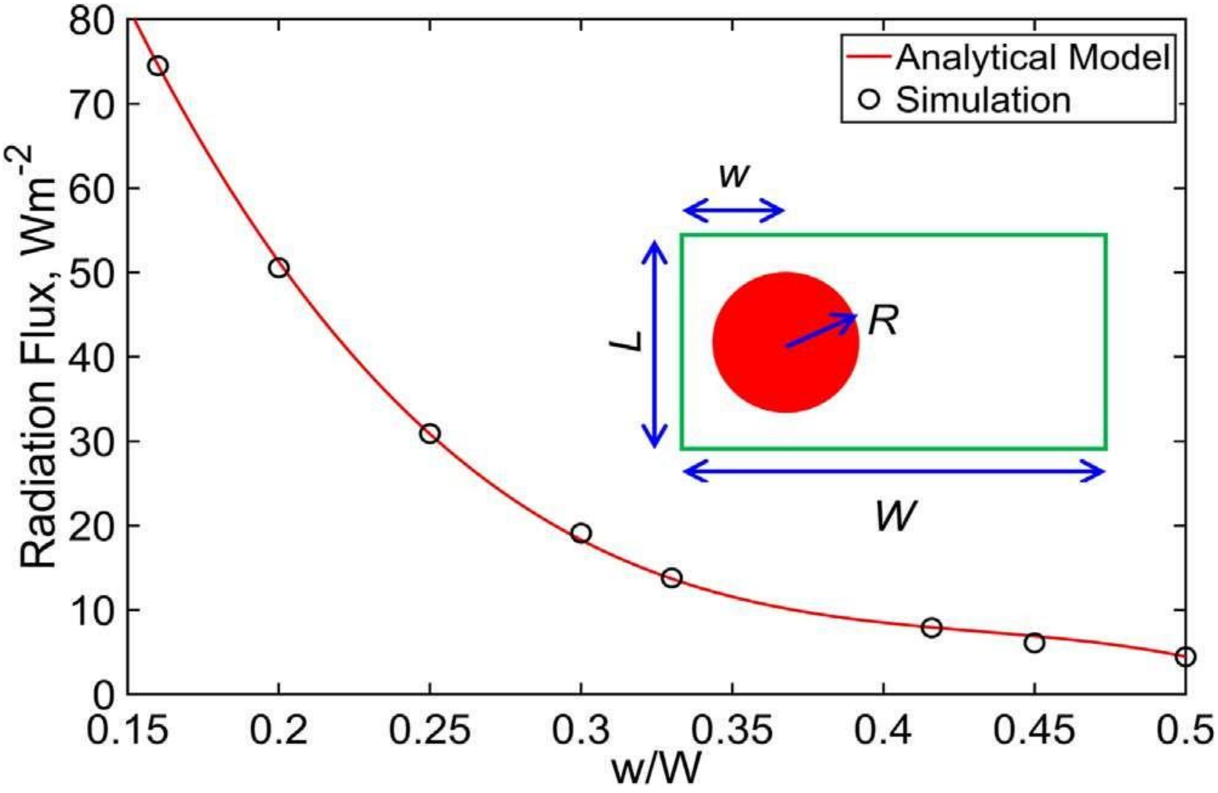

Figure 2. Validation of simulation results against analytical model for surface-to-surface radiation modeling: (a) Radiation flux intercepted by cell at 298 K temperature located inside a box from the left wall at 373 K temperature as a function of w/W. A geometrical schematic is shown as an inset.

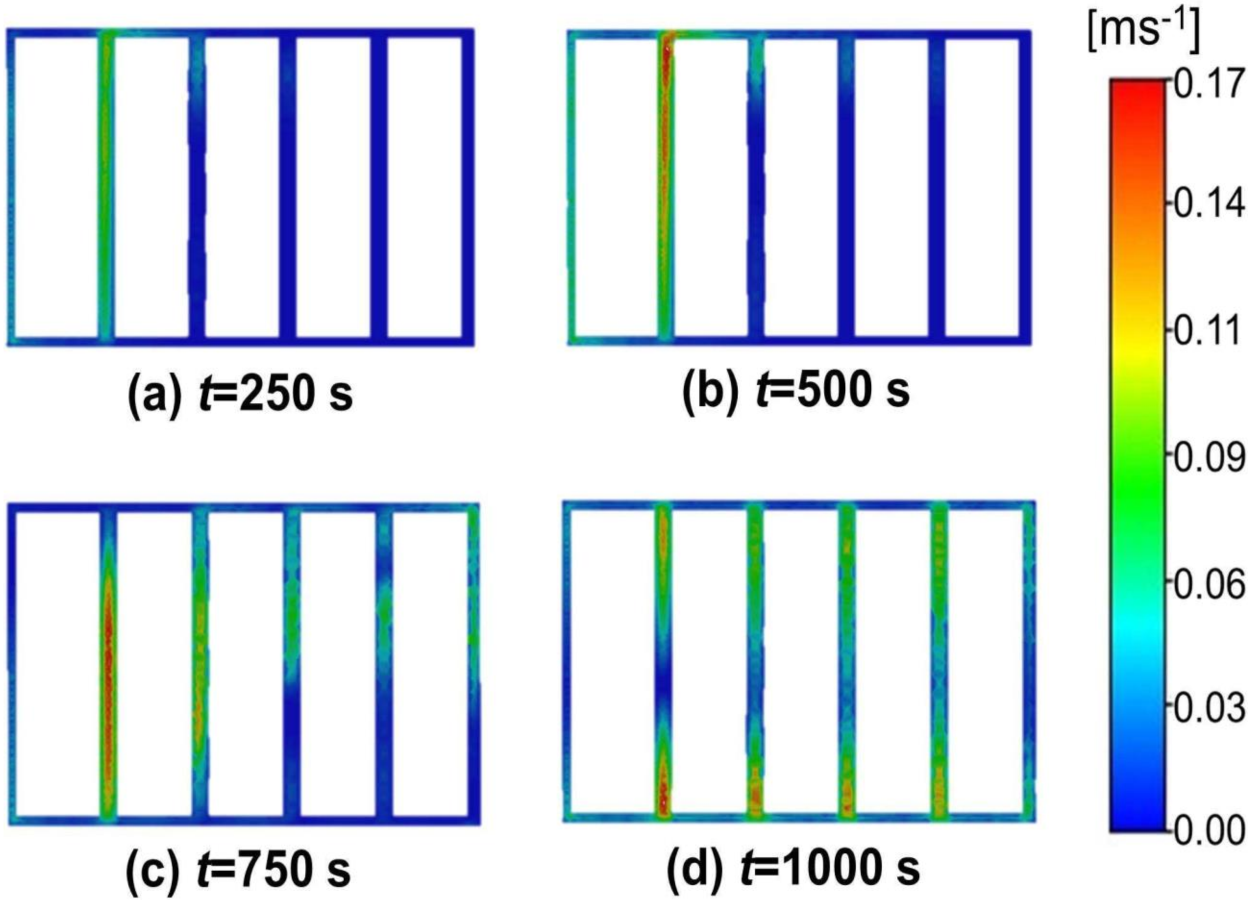

(a) *t*=250 s

(b) *t*=500 s

(c) *t*=750 s

(d) *t*=1000 s

Figure 3. Velocity colormap at different time steps to demonstrate establishment of convective flow and heat transfer between cells as simulation progresses: (a) 250 s, (b) 500 s, (c) 750 s, (d) 1000 s. These color- maps are shown on a cross-section across five cells, where the left-most cell is the trigger cell, and the cell-to-cell gap is 4 mm.

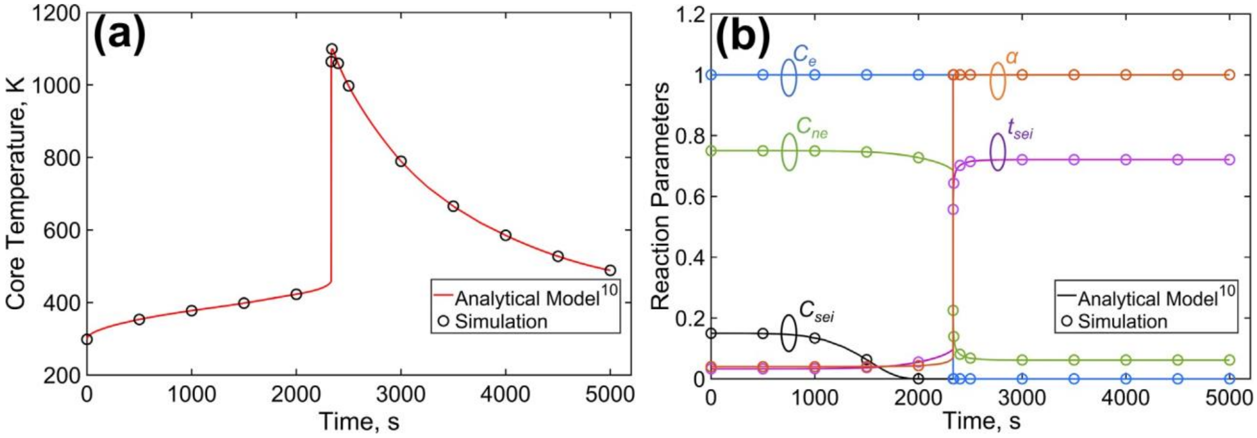

Figure 4. Validation of simulations against analytical model[10] for thermal runaway onset in response to convective heat transfer from a heater ambient maintained at 423 K: Plots of (a) temperature, and (b) various reactant concentration parameters as functions of time during a thermal runaway event.

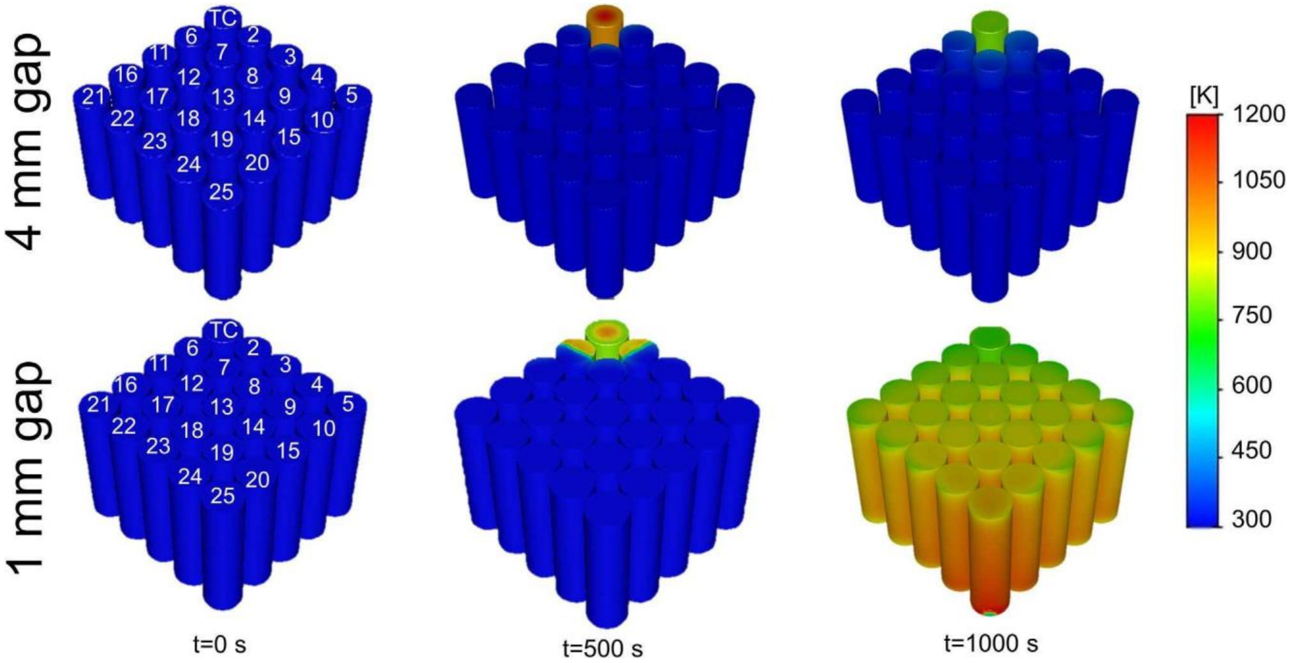

Figure 5. Effect of cell-to-cell gap on thermal runaway propagation: Temperature contours at three specific times during a thermal abuse event for two different values of the cell-to-cell gap. Thermal conductivity of the interstitial material is 0.02 $Wm^{-1}K^{-1}$ and heating rate is 4×10^5 Wm^{-3} for 0–400 s.

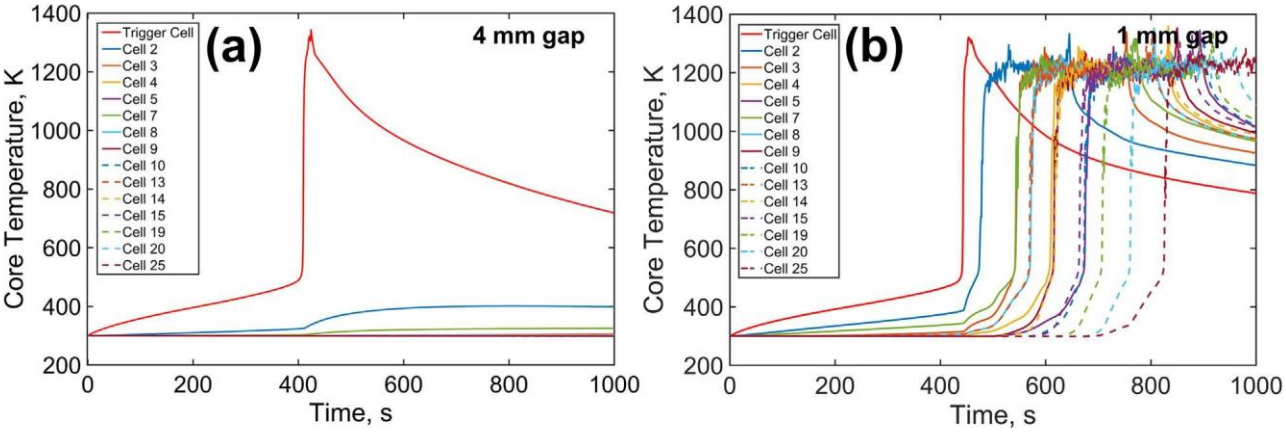

Figure 6. Temperature vs time plots for each cell for the scenario considered in Fig. 5 with cell-to-cell gap of (a) 4 mm, (b) 1 mm.

Scenario 1

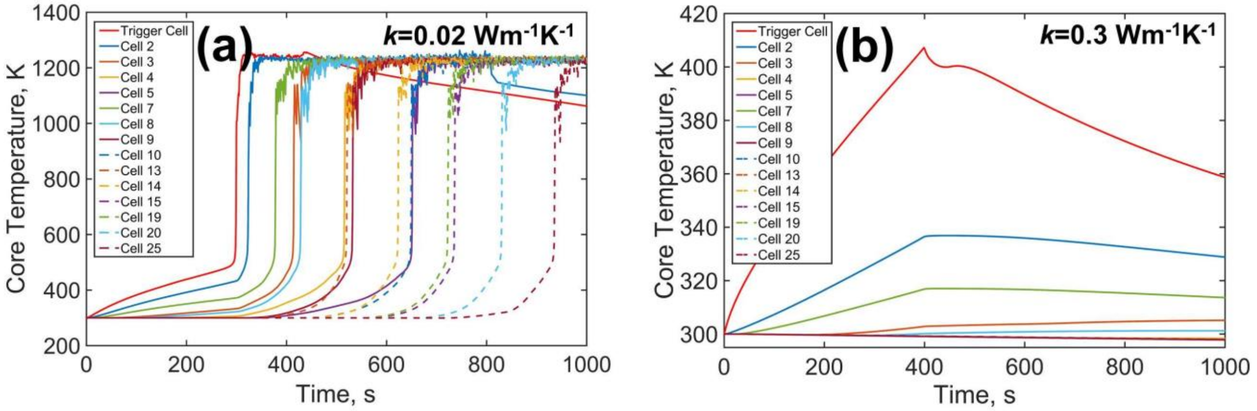

Scenario 2

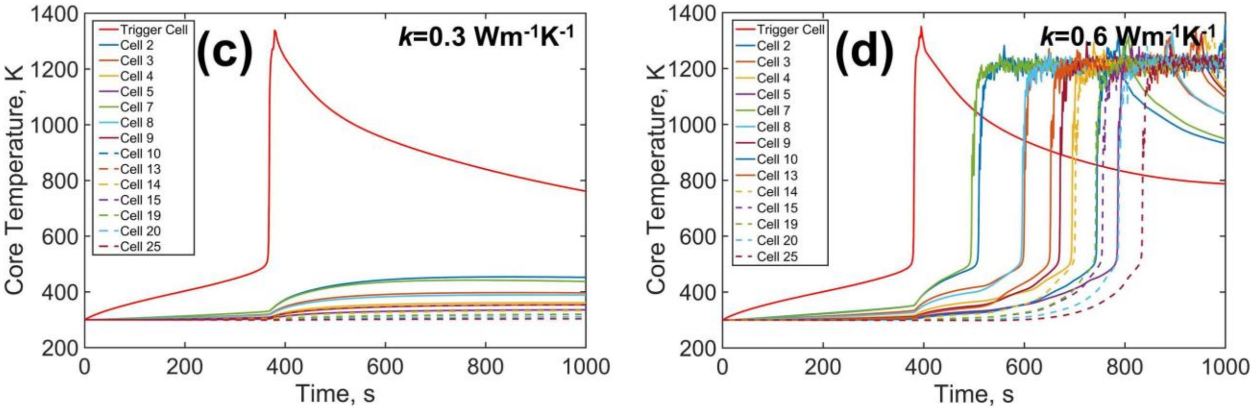

Figure 7. Temperature contours for investigating the effect of thermal conductivity of the interstitial material: (a) and (b) present plots for $k = 0.02$ Wm^{-1} K^{-1} and $k = 0.3$ Wm^{-1} K^{-1} under Scenario 1 (heating rate of 4×10^5 Wm^{-2} for 0–400 s and external convective heat transfer coefficient of 10 W/m^{2}K); (c) and (d) present plots for $k = 0.3$ Wm^{-1} K^{-1} and $k = 0.6$ Wm^{-1} K^{-1} under Scenario 2 (heating rate of 5×10^5 Wm^{-2} for 0–400 s and external convective heat transfer coefficient of 0 Wm^{-2} K^{-1}).

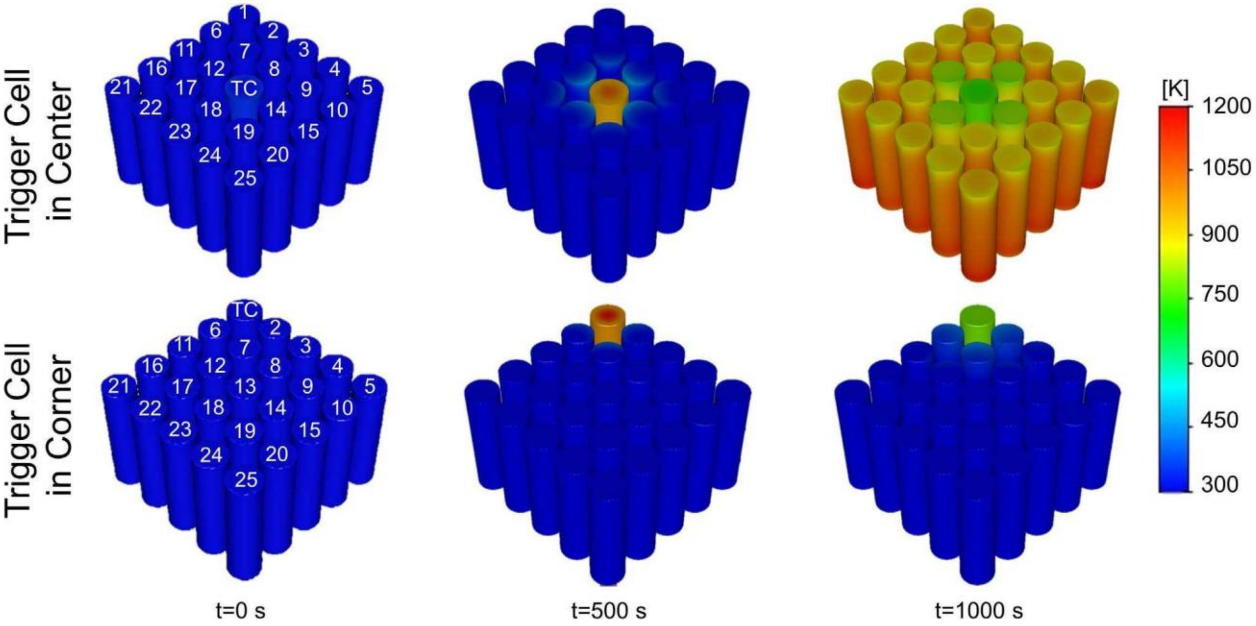

Figure 8. Effect of position of trigger cell on thermal runaway propagation in Scenario A (heating rate of 4×10^5 Wm^{-2} for 0–400 s and external convective heat transfer coefficient of 10 Wm^{-2} K^{-1}): Temperature contours at three specific times for (a) Trigger cell at the center; (b) Trigger cell at the corner.

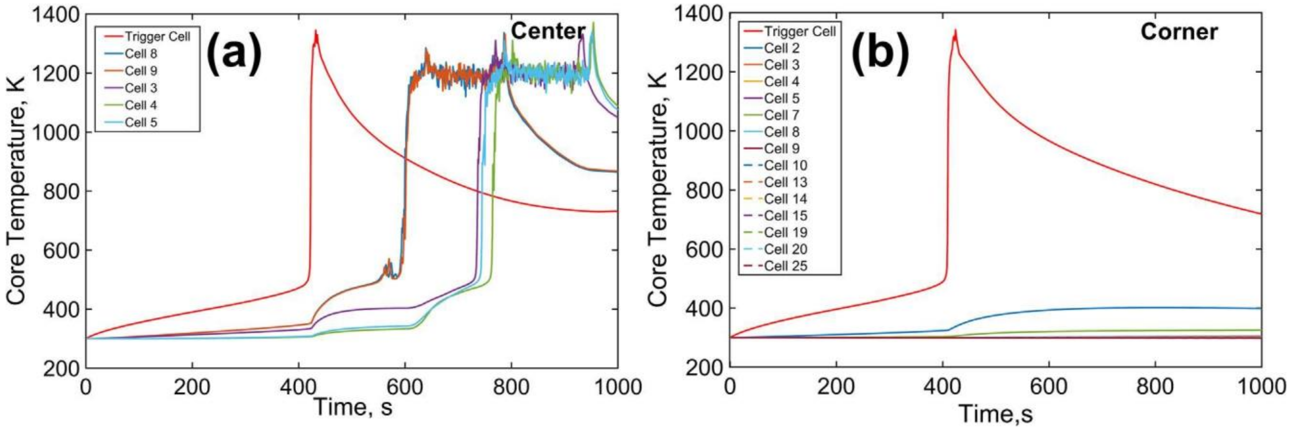

Figure 9. Temperature vs time plots for each cell for the scenario considered in Fig. 8 with (a) Trigger cell at the center; (b) Trigger cell at the corner.

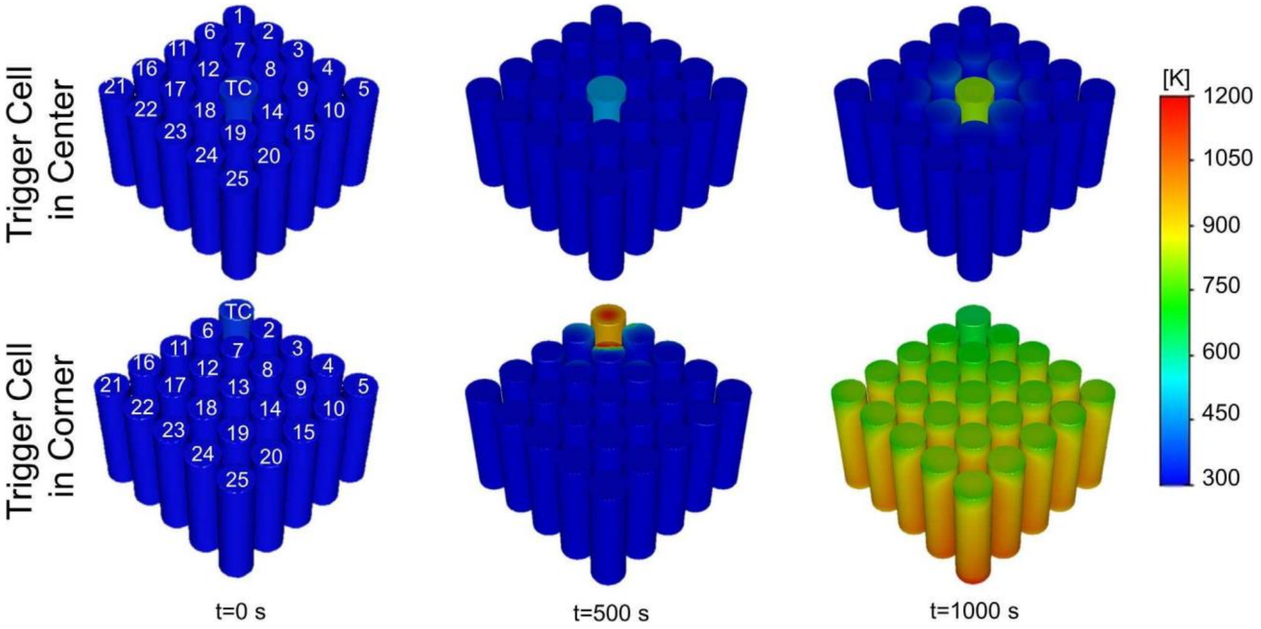

Figure 10. Effect of position of trigger cell on thermal runaway propagation in Scenario B (heating rate of 3×10^5 Wm^{-2} for 0–400 s and external convective heat transfer coefficient of 0 Wm^{-2} K^{-1}): Temperature contours at three specific times for (a) Trigger cell at the center; (b) Trigger cell at the corner.

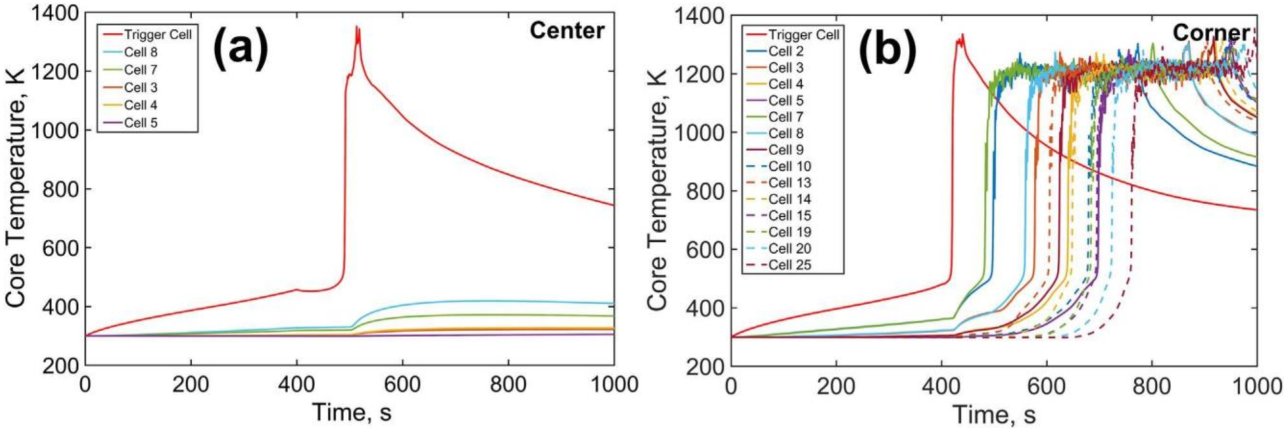

Figure 11. Temperature vs time plots for each cell for the scenario considered in Fig. 10 with (a) Trigger cell at the center; (b) Trigger cell at the corner.

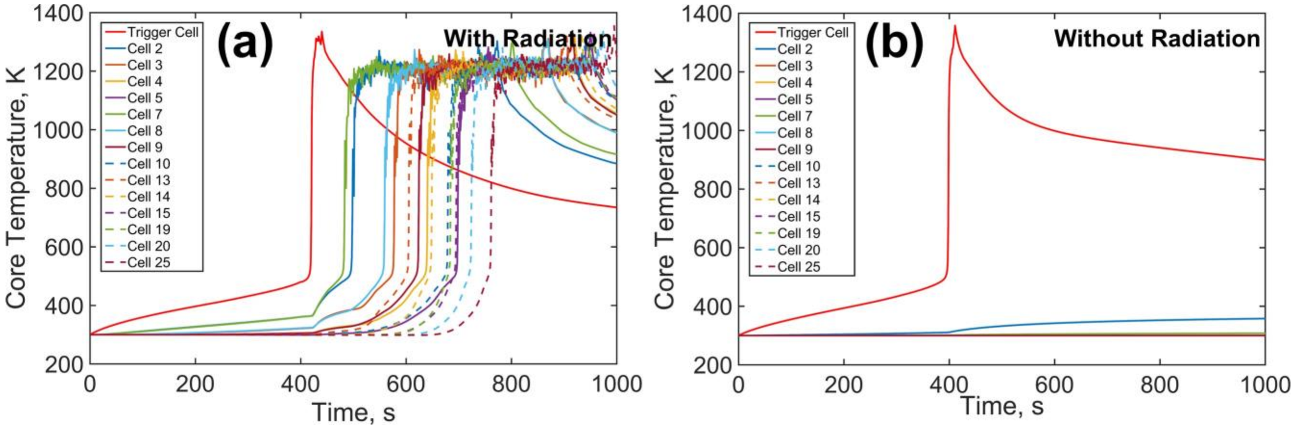

Figure 12. Impact of modeling of radiative heat transfer on the prediction of thermal runaway propagation: Temperature vs time plots for each cell in the pack (a) with radiation modeling, (b) without radiation modeling. In both cases, the cell-to-cell is 4 mm, thermal conductivity of interstitial material is 0.02 $\mathrm{Wm^{-1}\,K^{-1}}$, external convective heat transfer coefficient is 0 $\mathrm{Wm^{-2}\,K^{-1}}$, trigger cell is at center, and heating rate is 3×10^5 $\mathrm{Wm^{-2}}$ for 0–400 s.

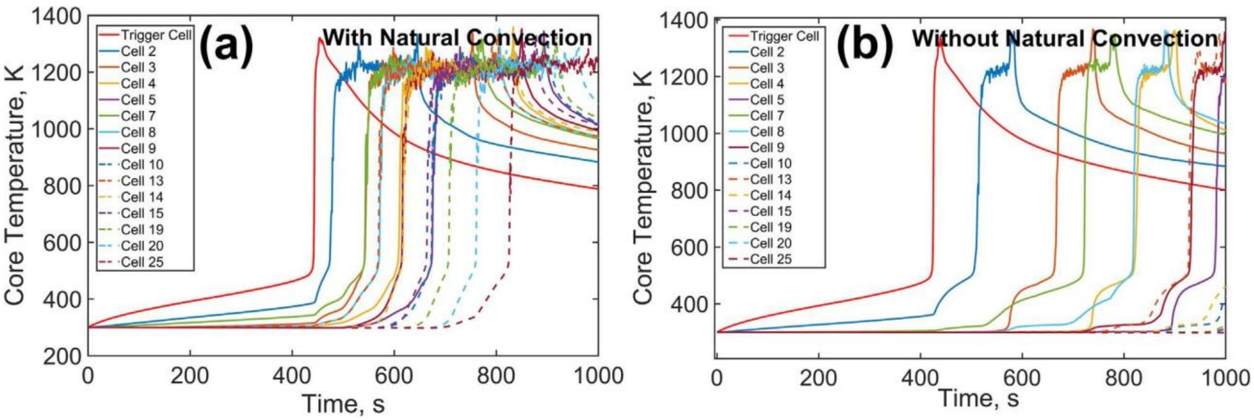

Figure 13. Effect of modeling of natural convection on the prediction of thermal runaway propagation: Temperature vs time plots for each cell in the pack (a) with natural convection modeling, (b) without natural convection modeling. In both cases, the cell-to-cell is 1 mm, thermal conductivity of interstitial material is 0.02 Wm^{-1} K^{-1}, external convective heat transfer coefficient is 10 Wm^{-2} K^{-1}, trigger cell is at a corner, and heating rate is 4×10^5 Wm^{-2} for 0–400 s.

References

1. B. Diouf and R. Pode, Renew. Energy, 76, 375 (2015).
2. T. Reddy (ed.), Linden's Handbook of Batteries (McGraw-Hill, New York, NY) 4th ed. (2010).
3. K. Shah, V. Vishwakarma, and A. Jain, J. Electrochem. Energy Convers. Storage,
4. 13 (2016).
5. T. M. Bandhauer, S. Garimella, and T. F. Fuller, J. Electrochem. Soc., 158, R1 (2011).
6. R. Spotnitz and J. Franklin, J. Power Sources, 113, 81 (2003).
7. I. Esho, K. Shah, and A. Jain, Appl. Therm. Eng., 145, 287 (2018).
8. R. C. Shurtz et al., J. Electrochem. Soc., 166, A2498 (2019).
9. K. Shah, D. Chalise, and A. Jain, J. Power Sources, 330, 167 (2016).
10. P. Huang, H. Chen, A. Verma, Q. Wang, P. Mukherjee, and J. Sun, J. Hazardous Mater., 369, 268 (2019).
11. K. Shah and A. Jain, Int. J. Energy Res., 43, 1827 (2019).
12. G. H. Kim, A. Pesaran, and R. Spotnitz, J. Power Sources, 170, 476 (2007).
13. X. Feng et al., Appl. Energy, 154, 74 (2015).
14. J. Lamb, C. J. Orendorff, L. A. M. Steele, and S. W. Spangler, J. Power Sources,
15. 283, 517 (2015).
16. W. Q. Walker et al., J. Power Sources, 415, 207 (2019).
17. C. F. Lopez, J. A. Jeevarajan, and P. P. Mukherjee, J. Electrochem. Soc., 162, A1905 (2015).
18. R. M. Spotnitz, J. Weaver, G. Yeduvaka, D. H. Doughty, and E. P. Roth, J. Power Sources,

163, 1080 (2007).

19. R. Spotnitz and R. Muller, Electrochem. Soc. Interface, 21, 57 (2012).
20. M. Chen et al., Energies, 8, 490 (2015).
21. L. Torres-Castro, A. Kurzawski, J. Hewson, and J. Lamb, J. Electrochem. Soc., 167,
22. 090515 (2020).
23. W. A. Hermann, S. I. Kahn, V. H. Mehta, and D. G. Beck, US Patent No. 8541126B2 (2013).
24. Q. Li et al., J. Power Sources, 429, 80 (2019).
25. A. Prilutsky and W. A. Hermann, US Patent No. 9093726B2 (2015).
26. J. Xu, C. Lan, Y. Qiao, and Y. Ma, Appl. Thermal Eng., 110, 883 (2017).
27. M. Parhizi, M. B. Ahmed, and A. Jain, J. Power Sources, 370, 27 (2017).
28. T. L. Bergman, A. S. Levine, F. P. Incropera, and D. P. Dewitt, Fundamentals of Heat and Mass Transfer (Wiley, New York) 8th ed. (2020).
29. T. S. Bowling, J. Atmos. Terr. Phys., 56, 539 (1994).
30. T. Walker, S. C. Xue, and G. W. Barton, J. Heat Transfer, 132, 1 (2010).
31. S. J. Drake et al., J. Power Sources, 252, 298 (2014).

CHAPTER 3

Investigation of the Impact of Flow of Vented Gas on Propagation of Thermal Runaway in a Li-Ion Battery Pack

Thermal runaway in Li-ion cells is a key technological challenge that impacts the performance, safety and reliability of electrochemical energy conversion and storage devices.[1] Thermal runaway typically initiates when a cell is subjected to thermal, mechanical or electrical abuse conditions, such as high temperature, nail penetration or overcharging.[2] Decomposition of the Solid Electrolyte Interphase (SEI) layer occurs early in the thermal runaway process, which may generate sufficient heat to trigger decomposition reactions at the electrodes, eventually leading to decomposition and combustion of the electrolyte.[3] A cell undergoing thermal runaway may also rupture and release vent gases, which may contribute towards propagation of thermal runaway to neighboring cells in a battery pack.[2] Despite a large volume of past research, thermal runaway remains an active area of research, and methods for preventing, mitigating or predicting thermal runaway are of much interest. In the context of large electrochemical energy conversion and storage systems, thermal runaway initiated in a single cell often propagates to neighboring cells, which eventually destroys the entire battery pack. Prevention of thermal runaway propagation is critical for limiting catastrophic failure of the entire battery pack. A number of studies have investigated the propagation of heat from one cell to the other in a large battery pack. Experimental measurements of thermal runaway propagation with a number of different cell chemistries and formats have been reported.[4,5,6] Accelerating Rate Calorimetry (ARC) is a commonly used experimental technique for measurement of thermal properties and heat generation rates.[7] Experimental analysis of thermal response of various Li-ion battery configurations to thermal abuse has been reported.[8] Numerical simulations have also been used to study a variety of aspects of thermal runaway propagation. For example, the role of thermal conduction through the interstitial material, as well as direct, surface-to-surface radiation between cells has been studied.[9] An optimal range of thermal conductivity has been identified.9 The use of metal plates between cells and reducing the state of charge have been investigated for preventing propagation between cells.[10,11] A number of other cooling mechanisms have also been investigated for prevention of thermal runaway propagation, including phase change composite materials,[12,13] evaporative cooling,[14] liquid mist,[15] and aerosol insulation combined with a cooling plate.[16] The influence of different cell packing patterns on Li-ion thermal runaway propagation has also been investigated.[17] Investigation of thermal runaway in a battery pack initiated by mechanical nail penetration of one of the cells showed significant difference between pouch and cylindrical cells, and, for cylindrical cells, strong dependence on the electrical configuration of the battery pack.[18] In addition to direct heat transfer between cells, gases venting out of the trigger cell after rupture may also play an important role in thermal runaway propagation. While the venting of hot gases from the trigger cell may momentarily cause cooling of the trigger cell due to evaporation and removal of hot material from the cell, the flow of vented gases outside the trigger cell causes advective transport of thermal energy to the surrounding cells. In addition, the vented gases may also combust outside the trigger cell, which generates even more heat.[2] The nature of venting during thermal runaway has been investigated in a number of papers. Coupled thermal and gas generation simulations based on finite-element technique have been reported for studying onset and evolution of thermal runaway venting in 18650 Li-ion cells. [19,20,21] The composition of vented gases is important for understanding post-venting events such as combustion and thermal advection, and has been reported in a number of papers. Measurements of total gas emission volumes, gas emission rates and amount of HF and CO2 emissions during venting have been presented.[22] A key conclusion from this work was the large variability in venting time from a battery pack, ranging from 4 to 45 min depending on the chemistry of the underlying cells.[22] Differential Scanning Calorimetry (DSC) and gas chromatography measurements have been carried out to identify key species in the venting gas for a variety of cell chemistries and configurations.[23,24] Venting time of up to 30 s was reported for individual LFP cells.[25] It has been shown that temperature of the first detected exothermic reaction, maximum cell temperature, amount of vent gas and composition of vent gas depend strongly on SOC and the nature of abuse leading to thermal runaway.[25] Internal pressure change during venting of 18650 cells has been studied using computational fluid dynamics (CFD) simulations.26 Cells at higher SOC were found to produce more heat and venting gas, resulting in higher internal pressure and subsequently a greater risk of side wall breaching.[26] A limited number of measurements of the temperature and speed of vent gases have also been reported. Specifically, burst pressure, vent opening area and discharge coefficient during chokedflow venting of 18650 Li-ion cell have been measured.[27] Experimentally validated finite-element simulations of the venting process have been used to determine Current Interrupt Device (CID) activation pressure and vent activation pressure at different ambient temperatures, showing that increasing temperature reduces vent activation pressure significantly.[28] This work also presented Computed Tomography (CT) scans of vent caps, providing useful insights into the vent release process in the case of overpressure. Based on this work, rupture of the cell on the top surface is expected when the safety valve is activated. However, if the safety valve malfunctions, or if there is weakening of the side wall due to mechanical impact, rupture may occur on the side wall.[29] Ejecta venting from side wall rupture may directly impinge on neighboring cells. The advection of gases venting from the trigger cell into its surroundings, including in the gaps between neighboring cells, is a coupled heat and mass transfer problem, driven mainly by the gas pressure and speed at the vent hole. In this case, the temperature and velocity of escaping gases determines the amount of thermal energy transferred to the surroundings. While similar heat and mass transfer problems have been studied in other fields, such as dispersion of pollutants into the atmosphere[30] and oil recovery from sub-surface rocks,[31] similar work in the context of thermal runaway in Li-ion cells has not been reported in the past. While processes within the trigger cell leading up to venting, as well as the nature of vented gases have been widely studied, as summarized above, understanding the role of venting in the propagation of thermal runaway from one cell to the other is also very important, and will require a careful study of heat and mass transfer during and immediately after the venting event. A few interesting questions that such a study may help answer include whether advective heat transfer from the trigger cell to the battery pack via vent gas alone can cause thermal runaway propagation and how this would be impacted by the cell-to-cell gap, battery pack geometry and vent size and location on the trigger cell. Additionally, combined synergistic effects of venting and other heat transfer mechanisms on propagation may also be of interest. This paper presents three-dimensional, non-linear numerical simulations of mass and heat transfer in a battery pack with hot gases venting out of a trigger cell. The constitutive energy, momentum and mass conservation equations along with appropriate boundary conditions are numerically solved. These simulations help characterize how the ejecta flow distributes thermal energy to the surrounding cells in the pack, and therefore, may contribute towards propagation of thermal runaway. Results indicate that the relative flow resistances encountered by ejecta flow for lateral transport and transport in the gap between cells play a key role in determining whether thermal runaway propagation occurs. The role of location of the vent hole is also shown to be an important determinant of propagation into neighboring cells. Results discussed here help understand an important mechanism underlying thermal runaway propagation in a battery pack. These results may help contribute towards the design of battery packs with improved thermal runaway safety and reliability.

3.1 Simulation set up

3.1.1 Geometry

Figure 1 shows top and side view schematics of the simulation geometry, which consists of a 5 by 5 array of uniformly arranged 18650 cells within an enclosed box. The volume between cells is occupied by air. In addition to the cell diameter, the two key geometrical parameters of this geometry are the cell-to-cell gap and the overhead gap, both of which are indicated in Fig. 1. The overhead gap is the clearance between the top of the cells and the battery pack enclosure. Hot ejecta is assumed to escape the trigger cell 1 in the present simulations from a 7 mm2 circular vent hole and flow into the battery pack. Two locations of the vent hole either on the top surface of the trigger cell, or on the curved surface with center positioned at 2.5 mm below the top surface and pointing towards cell 2 are considered in this work. These locations are indicated in Fig. 1. Rupture and venting from the top may occur if the safety valve is released due to overpressure during thermal runaway. Rupture and venting from the side wall may occur if the safety valve malfunctions and/or if the side wall is weakened due to physical impact in case of mechanical abuse.29 Side wall rupture is potentially more dangerous for thermal runaway propagation and therefore important to study as the ejecta might directly impinge on neighboring cells. The cells are assumed to be merely stored within the pack, and therefore, no charge/discharge of cells is considered. Secondary venting, i.e. venting from non-trigger cells to which thermal runaway propagates from the primary trigger cell is neglected. Finite volume simulations are designed and carried out to account for fluid flow, and consequently heat transfer, induced by the ejecta escaping from the trigger cell. Temperature-dependent heat generation in the cells due to the various decomposition reactions is modeled using non-linear Arrhenius equations. Direct cell-to-cell heat transfer due to radiation is also accounted for. Thermal conduction between cells is ignored due to the much larger timescale for heat diffusion through materials such as electrical connectors compared to the advection timescale associated with the high speed flow. The presence of solid particles in the gas flow is ignored due to the potentially minor role played by the solid particles in cell-to-cell heat transfer, especially due to the high speed of the flow and relatively small fraction of solid particles in the flow. Heat generation due to reaction between vent gases and ambient air outside the cell is ignored due to the small time scale of the problem considered here. Governing equations for each phenomenon are described below in detail.

3.2 Governing equations

3.2.1 Mass, momentum, and energy transport equations

Mass, momentum and energy transport equations. Due to the high speed of venting gases, the vent flow is expected to be turbulent, necessitating detailed turbulence modeling for the flow. Amongst the multiple turbulence modeling techniques that have been proposed, the Spalart-Allmaras technique,[32] based on the Reynolds Average Navier–Stokes (RANS) method is used in this work. This technique has been used extensively in the past to model turbulent high-speed flows such as jets,[33] and shows good convergence without being memory-intensive. This technique also offers reduced computational effort as it needs to solve only one equation, unlike other solvers, which require more than one equation. In the Spalart-Allmaras technique, the mass conservation is given by the usual continuity equation, given by

$$\nabla.(\rho\mathbf{V}) = 0 \tag{1}$$

The transport equation for any other variable a between two mesh elements i and j is given by

$$\frac{\partial(\rho.\mathrm{a})}{\partial \mathrm{t}} + \nabla_{\mathrm{i}}(\rho.\mathrm{a}.\mathrm{v}_{\mathrm{i}}) = \mathrm{G}_{\mathrm{a}} + \frac{1}{\sigma_{\mathrm{a}}}\left[\nabla_{\mathrm{i}}\left\{(\mu + \rho.\mathrm{a})\nabla_{\mathrm{j}}.\mathrm{a}\right\} + \mathrm{C}_{\mathrm{b2}}.\rho{\nabla_{\mathrm{j}}}^{2}.\mathrm{a}\right] - \mathrm{Y}_{\mathrm{a}} + \mathrm{S}_{\mathrm{a}} \tag{2}$$

Here, Ga is the production of turbulent kinematic viscosity, Sa is the source term and Ya is the destruction of turbulent viscosity that occurs in the wall region due to wall blocking and viscous damping. Cb2 and σa are constants with values of 0.622 and 2/3 respectively.33 Details of the Spalart-Allmaras model are available in past work.[33] Similarly, using Reynolds analogy to turbulent momentum transfer, turbulent heat transport equation for the turbulent flow can be written as

$$\frac{\partial(\rho.\mathrm{E})}{\partial \mathrm{t}} + \nabla_{\mathrm{i}}\, [\mathrm{v_i}\, (\rho.\mathrm{E} + \mathrm{p})] = \nabla_{\mathrm{j}}\, \left[\left(\mathrm{k} + \frac{\mathrm{C_p}\mu}{\mathrm{P_r}}\right) \nabla_{\mathrm{j}}.\mathrm{T} + \mathrm{v_i}(\tau_{\mathrm{ij}})_{\mathrm{eff}}\right] + \mathrm{S_h} \tag{3}$$

where k is thermal conductivity, E is total energy, Sh is the heat source term and (τij)eff is the stress tensor.

3.2.2 Thermal conduction

Heat transfer within each solid cell is governed by the thermal conduction equation

$$\frac{1}{\mathrm{r}} \frac{\partial}{\partial \mathrm{r}}\left(\mathrm{k_r} \mathrm{r} \frac{\partial \mathrm{T}}{\partial \mathrm{r}}\right) + \frac{\mathrm{k_\theta}}{\mathrm{r}^2} \frac{\partial^2 \mathrm{T}}{\partial \theta^2} + \mathrm{k_z} \frac{\partial^2 \mathrm{T}}{\partial \mathrm{z}^2} + \mathrm{q}''' = \rho \mathrm{c_p} \frac{\partial \mathrm{T}}{\partial \mathrm{t}} \tag{4}$$

where thermal conductivity within the cell is taken to be uniform, but orthotropic, and all properties are assumed to be independent of temperature.

3.2.3 Heat generation

In addition to the advection of thermal energy due to the high-speed flow of the ejecta, heat is also generated within each cell. This strongly temperature-dependent heat generation occurs due to SEI decomposition, negative solvent reaction, positive solvent reaction and electrolyte decomposition.[34] The scenario considered here is that of storage of cells without charge/discharge, and therefore, the only heat generation within cells is due to decomposition reactions. A standard set of governing equations for these processes are used, and parameter values corresponding to $LiCoO_2$ cell chemistry are assumed. These equations and parameter values are easily available in past work,[35] and therefore, are not being included here. Heat generated in these decomposition reactions is implemented as a temperature-dependent volumetric heat generation term appearing in the energy conservation equation for the cells. Each 18650 cell is modeled as a cylindrical orthotropic material, with values of 0.2, 32 and 32 $\mathrm{Wm^{-1}\,K^{-1}}$ in the radial, axial and circumferential directions, respectively, based on past measurements.[36] Density and heat capacity are taken to be 2280 $\mathrm{kgm^{-3}}$ and 715 $\mathrm{Jkg^{-1}\,K^{-1}}$, respectively, also based on past work.[34]

3.2.4 Radiative heat transfer

The cells are expected to reach very high temperature during these simulations, both due to heat advected by the vent gases, as well as heat generation due to decomposition reactions associated with thermal runaway. As a result, radiation is expected to be an important mode of heat transfer and must be accounted for. Radiation modeling between two surfaces is implemented using a surface-to-surface radiation model. Total energy flux leaving a surface comprises of irradiation flux from surroundings, known as reflected energy, and emitted energy by virtue of its own temperature. For any surface i, the amount of energy leaving the surface is [37]

$$q_{out,i} = \varepsilon_i \sigma T_i^4 + b_i q_{in,i} \tag{5}$$

where εi and bi are the emissivity and reflectivity, respectively, of the i th surface, and σ is the Boltzmann constant. qin,i is the irradiation flux incident on the surface from the surroundings, which is given by the net sum of energy incident from all other surfaces based on the view factors fji as follows:

$$A_i \cdot q_{in,i} = \sum_{j=1}^{N} A_j \cdot q_{out,j} \cdot f_{ji} \tag{6}$$

Therefore, total energy leaving the surface in Eq. 5 can be re-written as:

$$q_{out,i} = \varepsilon_i \cdot \sigma T_i^4 + b_i \cdot \sum_{j=1}^{N} f_{ij} \cdot q_{out,j} \tag{7}$$

Thus, the net radiation emitted from a surface comprises of emission from the surface and sum of radiation flux intercepted and reflected by virtue of other visible surfaces. In calculation of total radiation heat flux from a surface, view factors play a key role. For these simulations, view factors are computed using ray tracing method as described in a past study.[38] Radiation flux obtained is used as heat input for the energy equation of each cell. For this radiation module, each cell surface in the simulation geometry is considered as a diffuse gray surface with an emissivity of 0.1. Radiative properties of most practical surfaces are independent of direction and wavelength, which justifies the diffuse gray assumption. This assumption also results in time-efficient computation of radiative heat transfer at each timestep. Typical Li-ion cells have shiny metal casing, which justifies the low value of emissivity.

The governing equations listed above must be supplemented with appropriate boundary conditions. Boundary conditions for the vent through which the ejecta flows out of the trigger cell are deduced based on isentropic flow equations as described in section 2.2.5 below. Diagonal symmetry is applied on the overall simulation geometry for efficient computation, resulting in adiabatic boundary condition on diagonal face of the box as shown in Figure 1. Natural convective cooling to the ambient is modeled on the remaining four faces. In simulations involving an external opening on the battery pack, ambient pressure boundary condition is implemented on the external opening.

3.2.5 Isentropic flow equation

This subsection describes the approach used for determining velocity and temperature of the vented ejecta as a function of time based on stagnation pressure and mass flow rate measurements.[27] The temperature and velocity values calculated based on this approach are used to specify boundary conditions on the outlet vent for the ejecta. This approach utilizes stagnation pressure measurements reported in the past for venting of similar Li-ion cells.[27] First, the Mach number of the ejecta can be obtained by inserting the experimental pressure measurements in the following relationship:[39]

$$\frac{\mathrm{p_0}}{\mathrm{p}} = (1 + \frac{\gamma - 1}{2} * \mathrm{Ma}^2)^{\frac{\gamma}{\gamma - 1}} \tag{8}$$

where the freestream pressure is considered to be constant at 1 atm. Mach number is then used, along with thermophysical properties of ejecta and mass flow rate measurements, to determine stagnation temperature T_0 as follows[18]

$$\frac{\dot{\mathrm{m}}}{\mathrm{A}} = \sqrt{\frac{\gamma}{\mathrm{R}}} * \frac{\mathrm{p_0}}{\sqrt{\mathrm{T_0}}} * \mathrm{Ma}(\, 1 + \frac{\gamma - 1}{2} * \mathrm{Ma}^2)^{\frac{\gamma + 1}{2(\gamma - 1)}} \tag{9}$$

Finally, the venting temperature is determined from T_0 by considering isentropic flow through the vent outlet, assuming the ejecta to be a perfect gas. Under these conditions, the venting temperature is related to stagnation temperature as follows:

$$\frac{T_0}{T} = (1 + (\frac{\gamma - 1}{2}) * Ma^2) \tag{10}$$

Further, the acoustic speed is obtained from the following relationship:

$$a = \sqrt{\gamma RT} \tag{11}$$

Note that the Mach number is the ratio of flow speed to acoustic speed. Therefore, from the computed values of Mach number and acoustic speed as functions of time, the flow speed can be determined as a function of time.

All required thermophysical properties are calculated based on weighted average of gaseous components (CO_2, H_2, C_2H_4, CO, CH_4, C_3H_6, C_2H_5F) reported for Lithium Nickel Cobalt Aluminum Oxide (NCA)[40] and Lithium Cobalt Oxide (LCO)[41] type cathodes using Coolprop,[42] an open source fluid property database. The vent gas is assumed to be a calorically perfect gas. The three-coefficient Sutherland viscosity model is used to account for temperature dependent change in viscosity of the ejecta.[43] Key transport properties, including γ for the two cell types are summarized in Table 1. It is found that the composition, and hence transport properties of the vent gas mixture is very close to each other for NCA and LCO cathode chemistries. Specifically, γ for the two cell types are within 2% of each other. The closeness of transport properties is likely because the gases in the vent are mainly organic, and therefore strongly dependent on the electrolyte and only weakly dependent on the cathode material.

Based on the isentropic flow analysis described above, fourth degree polynomial curve-fit expressions for transient velocity and temperature for the vent gas are determined to be

$$V(t) = -12.59t^4 - 73.387t^3 + 180.18t^2 + 20.66t + 218.76 \quad (11)$$

$$T(t) = 86.146t^4 - 345.78t^3 + 749.76t^2 - 153.27t + 361.82 \quad (12)$$

where t, T and V have units of s, K and ms^{-1}, respectively.

Figure 2 plots the vent velocity and temperature as functions of time based on the calculations outlined above for both NCA and LCO cell types. Data for the two cell types are very similar to each other due to very similar values of γ. This shows that there is negligible difference between venting and venting-related thermal runaway propagation behavior between the two chemistries.

Figure 2 shows that the vent temperature continues to increase throughout the venting process, whereas the vent velocity reaches a peak and then comes down. This trend directly results from the experimental measurements of stagnation pressure[27] underlying these calculations, which show that stagnation pressure decreases with time. Since the stagnation pressure is directly proportional to the Mach number, as seen in equation (8), this may result in reduction in speed after much of the trigger cell has emptied out. On the other hand, decrease in vent velocity causes vent temperature to increase as seen in equation (10). This inverse proportionality results from the conversion of pressure energy into intermolecular thermal energy.

3.2.6 Meshing and other simulation details

A 3D polyhedral meshing technique is used in all simulations due to its high resolution, smaller residual values and lower meshing time compared to other meshing techniques. Polyhedral meshing increases number of neighboring cells, which in-turn improves gradient approximation and reduces probability of errors. Global mesh controls allow automatic calculation of global element size based on smallest geometric entity. The smallest element length used is 10^{-5} m, and advanced sizing functions are used for resolving regions with curvature and proximity. Other mesh parameters include a growth rate of 1.1 and squish index of 0.28. A total of 7.2 million elements are used in each simulation. Mesh independence of results is established and is discussed in section 3.

Venting of hot ejecta lasts for first two seconds of the simulation requiring extremely small time stepping to meet the convergence criteria. Hence, 0.01 millisecond fixed time stepping and 0.001 relative tolerance limit are used during the venting phase of the simulation. For rest of the simulation, an extremely fine timestep is not needed since high speed venting process has stopped. In this regime, a 1 millisecond timestep is used in order to minimize computation time while keeping residuals within tolerance. Simulation is stopped at 10 seconds, since by this time, the cells have either cooled down substantially or onset of thermal runaway has occurred. A comprehensive mesh sensitivity analysis is performed prior to actual simulations in order to determine the required spatial discretization to obtain grid-independent results.

3.3 Results and discussion

A summary of goals, key parameters and conclusions of each simulation described in this section is summarized in Table 2. Each simulation is labeled, in order to enable cross-referencing between the summary in Table 2 and detailed discussion below.

The establishment of grid independence of the simulation results is discussed first. A baseline simulation (Simulation A) comprising 25 cells is carried out, as shown in Figure 1. In this simulation, the cell-to-cell gap and overhead gap are 4 mm and 5 mm, respectively, and venting occurs for 2 s duration from a 7 mm^2 hole at the top of the trigger cell located at a corner of the geometry. As discussed in the previous Section, Arrhenius heat generation is considered in all cells, except the trigger cell, to model thermal runaway if a certain threshold temperature is exceeded. Temperature and velocity fields are computed as functions of time using the methodology discussed in Section 2. The maximum surface temperature of cells 3 and 4 are plotted in Figures 3(a) and 3(b), respectively, for three different grid sizes. When the number of elements is increased from 1.5 million to 3.6 million, both Figures 3(a) and 3(b) show significant change in the predicted temperature. However, increasing further to 4.2 million elements changes the resulting temperature distribution only by 3%. This establishes grid independence at 3.6 million elements, which is the grid size used for all the simulations discussed in the remainder of this work.

To understand the nature of thermal and fluid transport occurring in this system, color plots of the temperature and velocity fields in the interstitial air around the cells are plotted at different times for a simulation with the cell-to-cell gap of 1 mm in Figures 4(a) and 4(b), respectively. Similar plots for the cell-to-cell gap of 4 mm are presented in Figure 5. In these plots, the trigger cell is shown in dark gray color on the left end of the cross-section, and the vent location at the top surface of the trigger cell is also indicated with a red arrow. The cell-to-cell gap and overhead gap are 1 mm each. Both temperature and velocity color plots indicate that the thermal and fluid fields are rapidly established following the start of venting, with the vent gas advancing outwards over time. Some retraction in the gas front is observed towards the end of venting, which may be due to the reduction in vent speed, as shown in Figure 2(b). More ejecta is found to settle in the gap between cells when the cell-to-cell gap is 4 mm, which is likely due to the lower resistance to flow into these gaps. Specifically, there is a large temperature rise in the gap between the trigger cell and cell 2. While this increases the risk of thermal runaway in cell 2, it may reduce the risk to other cells, which may be desirable for preventing propagation. Note that increasing the cell-to-cell gap also increases the distance that the vent gas must travel to reach other cells. However, this is unlikely to influence the likelihood of propagation much due to the very high speed at which vent gas is ejected. Instead, the propensity of the vent gas to get trapped between trigger cell and cell 2 when the cell-to-cell gap is increased is likely to be a more influential phenomena in determining whether thermal runaway propagates or not.

For a more detailed investigation of the influence of cell-to-cell gap on thermal runaway propagation, peak temperature on the surface of various cells is plotted as functions of time for cell-to-cell gaps of 1 mm and 4 mm in Figures 6 and 7, respectively (Simulations B and C). Other relevant parameters used in both simulations include an overhead gap of 1 mm, vent time of 2 s, and 7 mm^2 vent located on top surface of the trigger cell. Temperature color plots at four different times are also shown in Figures 6 and 7. Note that these Figures plot the maximum surface temperature. The corresponding color plots indicate that the peak temperature is reached only in a small of the cell, and most of the cell remains quite cold within the short simulation period.

Figure 6 shows that when the cell-to-cell gap is 1 mm, the propagation of thermal runaway is quite extensive. Cells 2, 7, 8, 9, 13 and 14 all reach very high temperatures within the 2 second vent duration. For cells 2, 7 and 8, the thermal excursion is sufficiently extensive that a very high temperature is sustained even after venting stops. In this case, sufficient volume of the cell has overheated, so that the heat generated by decomposition reactions is enough to initiate substantial self-heating in the cell even after venting stops. In contrast, even though the maximum surface temperature of cells 9, 13 and 14 also becomes high, the volume of the cell impacted is smaller, which results in unstained thermal runaway and reduction in peak temperature once the venting stops.

In comparison to the 1 mm cell-to-cell scenario presented in Figure 6, Figure 7 shows a very different nature of thermal runaway propagation when the cell-to-cell gap is 4 mm. In this case, only cell 2 experiences sustained thermal runaway. As the vent gas spreads out from the trigger cell, the flow resistance offered by the gap between trigger cell and cell 2 relative to the flow resistance offered by the overhead gap plays a key role in determining whether the vent gas spreads further outwards or mostly gets lodged in the gap. When the cell-to-cell gap is only 1 mm, there is large resistance to flow into the gap between cells, due to which, the hot vent gas flows preferentially in the overhead region, causing extensive propagation of thermal runaway as seen in Figure 6. On the other hand, when the cell-to-cell gap is relatively larger, for example 4 mm, there is much lower resistance to flow into the gap between cells, due to which, more hot vent gas flows in the gap between cells, thereby limiting the extent of propagation. In this case, most of the thermal impact of the vent gas is absorbed by cell 2, which undergoes thermal runaway, but partly protects other cells from thermal runaway.

The reduced propensity of thermal runaway propagation at large cell-to-cell gap observed in Figure 7 is consistent with past experimental measurements that suggest an inverse relationship between cell-to-cell gap and thermal runaway propagation intensity. For example, past experimental work suggests a spacing of at least 2 mm between 18650 cells in a module to prevent thermal runaway propagation.[8] In a separate work, it was shown that that 4 mm horizontal spacing and 8 mm vertical spacing is required to suppress thermal runaway propagation in 18650 battery pack.[44]

Note that the only venting considered in this work is from the trigger cell. Secondary venting from other cells that may undergo thermal runaway later is not modeled in this work.

Figure 7 shows that maximum surface temperature on cell 7 is very high during the venting period, but once venting stops, this does not lead to sustained heating typical of thermal runaway. This is because only a very small region of the cell overheats, which is not sufficient to trigger and sustain thermal runaway once the heat input from the venting gases stops. Since the hot vent gas flow is similar to a jet, temperature rise due to hot vent gas is a highly directed phenomenon – there is large temperature rise where the vent gas jet impinges directly, with relatively minor impact elsewhere. This is the reason why there is no sustained thermal runaway in several cells despite a very high value of the maximum temperature rise seen in Figure 5 and 6. This is confirmed in Figure 8, which presents temperature color plots of two contrasting cells for the 1 mm cell-to-cell gap case. Even though cells 2 and 14 both show very high maximum temperature in Figure 6, a temperature color plot of the two cells shown in Figure 7 indicates that the large temperature rise in cell 2 is observed over a much larger surface area than cell 14, which is why cell 14 cools down to ambient after the gas venting stops, whereas cell 2, having absorbed sufficient thermal energy, enters thermal runaway sustained by the heat from its own exothermic reactions.

The effect of the overhead gap is investigated next. Similar to the cell-to-cell gap, the overhead gap may play a key role in determining the nature of vent gas flow, and thus the propagation of thermal runaway by changing the volume and flow resistance offered by the overhead space relative to the flow resistance offered by the gap between the cells. The scenarios in Figures 6 and 7 correspond to an overhead gap of 1 mm. In order to investigate the impact of increasing the overhead gap, simulations are carried out at an overhead gap of 5 mm. Two different cell-to-cell gaps of 1 mm and 4 mm are simulated and shown in Figures 9 and 10(Simulations D and E), respectively. In both cases, the volume of the overhead gap is large enough that the heat carried by the vent gases is sufficiently absorbed by air in the overhead gap without significant rise in temperature in any of the cells. At an overhead gap of 5 mm, therefore, there is no significant propagation of thermal runaway, even when the cell-to-cell gap is relatively small. This suggests that it may be possible to store cells in a dense manner without compromising on safety by increasing the overhead gap.

The physical location and orientation of the vent hole on the trigger cell is also expected to play a key role in thermal runaway propagation since it governs the direction of the vent gas jet. When the vent hole is located on the top surface, the jet is not directly targeted towards any of the neighboring cells. However, if the trigger cell ruptures on the side surface, leading to venting from the side, then the hot vent gas may impinge directly on one of the neighboring cells, making it more likely for thermal runaway to propagate. A set of simulations are carried out with the vent hole located on the curved surface of the trigger cell in order to compare with prior results in which the vent hole was located on the top surface. In this case, the vent hole of the same size as before is located on the curved surface, 2.5 mm below the top surface of the cell and directed towards cell 2. Two cases of cell-to-cell gap of 1 mm and 4 mm are simulated. Peak surface temperatures on various cells as functions of time are presented for these two cases in Figures 11 and 12(Simulations F and G), respectively. Results show that in the first case (Figure 11), due to the very small distance between the vent and neighboring cells, the narrow venting jet impinges directly on the immediate neighbors, cells 2 and 7, and most of energy of the ejecta is absorbed by these cells. On the other hand, when the cell-to-cell gap is larger (Figure 12), the venting jet becomes more distributed before reaching the neighboring cells, resulting in impingement on a greater number of cells. As a result, there is greater propagation and a larger number of impacted cells, as shown in Figure 12. The deflected trajectories of ejecta upon impingement in cells in the battery pack can be visualized through color plots shown in Figures 11 and 12.

Finally, simulations are carried out to understand the impact of placing an external opening on the top of the battery pack to safely remove the vent gases and prevent thermal runaway propagation. Normally, such an external opening would open to ambient pressure, and therefore, attract the vent gases that escape from the vent hole at a much higher pressure. While the exit of vent gas is, in principle, desirable, it is important to carefully choose the location of the external opening because the external opening can create an undesirable flow pattern of the vent gas within the battery pack, which may cause propagation of thermal runaway. To investigate this in detail, two simulations are carried out with different locations of the external opening on top of the battery pack. In the first case, the opening is located directly above the location of the vent hole on the trigger cell. In the second case, the opening is located above the center of cell 13. As expected, when the external opening hole is located directly above the vent hole, the venting gases flow upwards and directly exit the batter pack through the external opening, resulting in no temperature rise in the neighboring cell at all. Due to the trivial nature of this case, temperature color plots are not shown. Figure 13(Simulation H) shows the predicted temperature field when the opening is located above the center of cell 13. In this case, a flow pattern of vent gases flowing from the high-pressure region just above the trigger cell to the low pressure opening above cell 13 is created. This inadvertently exposes several other cells to high temperature and causes thermal propagation clearly seen in the color plots and temperature plots in Figure 13, both of which show propagation of thermal runaway to several cells in the pathway between trigger cell and cell 13.

The scenario discussed above is, of course, a best-case scenario, in which the location of the trigger cell and the vent hole is assumed to be known in advance. Ideally, the external opening would be placed directly above the trigger cell. However, in reality, which cell will fail, and vent may not be known in advance. Therefore, it is not straightforward to choose the location of the external opening. Of course, placing an external opening above every cell would greatly help suppress thermal runaway propagation, but doing so may be prohibitively expensive. It may be possible to optimize the number of vents and their locations to minimize the propagation of thermal runaway in the battery pack regardless of the location of the trigger cell, while keeping the cost of building such a pack reasonably low.

List of Figures

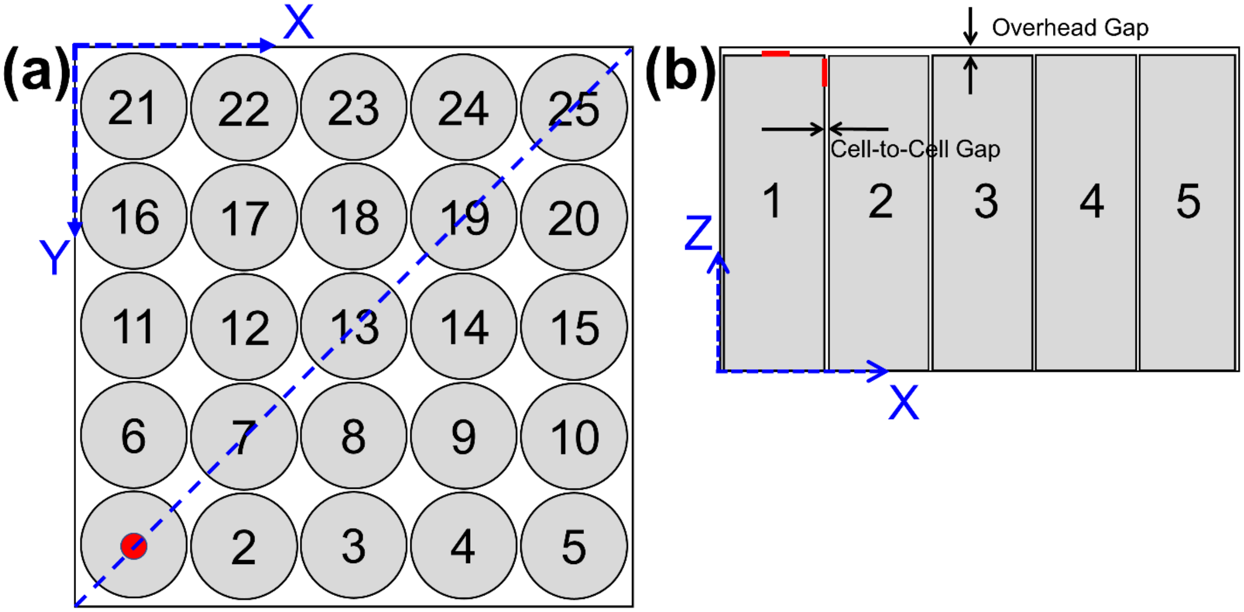

Figure 1. Schematic of 18650 Li-ion battery pack containing 25 cells: (a) Geometry of battery pack with trigger cell at position 1 and intercellular gap of 4 mm. (b) Cross sectional view of the 3D tetrahedral meshing elements used in the simulation.

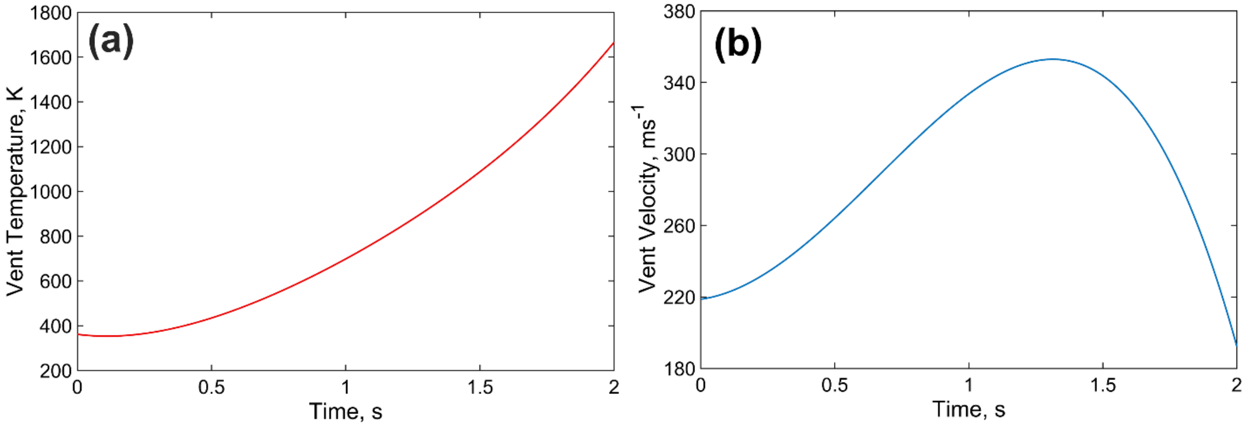

Figure 2. Temperature and velocity of venting gas as functions of time determined from calculations described in section 2.2.5.

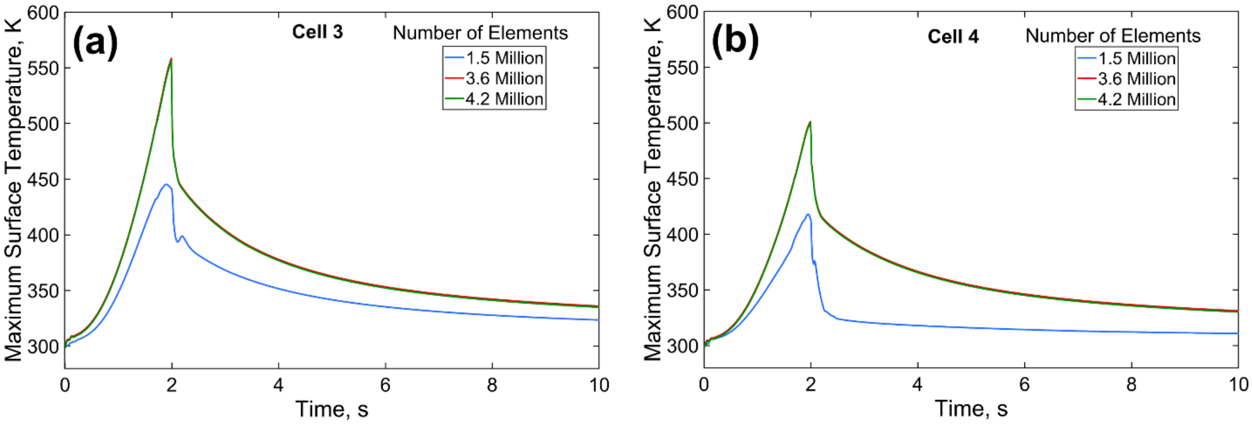

Figure 3: Simulation results to establish grid independence: Maximum surface temperature as a function of time for (a) Cell 3 and (b) Cell 4. Problem parameters include 5 mm overhead gap, 4 mm cell-to-cell gap, 2 s venting time and $7 mm^2$ vent placed at center of top surface of Cell 1.

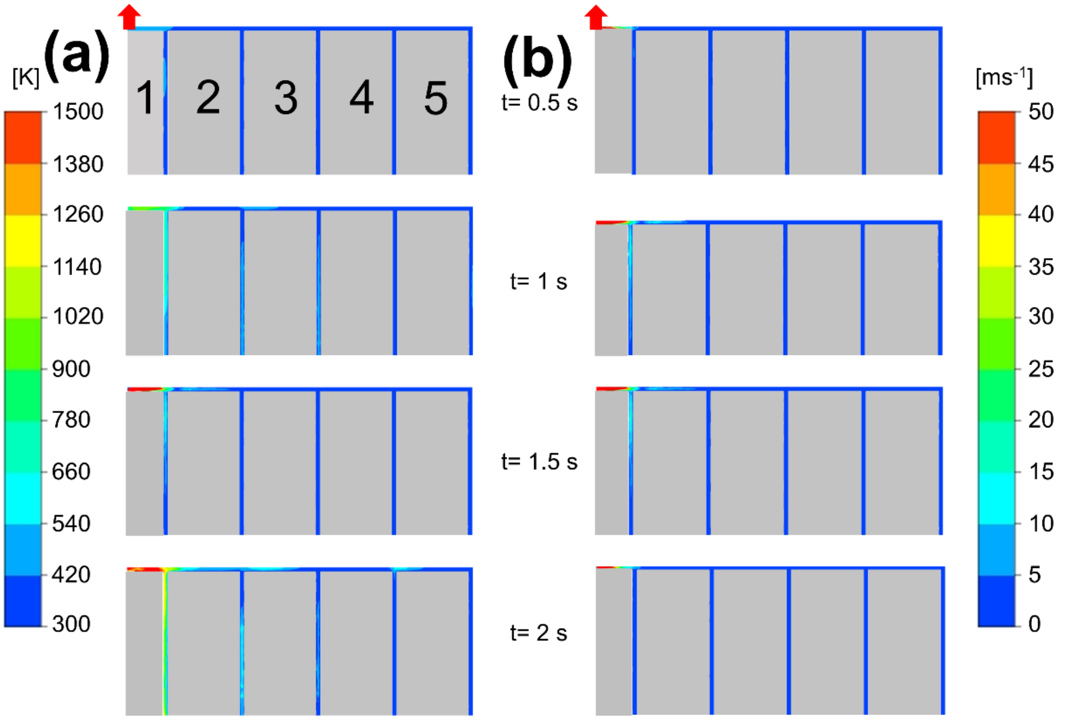

Figure 4: Color plots in the XZ plane showing evolution of the (a) Temperature and (b) Velocity fields at various times for 1 mm overhead gap and 1 mm cell-to-cell gap. The vent hole is located at the center of the top surface of trigger cell.

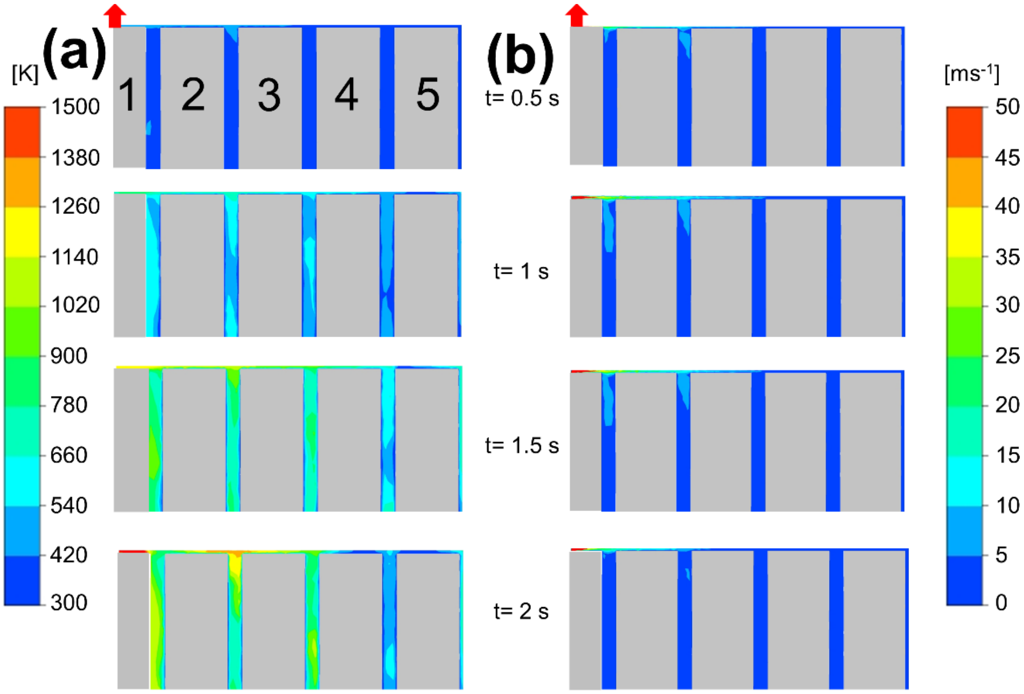

Figure 5: Color plots in the XZ plane showing evolution of the (a) Temperature and (b) Velocity fields at various times for 4 mm overhead gap and 4 mm cell-to-cell gap. The vent hole is located at the center of the top surface of trigger cell.

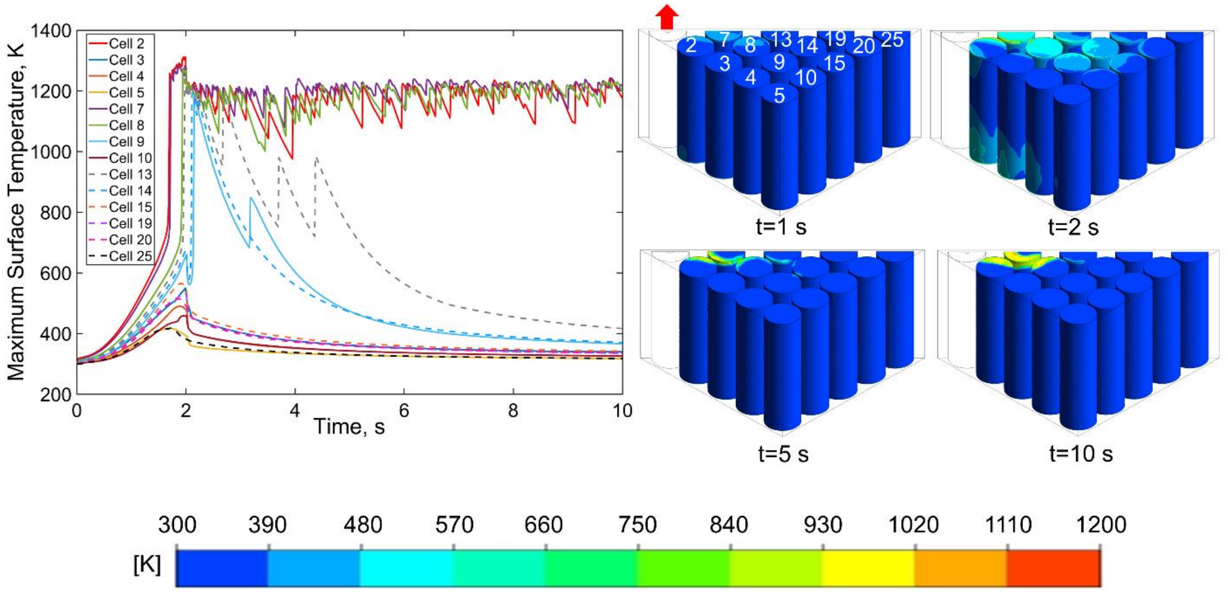

Figure 6: Effect of Cell-to-cell gap: Temperature plots for 1 mm cell-to-cell gap. Other parameters include 1 mm overhead gap, 2 s venting time and 7mm^2 vent placed at center of top surface of Cell 1.

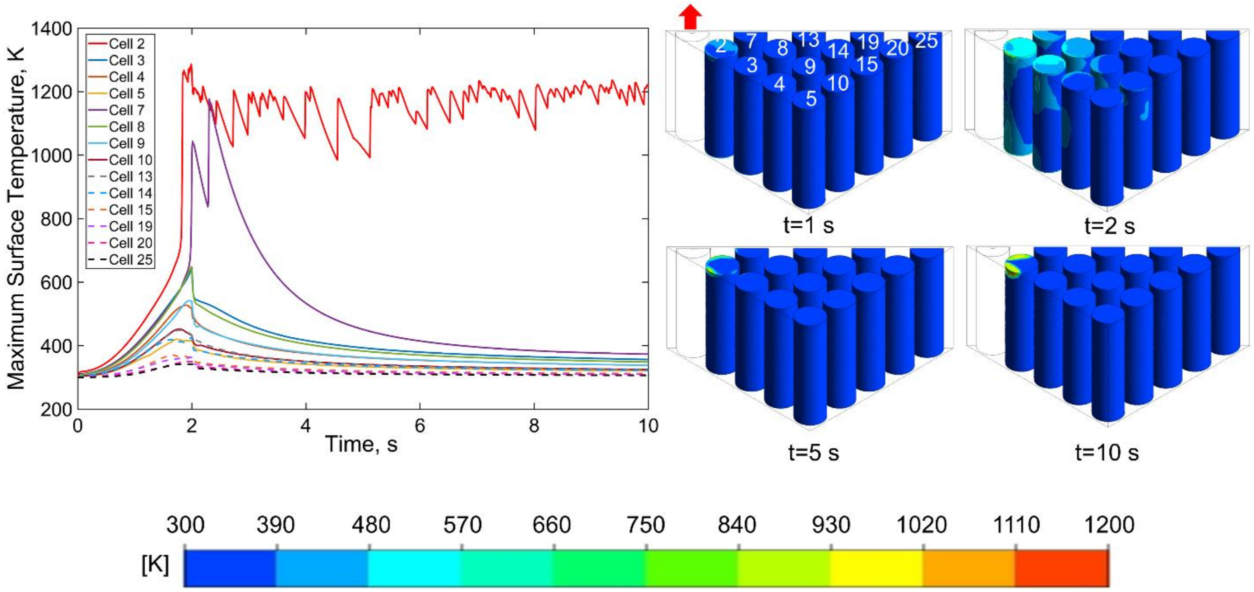

Figure 7: Effect of Cell-to-cell gap: Temperature plots for 4 mm cell-to-cell gap. Other parameters include 1 mm overhead gap, 2 s venting time and 7mm^2 vent placed at center of top surface of Cell 1.

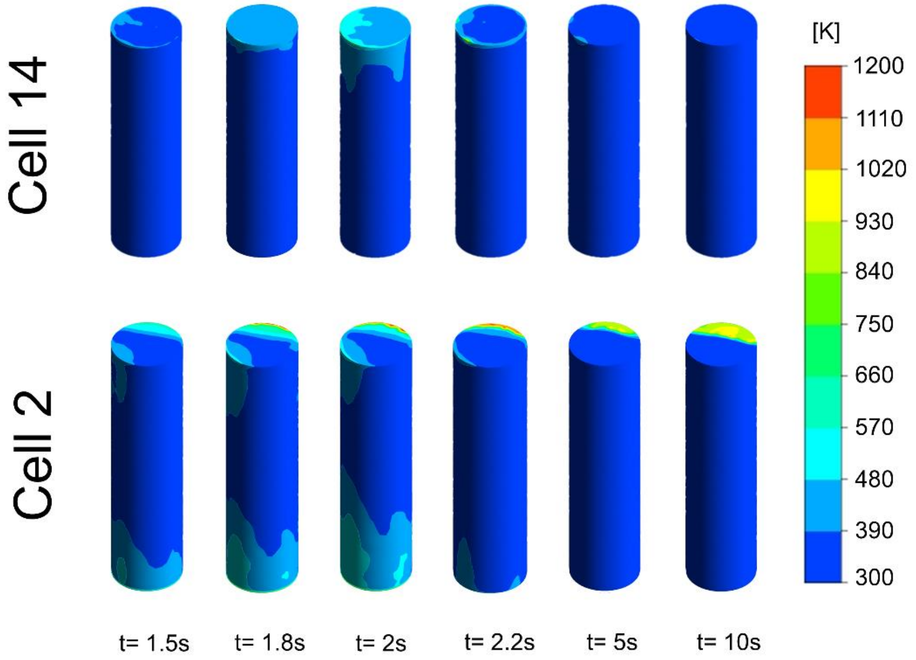

Figure 8: Temperature plots cell 14 and cell 2 for 1 mm cell-to-cell gap. Other parameters include 1 mm overhead gap, 2 s venting time and 7mm^2 vent placed at center of top surface of Cell 1.

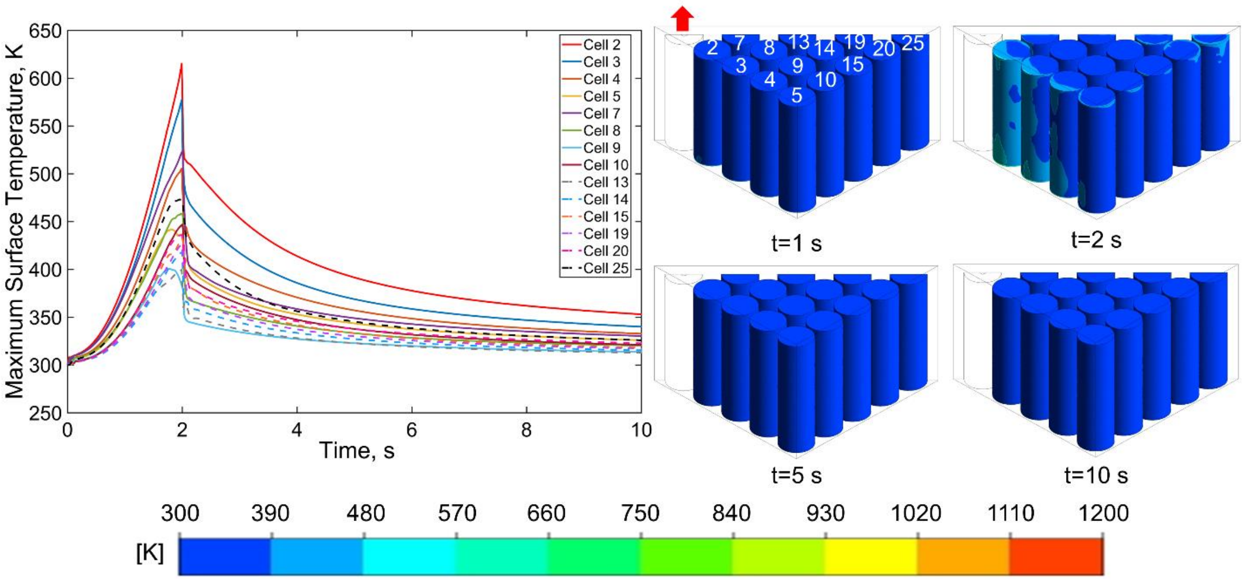

Figure 9: Effect of Overhead space: Temperature plots for 5 mm overhead gap (0-2s) venting time and 7mm^2 vent placed at center of top surface of Cell 1 for 1mm cell-cell gap.

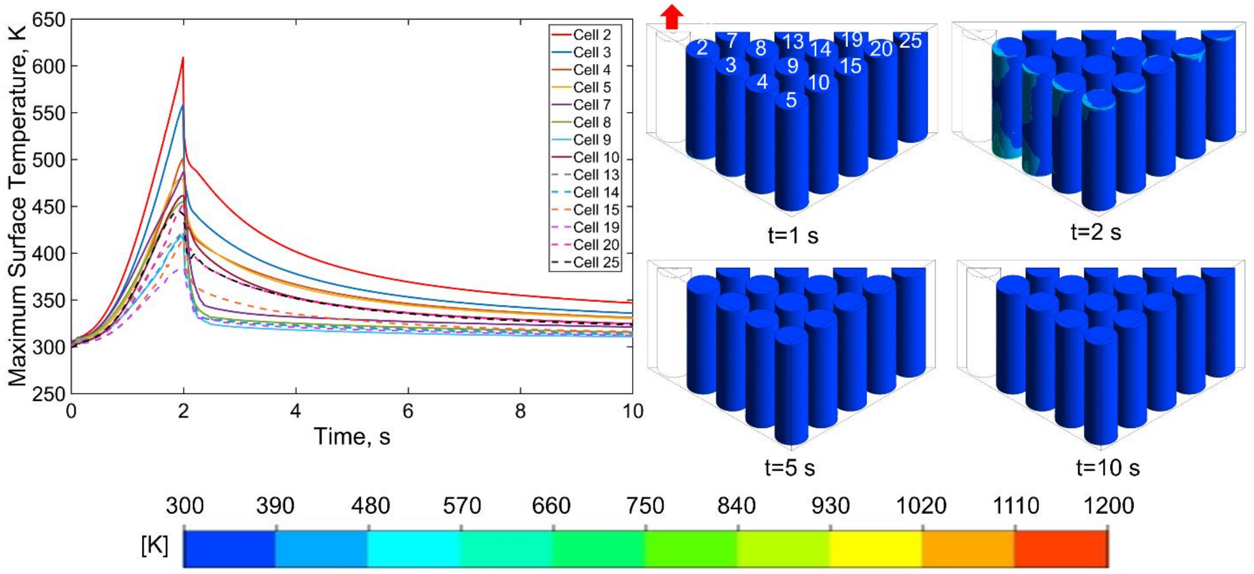

Figure 10: Effect of Overhead space: Temperature plots for 5 mm overhead gap (0-2s) venting time and 7mm^2 vent placed at center of top surface of Cell 1 for 4mm cell-cell gap.

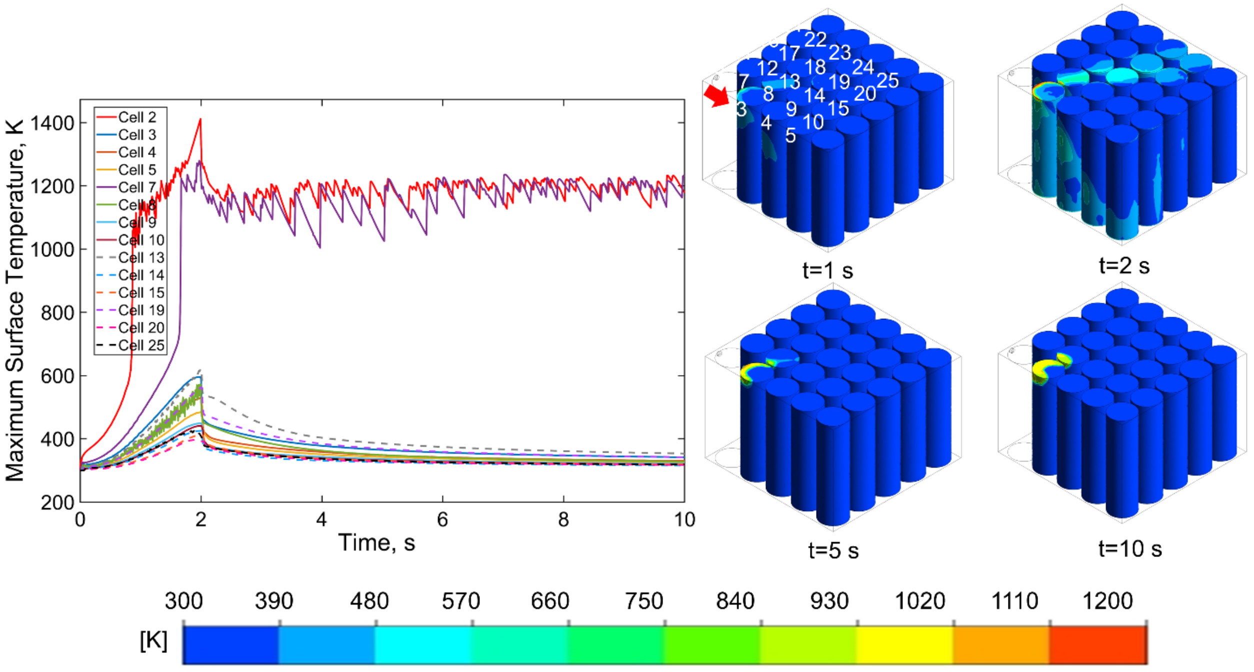

Figure 11: Effect of location of vent: Temperature plots for 1 mm overhead gap (0-2s) venting time and 7mm^2 vent placed at 63.5 mm height on curved surface of Cell 1 facing cell 2 for 1mm cell-cell gap.

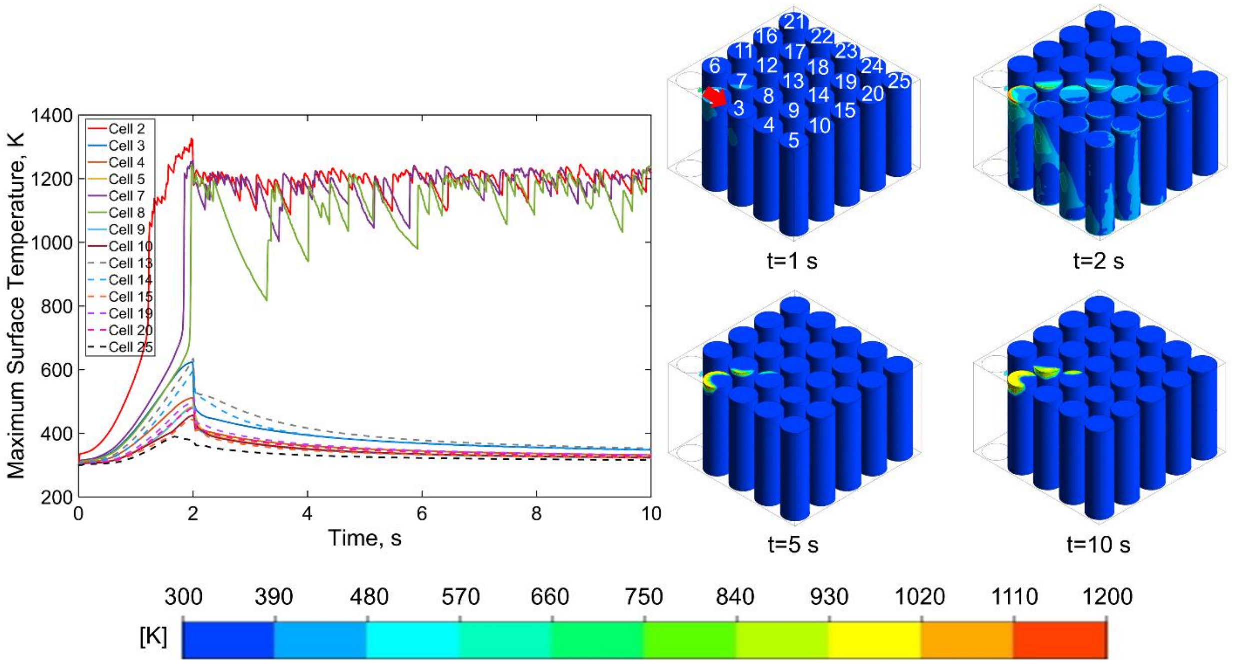

Figure 12: Effect of location of vent: Temperature plots for 1 mm overhead gap (0-2s) venting time and 7mm^2 vent placed at 63.5 mm height on curved surface of Cell 1 facing cell 2 for 4mm cell-cell gap.

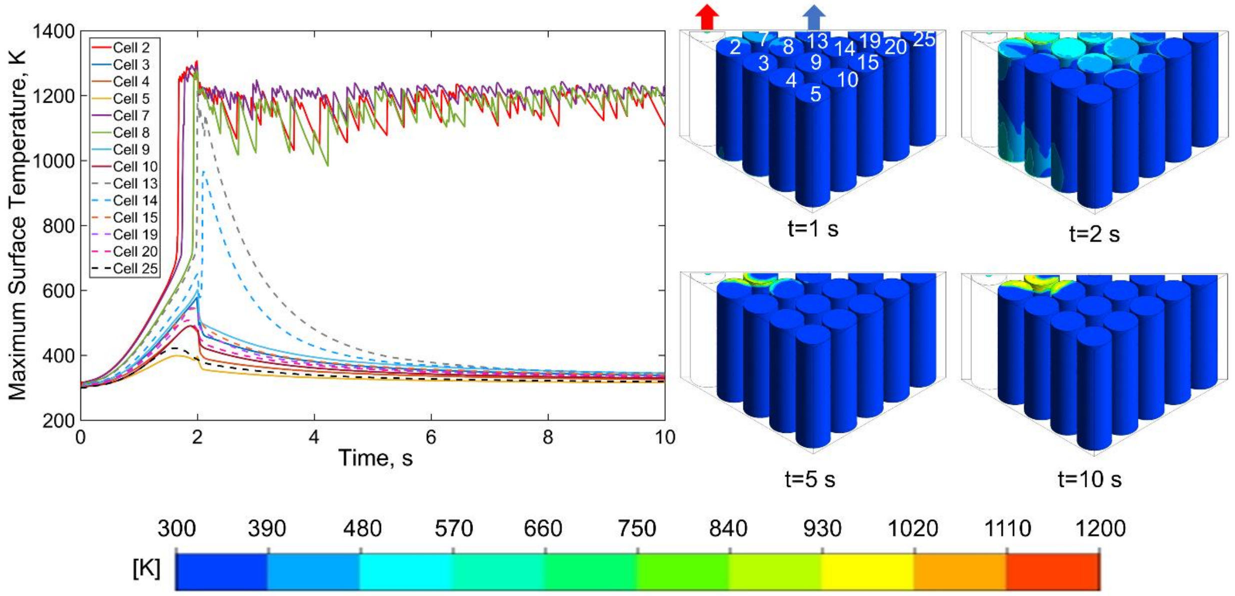

Figure 13: Effect of Outlet vent: Temperature plots for 1mm overhead gap (0-2s) venting time and 7mm^2 vent placed at center of top surface of Cell 1 for location of outlet vent above Cell 13.

References

1. T. M. Bandhauer, S. Garimella, and T. F. Fuller, *J. Electrochem. Soc.*, **158**, R1 (2011).

2. Q. Wang, P. Ping, X. Zhao, G. Chu, J. Sun and C. Chen, *J. Power Sources*, **208**, 210–224 (2012).

3. A. Melcher, C. Ziebert, M. Rohde, and H. J. Seifert, *Energies*, **9**, 292 (2016).

4. M. N. Richard and J. R. Dahn, *J. Power Sources*, **79**, 135–142 (1999).

5. E. P. Roth and D. H. Doughty, *J. Power Sources*, **128**, 308–318 (2004).

6. S. Santhanagopalan, P. Ramadass, and J. Z. Zhang, *J. Power Sources*, **194**, 550–557 (2009).

7. X. Feng, M. Fang, X. He, M. Ouyang, L. Lu, H. Wang and M. Zhang, *J. Power Sources*, **255**, 294–301 (2014).

8. C. F. Lopez, J. A. Jeevarajan, and P. P. Mukherjee, *J. Electrochem. Soc.*, **162**, A1905–A1915 (2015).

9. D. Mishra and A. Jain, *J. Electrochem. Soc.*, **168**, 20504 (2021).

10. Q. Li, C. Yang, S. Santhanagopalan, K. Smith, J. Lamb, L. A. Steele and L. Torres-Castro, *J. Power Sources*, **429**, 80–88 (2019).

11. L. Torres-Castro, A. Kurzawski, J. Hewson, and J. Lamb, *J. Electrochem. Soc.*, **167**, 090515 (2020).

12. K. S. Kshetrimayum, Y.-G. Yoon, H.-R. Gye, and C.-J. Lee, *Appl. Therm. Eng.*, **159**, 113797 (2019).

13. S. Wilke, B. Schweitzer, S. Khateeb, and S. Al-Hallaj, *J. Power Sources*, **340**, 51–59 (2017).

14. Z. An, K. Shah, L. Jia, and Y. Ma, *Appl. Therm. Eng.*, **160**, 113960 (2019).

15. T. Liu, C. Tao, and X. Wang, *Appl. Energy*, **267**, 115087 (2020).

16. X. Yang, Y. Duan, X. Feng, T. Chen, C. Xu, X. Rui, M. Ouyang, L. Lu, X. Han, D. Ren and Z. Zhang, *Fire Technol.*, **56**, 2579–2602 (2020).

17. L. Huang, Z. Zhang, Z. Wang, L. Zhang, X. Zhu and D. D. Dorrell, *J. Energy Storage*, **25**, 100811 (2019).

18. J. Lamb, C. J. Orendorff, L. A. M. Steele, and S. W. Spangler, *J. Power Sources*, **283**, 517–523 (2015).

19. J. K. Ostanek, W. Li, P. P. Mukherjee, K. R. Crompton, and C. Hacker, *Appl. Energy*, **268**, 114972 (2020).

20. P. T. Coman, S. Mátéfi-Tempfli, C. T. Veje, and R. E. White, *J. Electrochem. Soc.*, **164**, A1858–A1865 (2017).

21. P. J. Bugryniec, D. J. N. Davidson, and D. S. F. Brown, *J. Power Sources*, **474**, 228396 (2020).

22. D. Sturk, L. Rosell, P. Blomqvist, and A. A. Tidblad, *Batteries*, **5**, 1–17 (2019).

23. L. Yuan, T. Dubaniewicz, I. Zlochower, R. Thomas, and N. Rayyan, *Process Saf. Environ. Prot.*, **144**, 186–192 (2020).

24. G. Gachot, S. Grugeon, I. Jimenez-Gordon, G. G. Esheta, S. Boyanov, A. Lecocq, G. Marlair, S. Pilard and S. Laruelle, *Anal. Methods*, **6**, 6120–6124 (2014).

25. A. W. Golubkov, R. Planteu, G. Voitic, H. Wiltsche, C. Stangl, G. Fauler, A. Thaler and V. Hacker, *RSC Adv.*, **5**, 57171–57186 (2015).

26. J. Kim, A. Mallarapu, D. P. Finegan, and S. Santhanagopalan, *J. Power Sources*, **489**, 229496 (2021).

27. F. Austin Mier, M. J. Hargather, and S. R. Ferreira, *J. Fluids Eng. Trans. ASME*, **141**, 1–11 (2019).

28. W. Li, K. R. Crompton, C. Hacker, and J. K. Ostanek, *J. Energy Storage*, **32**, 101890 (2020).

29. L. Kong, X. Hu, G. Gui, Y. Su, and M. Pecht, *Fire Technol.*, **56**, 2565–2578 (2020).

30. B. A. Egan and J. R. Mahoney, *J. Appl. Meteorol. Climatol.*, **11**, 312–322 (1972).

31. C. Jia, K. Shing, and Y. C. Yortsos, *Water Resour. Res.*, **35**, 3239–3251 (1999).

32. S. R. Allmaras and F. T. Johnson, in *Seventh international conference on computational fluid dynamics (ICCFD7)*,, p. 1–11, Big Island, HI (2012).

33. S. Deck, P. Duveau, P. D'Espiney, and P. Guillen, *Aerosp. Sci. Technol.*, **6**, 171–183 (2002).

34. M. Parhizi, M. B. Ahmed, and A. Jain, *J. Power Sources*, **370**, 27–35 (2017).

35. G. H. Kim, A. Pesaran, and R. Spotnitz, *J. Power Sources*, **170**, 476–489 (2007).

36. S. J. Drake, D. A. Wetz, J. K. Ostanek, S. P. Miller, J. M. Heinzel and A. Jain, *J. Power Sources*, **252**, 298–304 (2014)

37. T. S. Bowling, *J. Atmos. Terr. Phys.*, **56**, 539–540 (1994).

38. T. Walker, S. C. Xue, and G. W. Barton, *J. Heat Transfer*, **132**, 1–6 (2010).

39. P. H. Oosthuizen and W. E. Carscallen, *Introduction to compressible fluid flow*, CRC press, (2013).

40. W. Li, H. Wang, Y. Zhang, and M. Ouyang, *J. Energy Storage*, **24**, 100775 (2019).

41. A. W. Golubkov, D. Fuchs, J. Wagner, H. Wiltsche, C. Stangl, G. Fauler, G. Voitic, A. Thaler and V. Hacker, *RSC Adv.*, **4**, 3633–3642 (2014).

42. I. H. Bell, S. Quoilin, J. Wronski, and V. Lemort, in *ASME ORC 2nd International Seminar on ORC Power Systems*, (2013).

43. F. M. White and I. Corfield, *Viscous fluid flow*, McGraw-Hill New York, (2006).

44. Z. Wang, N. Mao, and F. Jiang, *J. Therm. Anal. Calorim.*, **140**, 2849–2863 (2020).

CHAPTER 4

Investigation of the Impact of Radiative Shielding by Internal Partitions Walls on Propagation of Thermal Runaway in a Matrix of Cylindrical Li-Ion Cells

Li-ion cells and battery packs are commonly used for electrochemical energy storage and conversion. Despite favorable characteristics such as high capacity, low self-discharge rate and minimal memory effect,[1] Li-ion batteries suffer from several safety and reliability problems during operation, storage and transportation.[2] Thermal management of Li-ion battery packs is of critical importance because of the risk of thermal runaway at elevated temperatures.[3] Thermal runaway, which comprises a sequence of highly exothermic processes such as SEI decomposition, negative solvent reaction, positive solvent reaction and electrolyte decomposition reactions[4,5] can be triggered by mechanisms such as mechanical abuse[6], electrical abuse[7,8] and thermal abuse.[9] Preventing onset of thermal runaway in a cell and preventing propagation of thermal runaway from one cell to others in the battery pack are both critical to ensure overall safety.

Extensive literature is already available on theoretical/numerical and experimental investigation of thermal runaway propagation in a battery pack. The impact of geometrical design characteristics such as cell-to-cell gap, interstitial material and location of trigger cell on thermal runaway propagation has been studied through simulations.[10,11] An experimentally validated numerical study to prevent cell-to-cell thermal runaway propagation in a battery pack showed the importance of post-venting condensation of vented gases on neighboring cells on thermal runaway propagation.[12] Investigation of thermal management design tradeoffs to prevent thermal runaway propagation has been presented.[13] The importance of insulating layer around cells and a conductive heat sink in preventing thermal runaway propagation in a Li-ion battery pack has been demonstrated.[14] The impact of state-of-charge and packing arrangement of cells on thermal runaway propagation has been studied. . Numerical study of self-heating ignition of batteries in storage has been presented. A thermo-kinetic model to predict thermally induced failure of a Li-ion cell has been developed.

A number of papers on passive and active thermal management mechanisms to prevent and mitigate thermal runaway propagation are also available. An experimentally validated lumped computational model to prevent cascade propagation in the battery pack of pouch cells using cooling plates and fire walls was presented.[15] Use of 1 mm thick thermal resistant layers between adjacent batteries to prevent thermal runaway propagation is shown.[16] An experimental study on safety enhancement methods for battery module was presented with different interstitial materials. Effective suppression of thermal runaway propagation within 11 cells 18650 battery pack was observed with graphite composite and aluminum extrusion sheet.[17] Effectiveness of a passive mitigation technique to prevent thermal runaway propagation in a battery pack was investigated with insertion of different physical barriers such as ceramic fiber, intumescent material and double layer stainless steel.[18] Prevention of thermal runaway propagation during nail penetration by using phase change composite material has been shown.[19] Battery fire suppression using a clean agent has been demonstrated. Other thermal management mechanisms include water mist[20], integrated PCM and micro channel cooling[21] and combined PCM and liquid cooling.[22] Studies on nonflammable electrolyte,[23] flame retardant electrolyte,[24] additives[25] and use of thermal runaway inhibitors[26] to increase thermal stability of Li-ion batteries have been reported.

Most of the thermal management techniques summarized above, including those related to thermal barriers and metal plates focus on heat removal driven by thermal conduction and/or convection, with relatively limited literature available on the effect of radiative heat transfer. High cell surface temperature during thermal runaway makes direct cell-to-cell radiation an important heat transfer mechanism, and a critical factor in determining the thermal fate of the battery. The importance of radiative heat transfer in Li-ion cells has been noted in past work. For example, experimental measurements on $LiFePO_4$ pouch cells showed that 27% of the total heat exchange occurs due to radiative heat transfer.[27] In natural convection conditions, which is commonly the case for Li-ion battery packs, especially for transportation and storage, radiative heat transfer has been shown to be more significant than convective heat transfer.[28] While recognizing the importance of radiation during thermal runaway, however, there is insufficient work available on making use of available radiative heat transfer pathways to prevent thermal runaway propagation in Lithium-ion battery pack. The limited available work in this direction includes experimental results depicting improvement in tolerance of Li-ion cells to thermal abuse by virtue of radiation[29] and investigation of radiant barriers between prismatic cells in preventing thermal runaway propagation[30].

The analysis of radiation heat transfer in the context of thermal runaway propagation may present interesting trade-offs. For example, cells with low emissivity (and hence high reflectivity) are desirable due to the reduced tendency to absorb heat and prevent thermal runaway propagation. However, high emissivity may be favorable for preventing the onset of thermal runaway in the trigger cell. Further, careful design of the radiative properties of the internal partition commonly used to separate individual cells in a matrix of cells for storage/transportation (see Figure 1) may play an important role in preventing thermal runaway onset and propagation. Internal partitions, often made of cardboard, are already used in Li ion battery packaging, and therefore present an effective, easy-to-install and inexpensive mechanism for thermal management with minimal effect on energy density of the battery pack. There remains a critical need to investigate such radiative heat transfer-based mechanisms to enhance the thermal safety of a battery pack.

This work investigates the impact of radiative heat transfer on thermal response of Lithium Cobalt Oxide (LCO) 18650 cells during thermal abuse scenario using finite volume simulations. In particular, the role of radiative properties of the internal partition (see Figure 1) on onset and propagation of thermal runaway is studied. It is shown that careful choice of the radiative properties of cells as well as internal partition may help mitigate the propensity of cascade propagation in the battery pack. While high reflectivity of the cell may help prevent propagation to neighboring cells, the resulting low emissivity contributes towards thermal runaway onset in the trigger cell. Similarly, highly emissive walls of the internal partition may help in heat removal from the trigger cell. However, this may, in turn, exacerbate the safety of neighboring cells. Therefore, an optimal balance in these radiative properties may be helpful in ensuring overall thermal safety and to prevent thermal runaway onset and propagation in a battery pack.

4.1 Simulation set up

4.1.1 Geometry

The simulation geometry used in this work models a typical pack of cylindrical Li-ion cells during transportation and storage. A picture of a typical pack is shown in Figure 1(a), and a schematic of the simulation geometry is shown in Figure 1(b). The geometry comprises 25 18650 Li-ion cells placed in a 5×5 array enclosed in a box of overall dimensions 106 mm by 106 mm by 66 mm. The cells are segregated from each other using a thin internal partition of 1 mm thickness. The internal partition is typically made of wood/cardboard. The gap between each cell and internal partition is 1 mm. The overhead gap between cell top surface and the ceiling of the box is 1 mm. A heater of 1 mm thickness wrapped around the cell at the center of the pack (cell 13) provides thermal energy that triggers thermal runaway. The interstitial material around the cells is air.

Simulations carried out in this work account for multiple coupled physical phenomena, some of which may be non-linear. These include temperature-dependent heat generation due to Arrhenius decomposition reactions, surface-to-surface radiative heat transfer, anisotropic thermal conduction within cells, and natural convection within the battery pack. Modeling details pertaining to these processes are discussed in sub-sections below.

4.2 Governing Equations

4.2.1 Heat generation equations

Heat generation in each cell in the simulations occurs by virtue of four Arrhenius exothermic reactions –SEI decomposition, negative solvent reaction, positive solvent reaction, and electrolyte decomposition reaction – that are known to occur during thermal runaway[31,32] This cascade of highly temperature-dependent heat generating reactions is triggered by the joule heating in the heater, modeled as a volumetric heat source. Heat generation parameter values corresponding to $LiCoO_2$ cell chemistry are assumed[31] and are described in Table 1.

4.2.2 Thermal conduction and boundary conditions

The governing transient thermal conduction equation for each cell is given by

$$\frac{1}{r}\frac{\partial}{\partial r}\left(k_r r\frac{\partial T}{\partial r}\right) + \frac{k_\theta}{r^2}\frac{\partial^2 T}{\partial \theta^2} + k_z\frac{\partial^2 T}{\partial z^2} + q''' = \rho c_p\frac{\partial T}{\partial t} \tag{1}$$

Similarly, thermal conduction in interstitial and internal partition materials is written in cartesian coordinates as

$$\frac{\partial}{\partial x}\left(\frac{\partial T}{\partial x}\right) + \frac{\partial}{\partial y}\left(\frac{\partial T}{\partial y}\right) + \frac{\partial}{\partial z}\left(\frac{\partial T}{\partial z}\right) = \frac{\rho c_p}{k}\frac{\partial T}{\partial t} \tag{2}$$

Thermal properties of room-temperature air are assumed for the interstitial material. While internal partition materials vary widely in battery pack, a value of 0.153 $Wm^{-1}K^{-1}$ (see Table 2) representative of wooden materials, is used for the partition.

Each cell is modeled as cylindrical orthotropic material with thermal conductivity values of 0.2 $Wm^{-1}K^{-1}$, 32$Wm^{-1}K^{-1}$, and 32 $Wm^{-1}K^{-1}$ in radial, tangential, and axial directions respectively.[33] Thermophysical properties of various materials used are mentioned in Table 2. The outer walls of the box are subjected to a natural convection boundary condition with h=10 $Wm^{-2}K^{-1}$, which is representative of conditions expected in transportation/storage of the battery pack. Other boundary conditions implemented include the usual no-slip boundary condition at the outer walls.

4.2.3 Natural convection

Natural convection due to buoyancy of air may be important in the problem addressed here due to the large, anticipated temperature rise. Heating of air in the vicinity of a hot surface results in buoyancy driven flow around cells. Natural convection is modeled through temperature-dependent density of air. The gravity vector is defined as pointing downwards (negative *z* direction, referring to Figure 1(b)). Convective flow and heat transfer are governed by following conservation equations:

$$\frac{\partial \rho}{\partial t} + \nabla.(\rho \mathbf{V}) = 0 \tag{3}$$

$$\rho\left(\frac{\partial \mathbf{V}}{\partial t} + (\mathbf{V}.\nabla \mathbf{V})\right) = -\nabla.p + \mu\nabla^2\mathbf{V} + \rho\mathbf{g}\beta(T - T_\infty) \tag{4}$$

$$\frac{\partial T}{\partial t} + \mathbf{V}.\nabla T = \alpha\nabla^2 T \tag{5}$$

Viscous effects are neglected due to low velocity of air. Temperature dependent change in the density of air around cells is governed by volumetric thermal expansion coefficient, β in equation (4). Based on the ideal gas assumption, β for air can be expressed as:

$$\beta = -\frac{1}{\rho}\frac{\Delta\rho}{\Delta T} = \frac{1}{\rho}\frac{p}{R_u T^2} = \frac{1}{T} \tag{6}$$

4.2.4 Radiative heat transfer

Radiative heat transfer in the battery pack is accounted for through surface-to-surface radiation modeling which is based on gray-diffuse model.[34] This model assumes the radiative properties of a surface to be independent of wavelength and direction. In general, a surface that is highly emissive is also highly absorptive. The total radiative heat flux for each radiating surface in the geometry being simulated is calculated, which is further used in computing the energy equation described in the previous sub-section. Radiative heat transfer between any two surfaces is, in general, a function of temperature of the respective surfaces, size, relative orientation, and distance between surfaces. View factors are commonly used to characterize these factors.[34] In the present simulations, view factors between pairs of surfaces are calculated using ray tracing method[35] while the air between surfaces is assumed to be non-participating. All radiating surfaces are assumed to be opaque (zero transmissivity) therefore, sum of emissivity and reflectivity for each surface is unity. Radiative flux leaving a surface comprises of Stefan Boltzmann emission by virtue of its temperature and reflected radiative flux, which depends on irradiation flux from all visible surfaces in the surroundings. The irradiation flux is the net sum of radiation energy from all surrounding surfaces participating in the radiation exchange and is directly proportional to the view factors. Such surface-to-surface radiation calculations become computationally expensive due to large number of radiating surfaces. Therefore, surface clusters are created by grouping adjacent surfaces until a specified number of surfaces per cluster, five in this case, is reached. Clustering of radiating surfaces is an approximation that balances computational cost with accuracy. Radiosity, which is defined as the total radiation energy leaving a surface per unit time and per unit area is calculated for each surface cluster and these values are distributed on to the radiating faces.

In order to validate the radiation model, a special case is considered with a geometry that is representative enough of a battery pack with partitions, yet simple enough to admit an exact solution for radiation heat transfer. Specifically, a cell of radius R surrounded by partition walls in an enclosure of size L by W is considered. The cell is offset by a distance w from the left wall. For this case, assuming all bodies are opaque black bodies, the exact analytical solution for radiative heat flux into the left wall is given by

$$q''_{\mathrm{cyl-wall}} = \frac{1}{\pi}\tan^{-1}\left[\frac{L}{2(w+R)}\right]\sigma\left[T_{\mathrm{cyl}}{}^{4} - T_{\mathrm{wall}}{}^{4}\right] \tag{7}$$

where σ is the Stefan-Boltzmann constant and emissivity, respectively.

For this scenario, Figure 2(a) compares the computed radiative heat flux at the left wall with the analytical solution given by equation (7) as a function of *R*. Values of other geometrical parameters are w=300 mm, W=700 mm, L=400 mm. Both cell and walls are assumed to be opaque black bodies. Figure 2(b) presents a similar comparison as a function of cell temperature, while holding wall temperature at 300 K. Other geometrical parameters are the same as in Figure 2(a), in addition to *R*=150 mm. Both plots show excellent agreement between the radiation model and the analytical solution for this special case.

In addition, validation of other heat transfer models, such as thermal conduction and heat generation used here has been carried out by comparison with an analytical solution. More details of this comparison have been described in a recent paper [10].

4.2.5 Meshing and other simulation details

3D polyhedral mesh elements are used throughout this work. Polyhedral meshing results in each meshed element being surrounded by a greater number of elements compared to other meshing techniques, resulting in better gradient approximation. Polyhedral meshing also results in high numerical stability and low numerical diffusion. In this work, one meshed cell per gap is used for surface mesh sizing with proximity control type and three-layered boundary inflation control for each meshed cell. The maximum mesh element size is 0.05 mm, 0.1 mm and 0.5 mm for the internal partition, cells and the outer box, respectively. Contact meshing is used to enhance convergence at the intersection between the box and internal partition. The generated mesh is characterized by 1.05 growth rate and 0.33 squish index. For a 5 by 5 battery pack, upwards of 8.2

million elements are used along with a time step of 1 ms, based on a grid independence study described in the next section. Nonlinear coupled solver using implicit numerical approach with 0.001s timestep size and 0.0001 tolerance limit is used. Convergence in these simulations is found to require 600 energy iterations and 5 faces per surface cluster. Figure 3 presents representative pictures of the final mesh using in this work. Figure 3(a) shows a two-dimensional projection of the 3D mesh for the entire 25-cell battery pack, whereas a zoomed-in picture showing only the trigger cell, the surrounding heater and the partition walls around the trigger cell is shown in Figure 3(b).

Note that the present work does not account for combustion of the vent gases and/or cell and partition materials. Heat spreading by advection due to vented gases is also not considered, although this has been modeled in a prior study [11].

4.3 Results and discussion

A Multiphysics, finite-volume based computational simulation is developed to account for the physical processes described in the previous section. Validation of this general simulation framework has been carried out by comparison with analytical solutions for simplified special case of single cell thermal abuse, as described in previous work.[10]

A number of simulations are carried out in the present work to understand the role of the internal partition and specifically its radiative properties on thermal runaway propagation in the battery pack. Table 3 summarizes the goals, parameter values, and key conclusions of the simulations, which are discussed in detail in this Section.

The first set of simulations (Simulation A) establish timestep sensitivity of the simulations. Selection of timestep is an important tradeoff between computational efficiency and accuracy. A small timestep is preferred for smooth convergence and maintaining residuals within tolerance limit, particularly for simulations involving highly non-linear PDEs, such as the present case. However, a small timestep may also result in significant computational cost. In the first set of simulations, temperature distribution for the geometry described above is computed, with 8.5×10^6 Wm^{-3} heat generation in the sleeve heater up to 200s and with three different timesteps of 10, 1 and 0.5 ms. The computed core temperatures of trigger cell (cell 13) and cell 3 are shown in Figures 4(a) and 4(b) respectively for each case. For both cells, the predicted temperature distribution is independent of the time steps considered here. Therefore, a 1 ms fixed timestep is used for all subsequent simulations.

Similarly, grid independence study (Simulation B) is carried out to determine the minimum number of grid elements needed to ensure grid independence of results. Figures 5(a) and 5(b) plot core temperatures of trigger cell and cell 3, respectively as functions of time for three different numbers of grid elements. While there is a significant change in the computed results when the grid is refined from 4.6 to 8.2 million elements, there is much lesser change when the grid is further refined to 10.1 million elements. Between the 8.2 and 10.1 million element cases, the peak temperature and time of occurrence of the peak change by less than 3%. This shows that upwards of 8.2 million grid elements must be used to ensure accuracy of simulation results. This is a rather large number and underscores the importance of computational optimization when carrying such non-linear simulations.

The effect of the presence of internal partition that separates each cell in the battery pack is investigated next. These simulations (Simulation C) test the hypothesis that, with appropriate radiative properties of the partition surfaces, heat generated in the trigger cell can be prevented from radiating to neighboring cells, thereby, preventing propagation. A set of simulations without and with partitions is carried out. For the simulations with partition, the partition material is assumed to be wood, with emissivity of 1.0, which may correspond to a dark-colored partition. While the intrinsic emissivity of wood/cardboard is slightly lower, the surface emissivity can be modified by paint, and an emissivity close to 1 can be obtained by painting black. The extreme case of emissivity of 1.0 is taken here to demonstrate the effect of emissivity on thermal runaway characteristics. The same values of all other parameters, such as cell-to-cell gap and reaction parameters are used in both simulations. Particularly, heat generation rate in the sleeve heater around the trigger cell responsible for onset of thermal runaway is taken to be 4.7×10^{6} Wm^{-3} up to 500 s. Emissivity of each cell is taken to be 0.1, which is reasonable because cells usually have a shiny, metallic surface that is highly reflective. Simulation results are presented in Figures 6 and 7 in the form of temperature plots and colorplots at 400 s, 800 s and 1000 s, respectively. Corresponding videos of the evolution of the temperature field over time for Simulation C (and all subsequent simulations) are available in Supplementary Information. These videos are labeled by Simulation number and have been slowed down by 0.25 X for clarity. Figure 6 shows that, in the absence of the partition, neighboring cells 8 and 7 both undergo thermal runaway following the trigger cell. This is mainly due to direct radiative heat exchange between the trigger cell and its neighboring cells. In contrast, in the presence of the partition, while the trigger cell does undergo thermal runaway, there is no propagation to neighboring cells. The absence of propagation in this case is primarily due to the high emissivity (and therefore high absorptivity) of the partition walls, which absorb a significant amount of heat from the trigger cell and prevent the heat to radiatively transfer directly to the neighboring cells. In addition to the prevention of propagation to neighbors, Figure 6(b) also shows delayed thermal runaway in the trigger cell itself compared to the baseline case (Figure 6(a)), which is also due to the presence of the partition that radiatively absorbs a significant amount of heat from the trigger cell. Note that the trigger cell temperature plot in Figure 6(a) shows a few inflexion points. In addition to the sharp peak corresponding to occurrence of thermal runaway, there is an inflexion in the trigger cell curve at t=500 s, corresponding to the termination of sleeve heating, and at around t=815 s and t=910 s, when heat generated by thermal runaway in neighboring cells cause small bumps in the trigger cell curve.

Even though the internal partition may absorb significant heat from the trigger cell, as demonstrated above, it is important for such heat to be transported away from the battery pack, otherwise the internal partition will simply re-emit the heat back to the trigger cell and neighboring cells. High thermal conductivity of the partition material may enable conduction of heat to the outer box, from where, heat may be removed to the ambient. A set of simulations (Simulation D) are carried out to understand the impact of thermal conductivity of the partition on thermal runaway characteristics. In these simulations, 4.5×10^{6} Wm^{-3} internal heat generation up to 300 s is considered. Cells and partition emissivities are taken to be ε_c=0.1and ε_p =0.1. Two different partition materials – wood and aluminum – are considered. Wood and aluminum are representative of low and high thermal conductivity materials, respectively, with typical values of 0.153 $Wm^{-1}K^{-1}$ and 202.4 $Wm^{-1}K^{-1}$, respectively. Results are plotted in Figures 7(a) and 7(b) respectively. Corresponding temperature contours are shown in Figure 8, and complete videos of the evolution of the temperature field are provided as Supplementary Information. Figures 8(a) and 8(b) show that for the abuse condition considered here, both wood and aluminum are able to prevent propagation of thermal runaway to neighboring cells. The outcome in the case of Aluminum partition is even more desirable because in this case, even onset in the trigger cell is prevented, because the high thermal conductivity aluminum is able to diffuse away the radiative heat received from the trigger cell, and thereby prevent altogether the onset of thermal runaway in the trigger cell. Local accumulation of heat in the partition around trigger cell can be clearly seen for the case of wood partition (Figure 9(a)). In contrast, heat rapidly diffuses away from the trigger cell along the partition material in the high thermal conductivity aluminum case. This also helps in rapid distribution of heat absorbed from trigger cell to larger number of neighboring cells, which may reduce the thermal load on each neighbor, and therefore, propagation of thermal runaway. These plots show that at high thermal conductivity, the partition effectively acts like a thermal fin by providing a conduit for heat to diffuse away from the trigger cell. The higher the thermal conductivity of the partition, the more effective is its performance as a fin. An important trade-off to consider here, however, is that high thermal conductivity metals also tend to be heavier, and, therefore, may impact the overall energy storage density of the battery pack.

Surface emissivity is the key thermal property that determines the extent of heat that is radiatively absorbed or reflected from a surface. The higher the emissivity, the higher is the rate of heat absorption, and lower is the rate of reflection of heat. The next two sets of simulations examine the impact of partition and cell emissivities on thermal runaway propagation.

First, a set of simulations (Simulation E) is carried out using wood partition with an emissivity of 0.1 and 1.0. All other parameters are held constant, including a cell emissivity of 0.1 and heat generation of 4.5×10^{6} Wm^{-3} internal heat generation up to 300 s. Results are summarized in Figure 10 as lines plots, and in Figure 11 as colorplots of the temperature field. Corresponding videos of the temperature distribution evolution are presented in Supplementary Information. These results show that while there is no propagation of thermal runaway in either case, it is still desirable to have high emissivity of the partition material. As shown in Figure 10(b), high partition emissivity enables significant heat absorption from the trigger cell, which prevents thermal runaway from occurring altogether. In the low emissivity partition case, thermal runaway does occur in the trigger cell due to insufficient absorption of heat from the trigger cell. High emissivity of the internal partition can be achieved simply by choosing a dark colored material, or by painting over with a dark colored paint. This passive, inexpensive approach may result in significant thermal benefit without adding significantly to the system weight.

It is interesting to evaluate the importance of radiative heat transfer by comparing the radiative heat flux received by the partition wall with the total heat flux received. These heat flux values are plotted in Figure 12 as functions of time for the two cases considered in Simulation E discussed above. These plots show that radiative heat transfer peaks at the point of thermal runaway, similar to total heat transfer, and can be a significant component of total heat transfer.

Finally, the effect of emissivity of the cell on thermal runaway propagation is investigated. For this purpose, two simulations (Simulation F) with ε_c=1 and ε_c=0.1 are carried out. A wood partition with emissivity of 0.1, and 1.2×10^7 Wm^{-3} heat generation in the heater up to 500 s is considered in both cases. All other parameters are also constant, as listed in Table 3. High cell emissivity may be desirable to enable the trigger cell to lose as much heat as possible to prevent thermal runaway onset. However, high emissivity also results in the neighboring cells absorbing more heat from other radiative sources, such as the partition. For the purpose of minimizing radiative heat intake from neighboring sources, low emissivity may be desirable. A trade-off, therefore, clearly exists. Results presented in Figures 13 and 14 show that for the specific thermal abuse considered here, propagation of thermal runaway does occur for both cases. However, high emissivity of cells results in somewhat delayed onset for trigger cell but faster thermal runaway propagation. This is explained on the basis of enhancement in radiative heat transfer due to increased emissivity. This increased heat transfer rate results in delayed thermal runaway onset for the trigger cell as much of the internally generated heat is emitted away. However, increased emissivity (and hence absorptivity) also results in greater heat absorption by the neighboring cells, resulting in faster propagation. On the other hand, low emissivity results in increased reflectivity, due to which, thermal runaway in the trigger cell occurs earlier, but propagation to neighboring cells is delayed.

List of Figures

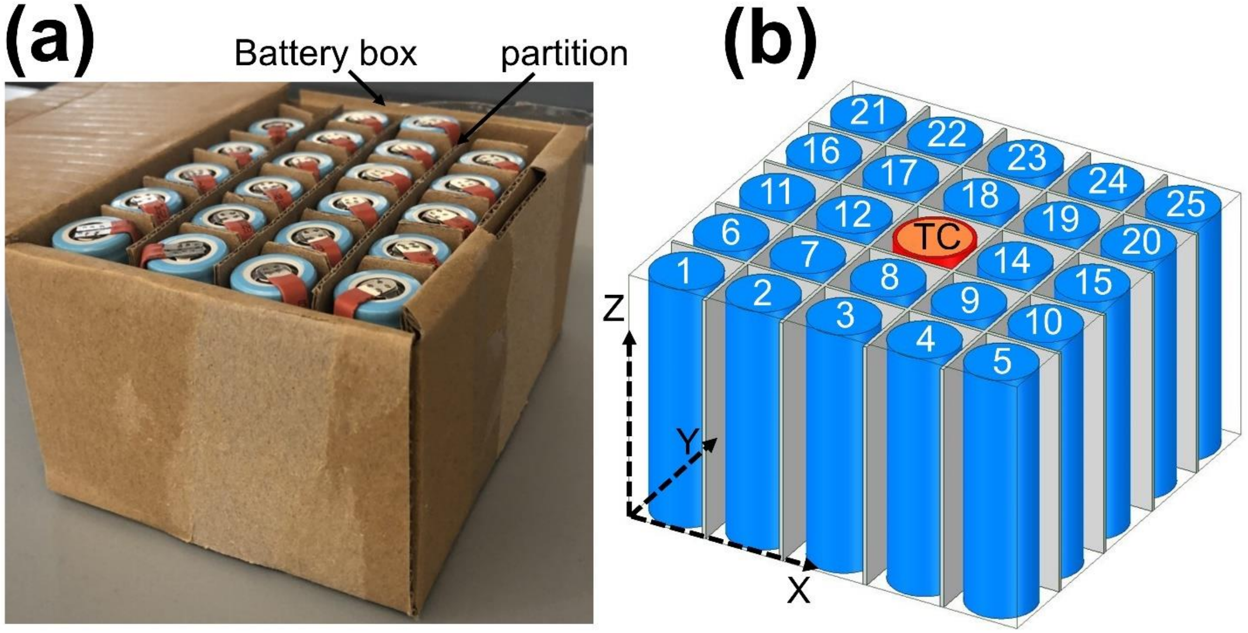

Figure 1. Schematic of 18650 Li-ion battery pack containing cells: (a) Photograph of a typically box of cells separated by internal partitions. (b) Geometry of the simulated battery pack showing 1 mm thick internal partition and trigger cell at position 13.

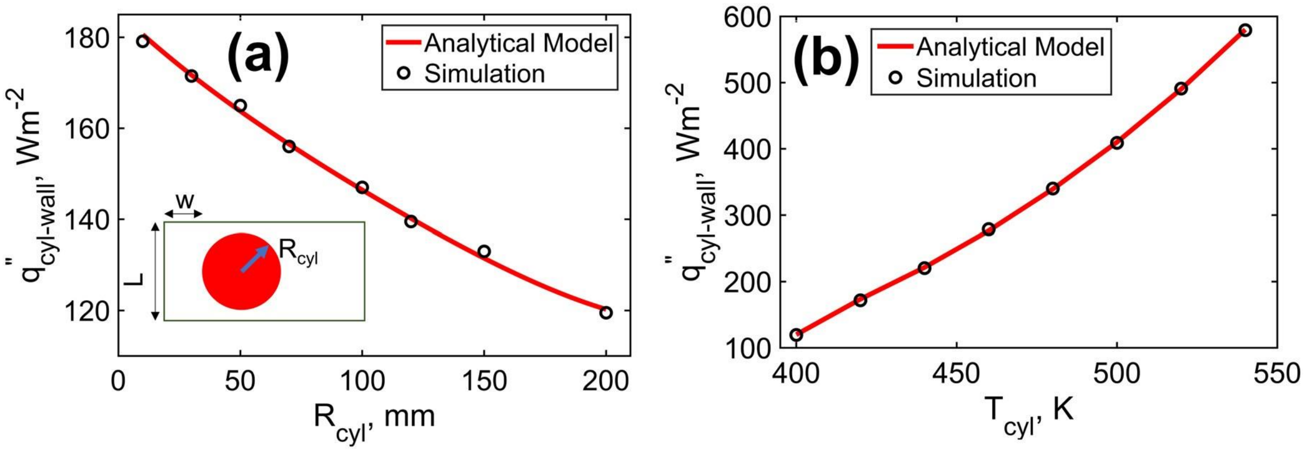

Figure 2. Validation of the radiation model: (a) Radiative heat flux between the left wall and the cell in an enclosure as a function of cell radius, *e*. (b) Radiative heat flux between the left wall and the cell in an enclosure as a function of cell temperature, while keeping wall temperature and cell radius at 300 K and 150 mm, respectively. Geometrical parameters are *L*=400 mm, *W*=700 mm, *w*=300 mm. All bodies are assumed to be opaque, black bodies.

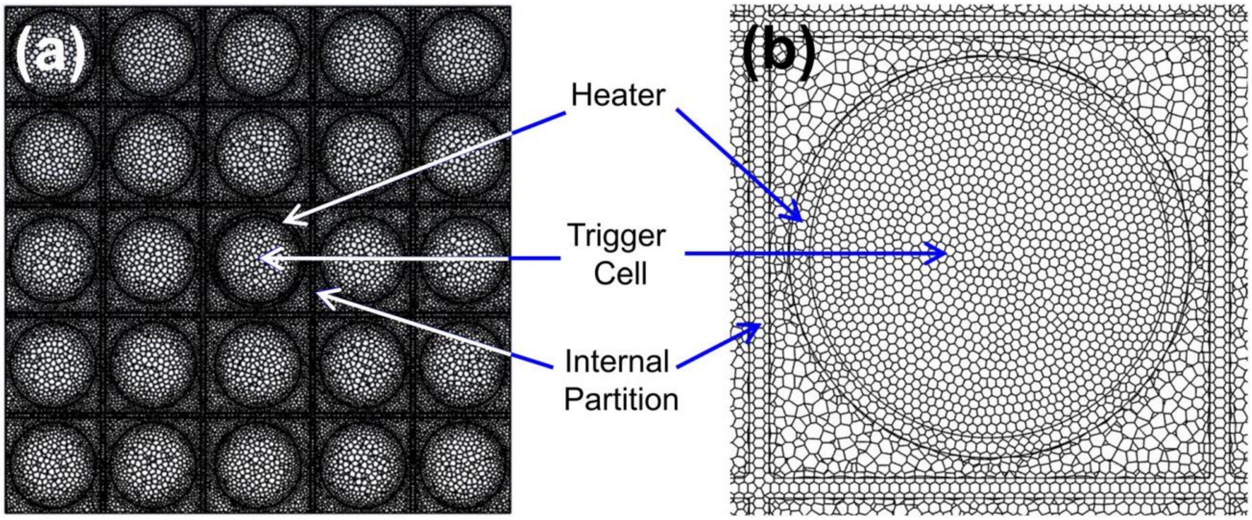

Figure 3. Pictures showing the representation mesh in cross-section view with (a) entire geometry, (b) zoomed-in to show only a small region around the trigger cell.

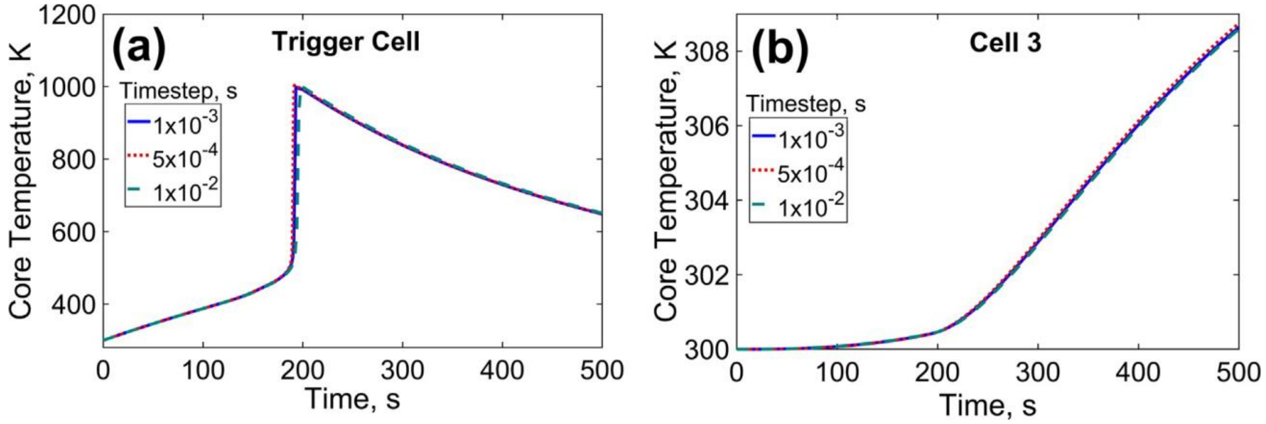

Figure 4. Simulations results to establish timestep sensitivity (Simulation A): Temperature vs time plot for (a) trigger cell, and (b) cell 3 in 5 by 5 battery pack. Problem parameters include 3 mm cell-to-cell gap, 1 mm overhead gap, 8.5×10^6 Wm^{-3} heat generation in heater up to 200 s, $\varepsilon_p = 0.1$, $\varepsilon_c = 0.1$.

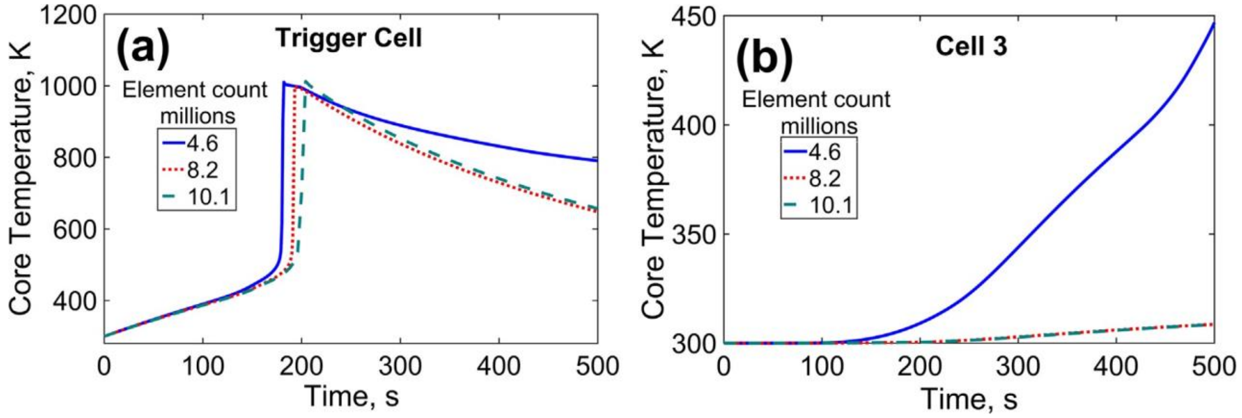

Figure 5. Simulations results to establish grid sensitivity (Simulation B): Temperature vs time plot for (a) trigger cell, and (b) cell 3 in 5 by 5 battery pack. Problem parameters are the same as Figure 2.

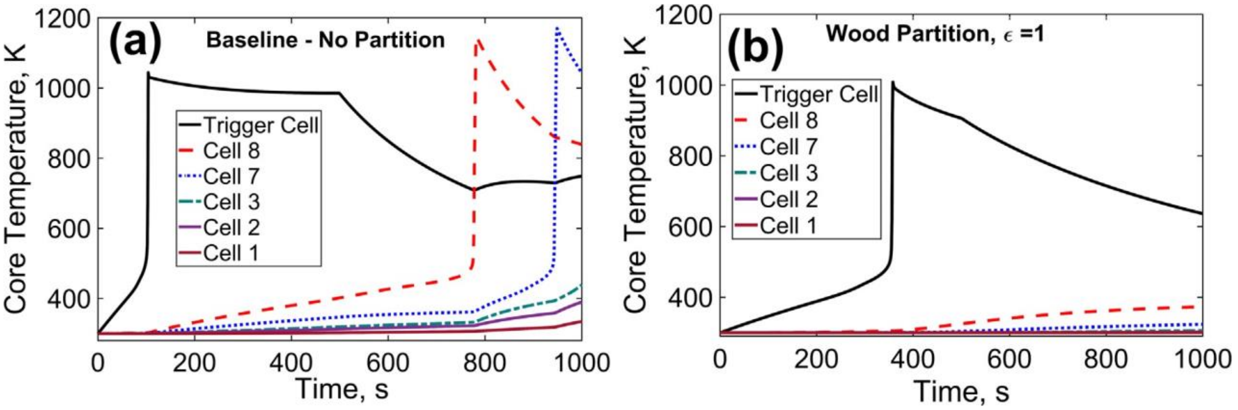

Figure 6. Effect of presence of internal partition (Simulation C): Temperature vs time plot for battery pack (a) without partition, (b) with wood partition. Problem parameters include 3 mm cell-to-cell gap, 1 mm overhead gap, 4.7×10^{6} Wm^{-3} heat generation in heater up to 500 s, $\varepsilon_p = 1$, $\varepsilon_c = 0.1$.

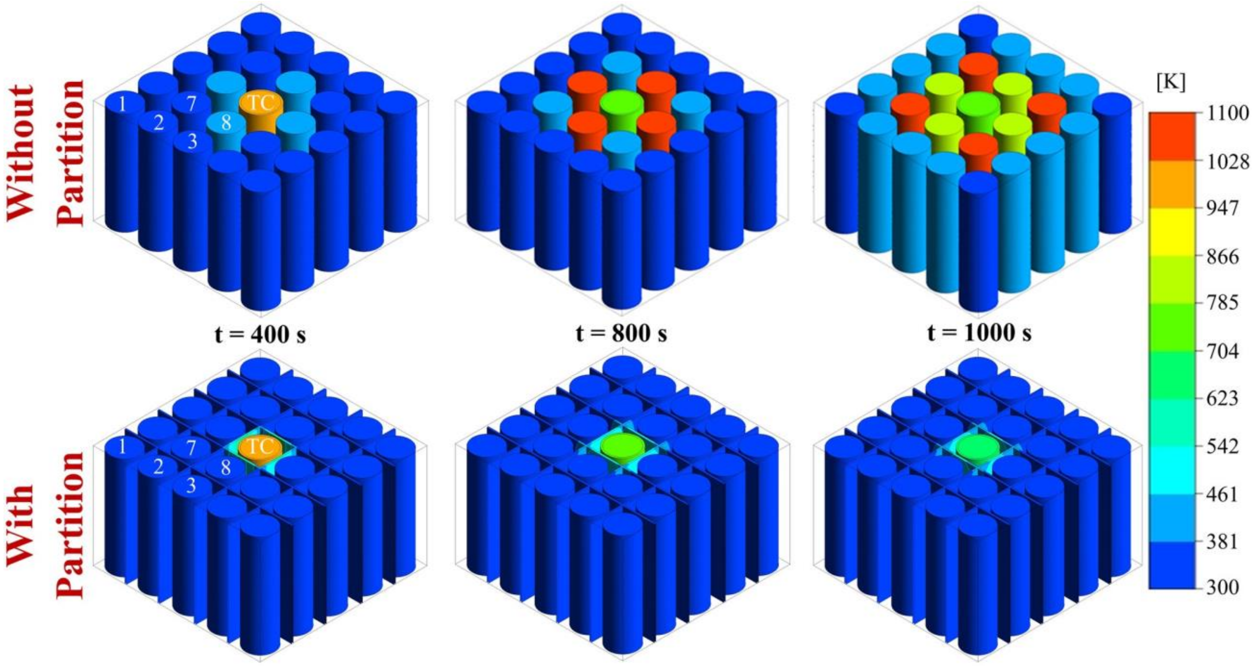

Figure 7. Color plots to demonstrate the impact of presence of internal partition on thermal runaway propagation. The problem parameters correspond to Figure 4.

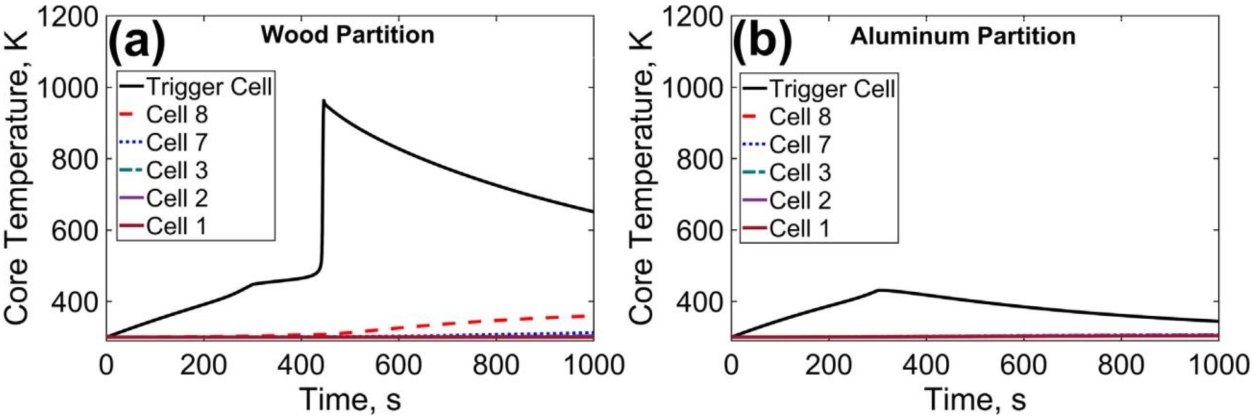

Figure 8. Effect of thermal conductivity of the internal partition material (Simulation D): Temperature vs time plot for battery pack with (a) wood partition, (b) aluminum partition. Problem parameters include 3 mm cell-to-cell gap, 1 mm overhead gap, 4.5×10^{6} Wm^{-3} heat generation in heater up to 300 s, $\varepsilon_p = 1$, $\varepsilon_c = 0.1$.

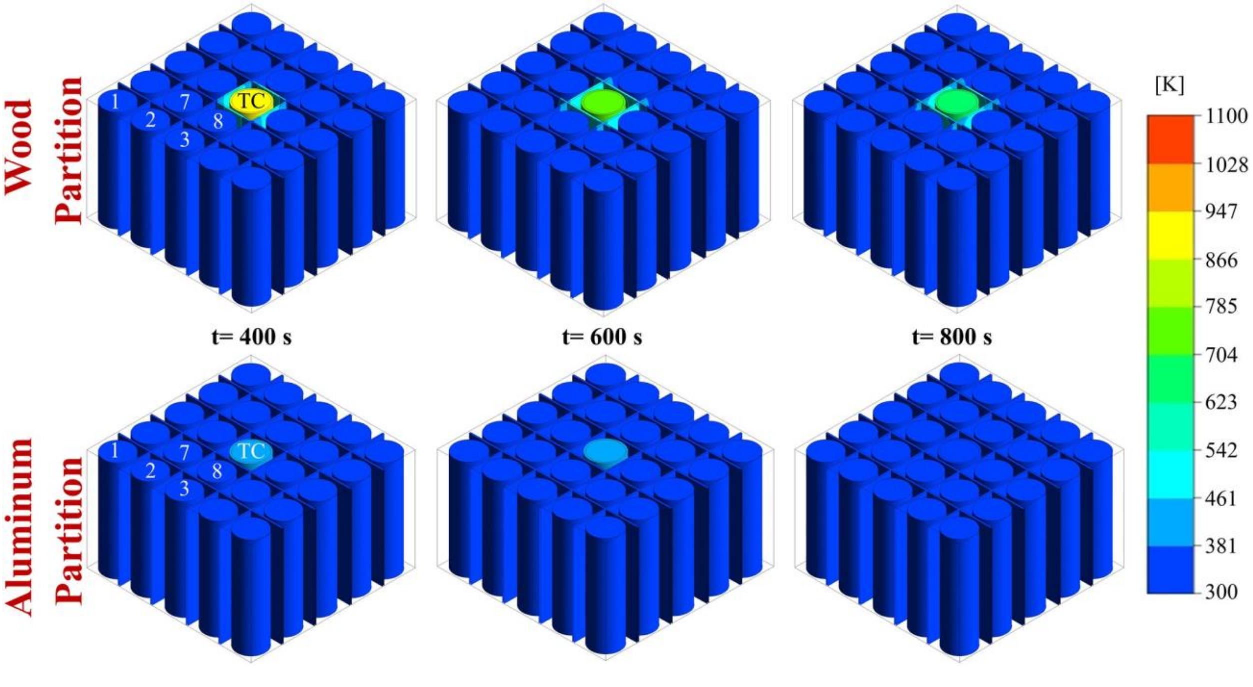

Figure 9. Color plots to demonstrate the impact of internal partition material on thermal runaway propagation. The problem parameters correspond to Figure 6.

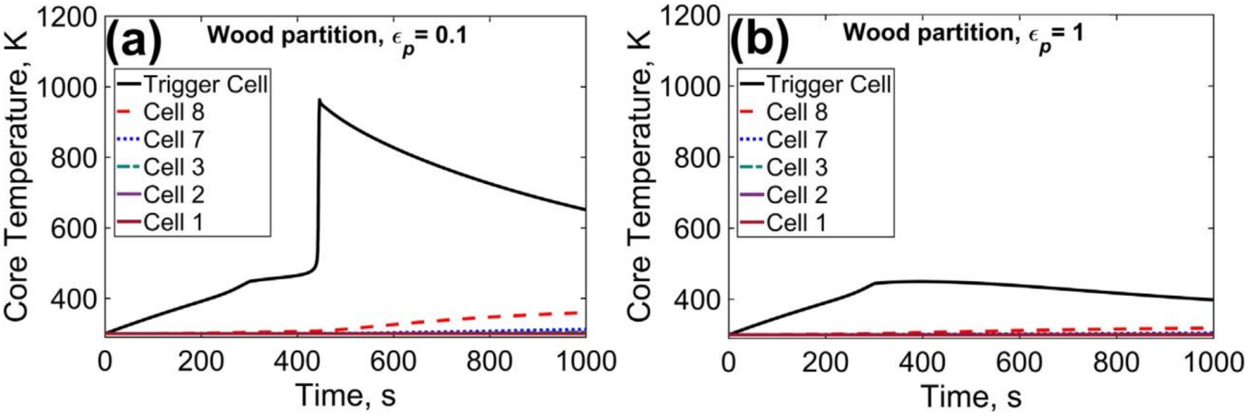

Figure 10. Effect of internal partition emissivity, ε_p (Simulation E). Temperature vs time plots for battery pack with (a) ε_p = 0.1; (b) ε_p = 1. Other problem parameters are the same as Figure 6.

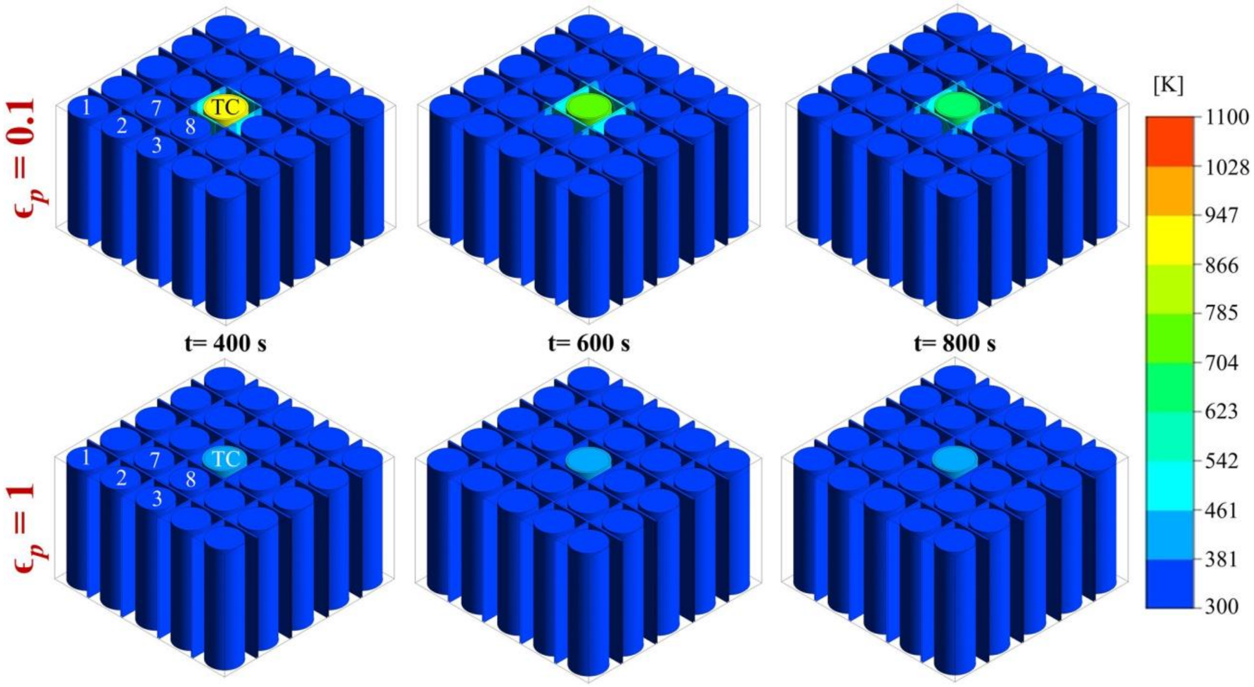

Figure 11. Color plots to demonstrate the effect of internal partition emissivity on thermal runaway propagation. The problem parameters correspond to Figure 8.

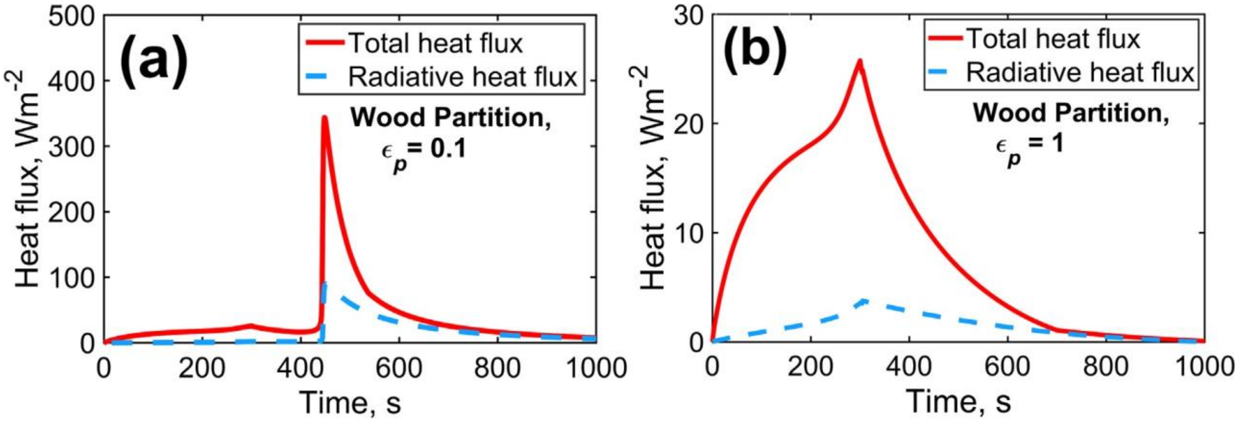

Figure 12. Comparison of radiative heat flux incident on the partition walls with total heat flux as a function of time for the two emissivity values considered in Figure 8.

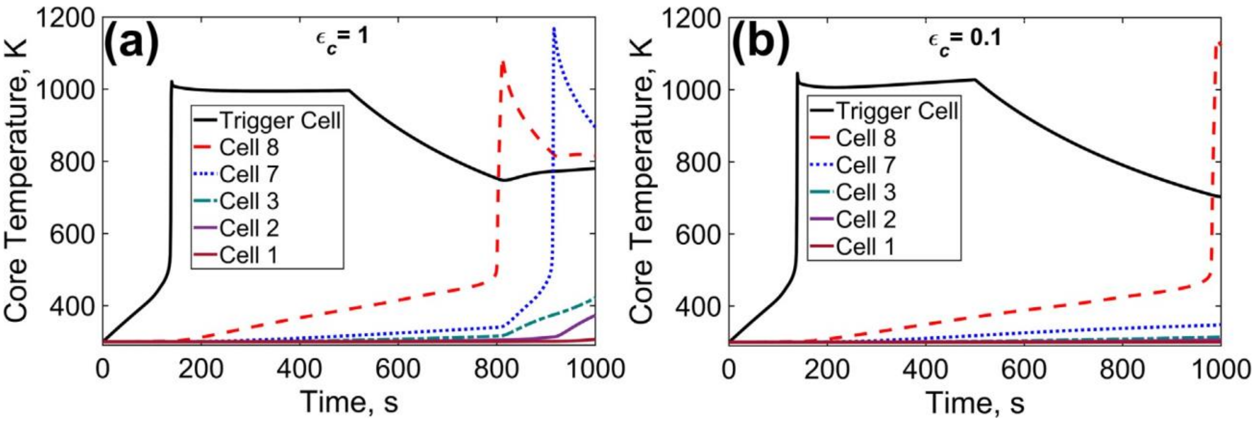

Figure 13. Effect of cell emissivity, ε_c (Simulation F): Temperature vs time plot for battery pack with (a) $\varepsilon_c = 1$, (b) $\varepsilon_c = 0.1$. Problem parameters include 3 mm cell-to-cell gap, 1.2×10^7 Wm^{-3} heat generation in heater up to 500 s, $\varepsilon_p = 0.1$.

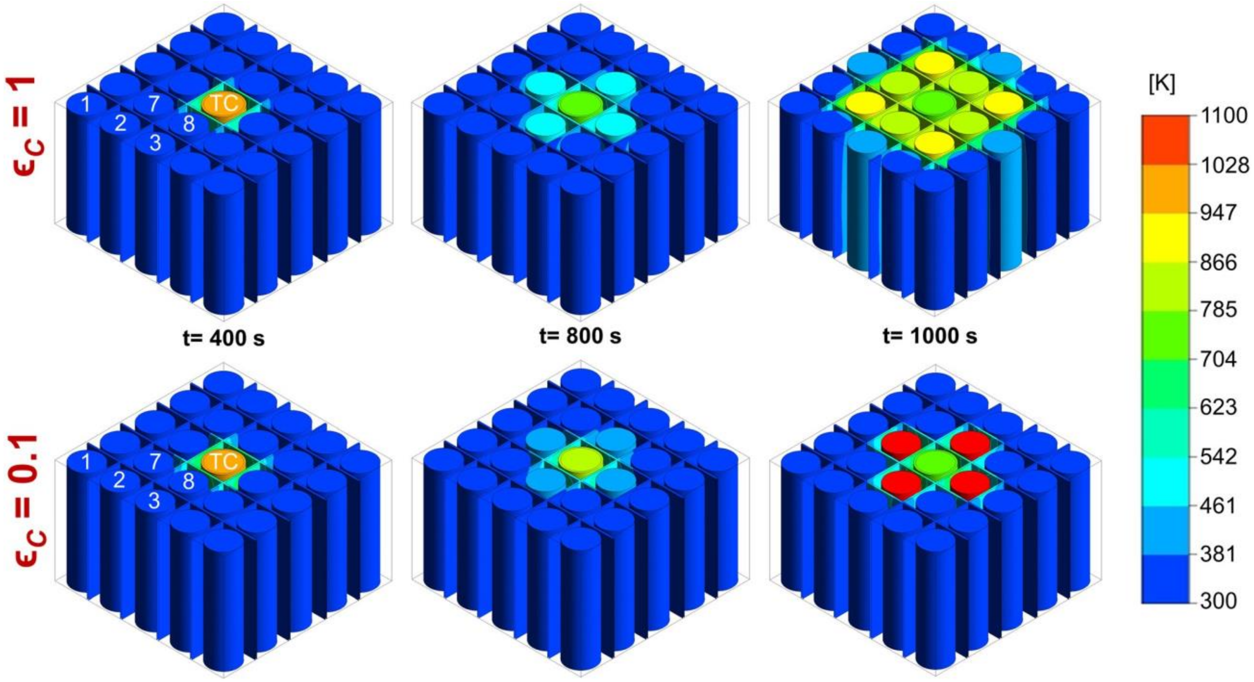

Figure 14. Color plots to demonstrate the effect of cell emissivity on thermal runaway propagation. The problem parameters correspond to Figure 10.

References

1. B. Diouf and R. Pode, Renew. Energy, 76, 375 (2015).

2. D. Lisbona and T. Snee, Process Saf. Environ. Prot., 89, 434 (2011).

3. X. Feng, M. Ouyang, X. Liu, L. Lu, Y. Xia, and X. He, Energy Storage Mater., 10, 246 (2018).

4. R. Spotnitz and J. Franklin, J. Power Sources, 113, 81 (2003).

5. I. Esho, K. Shah, and A. Jain, Appl. Therm. Eng., 145, 287 (2018).

6. T. Yokoshima, F. Maeda, T. Osaka, K. Takazawa, S. Egusa, S. Naoi, S. Ishikura, and K. Yamamoto, J. Power Sources, 393, 67 (2018).

7. L. Huang, Z. Zhang, Z. Wang, L. Zhang, X. Zhu, and D. D. Dorrell, J. Energy Storage, 25, 100811 (2019).

8. A. W. Golubkov, S. Scheikl, R. Planteu, G. Voitic, H. Wiltsche, C. Stangl, G. Fauler, A. Thaler, and V. Hacker, RSC Adv., 5, 57171 (2015).

9. D. Ren, X. Feng, L. Liu, H. Hsu, L. Lu, L. Wang, X. He, and M. Ouyang, Energy Storage Mater., 34, 563 (2021).

10. D. Mishra and A. Jain, J. Electrochem. Soc., 168, 020504 (2021).

11. D. Mishra, K. Shah, and A. Jain, J. Electrochem. Soc., 168, 060555 (2021).

12. R. Srinivasan et al., J. Electrochem. Soc., 167, 020559 (2020).

13. C. F. Lopez, J. A. Jeevarajan, and P. P. Mukherjee, J. Electrochem. Energy Convers. Storage, 13, 031007 (2016).

14. P. T. Coman, E. C. Darcy, C. T. Veje, and R. E. White, Appl. Energy, 203, 189 (2017).

15. C. Lee, A. O. Said, and S. I. Stoliarov, Transp. Res. Rec., 2673, 408 (2019).

16. D. Ouyang, J. Liu, M. Chen, J. Weng, and J. Wang, Appl. Sci., 8, 1263 (2018).

17. X. He, Z. Hu, F. Restuccia, H. Yuan, and G. Rein, Appl. Therm. Eng., 197, 117349 (2021).

18. X. Liu, Z. Wu, S. I. Stoliarov, M. Denlinger, A. Masias, and K. Snyder, J. Electrochem. Soc., 165, A2909 (2018).

19. F. Larsson, J. Anderson, P. Andersson, and B.-E. Mellander, J. Electrochem. Soc., 163, A2854 (2016). 20. X. Feng, X. He, M. Ouyang, L. Lu, P. Wu, C. Kulp, and S. Prasser, Appl. Energy, 154, 74 (2015).

21. C. Yuan, Q. Wang, Y. Wang, and Y. Zhao, Appl. Therm. Eng., 153, 39 (2019).

22. C. Lee, A. O. Said, and S. I. Stoliarov, J. Electrochem. Soc., 167, 090524 (2020).

23. S. Wilke, B. Schweitzer, S. Khateeb, and S. Al-Hallaj, J. Power Sources, 340, 51 (2017).

24. A. O. Said and S. I. Stoliarov, Fire Saf. J., 121, 103296 (2021).

25. T. Liu, J. Hu, C. Tao, X. Zhu, and X. Wang, Fire Saf. J., 120, 103117 (2021).

26. A. O. Said, A. Garber, Y. Peng, and S. I. Stoliarov, Fire Technol., 57, 1 (2021).

27. K. S. Kshetrimayum, Y.-G. Yoon, H.-R. Gye, and C.-J. Lee, Appl. Therm. Eng., 159, 113797 (2019).

28. W. Zhang, Z. Liang, X. Yin, and G. Ling, Appl. Therm. Eng., 184, 116380 (2021).

29. K. Xu, M. S. Ding, S. Zhang, J. L. Allen, and T. R. Jow, J. Electrochem. Soc., 149, A622 (2002).

30. Y. E. Hyung, D. R. Vissers, and K. Amine, J. Power Sources, 119–121, 383 (2003).

31. D. H. Doughty, E. P. Roth, C. C. Crafts, G. Nagasubramanian, G. Henriksen, and K. Amine, J. Power Sources, 146, 116 (2005).

32. B. K. Mandal, A. K. Padhi, Z. Shi, S. Chakraborty, and R. Filler, J. Power Sources, 161, 1341 (2006).

33. M. C. Niculuţă and C. Veje, J. Phys. Conf. Ser., 395, 012013 (2012).

34. W. Allafi, C. Zhang, K. Uddin, D. Worwood, T. Quang, D. Pedro, A. Ormeno, K. Li, and J. Marco, Appl. Therm. Eng., 143, 472 (2018).

35. T. D. Hatchard, D. D. MacNeil, D. A. Stevens, L. Christensen, and J. R. Dahn, Electrochem. Solid-State Lett., 3, 305 (2000).

36. C. F. Lopez, J. A. Jeevarajan, and P. P. Mukherjee, J. Electrochem. Soc., 162, A1905 (2015).

37. G. H. Kim, A. Pesaran, and R. Spotnitz, J. Power Sources, 170, 476 (2007).

38. M. Parhizi, M. B. Ahmed, and A. Jain, J. Power Sources, 370, 27 (2017).

39. S. J. Drake, D. A. Wetz, J. K. Ostanek, S. P. Miller, J. M. Heinzel, and A. Jain, J. Power Sources, 252, 298 (2014).

40. M. Parhizi, M. Ahmed, and A. Jain, J. Power Sources, 370, 27 (2017).

41. M. F. Couturier, K. George, and M. H. Schneider, Wood Sci. Technol., 30, 179 (1996).

42. J. R. Howell, M. P. Mengüç, K. Daun, and R. Siegel, Thermal Radiation Heat Transfer (CRC press, Boca Raton, FL) (2020).

43. T. Walker, S. C. Xue, and G. W. Barton, J. Heat Transfer, 132, 1 (2010).

CHAPTER 5

Thermal Runaway Propagation in Li-ion Battery Packs Due to Combustion of Vent Gases.

Thermal runaway in Li-ion cells is a well-known and widely researched phenomenon that directly impacts the safety, reliability and performance of electrochemical energy storage and conversion devices[1,2]. The onset of thermal runaway occurs when overheating of the cell results in initiation of exothermic reactions, leading to even greater heat generation. Due to the non-linear Arrhenius nature of heat generation, this results in a positive feedback loop, which, if not prevented, results in destruction of the cell and subsequent fire. Such exothermic reactions underlying thermal runaway include decomposition of the solid-electrolyte-interphase (SEI) layer, electrode-electrolyte reaction and electrolyte decomposition[3]. Semi-global Arrhenius parameters for these processes for various cell chemistries have been acquired through thermal calorimetry experiments and have been widely used in theoretical and simulation studies[3,4]. Thermal runaway is triggered by the competition between chemical heat release and heat loss, and is, in principle, similar to any thermal ignition process. After thermal runaway is triggered, rupture of the cell body often occurs, resulting in venting of hot gases and particles[5]. These venting substances are often hydrocarbon-dominant, and therefore, can trigger combustion and fire with suitable mixture composition and temperature, thus potentially contributing towards thermal runaway propagation.

Propagation of thermal runaway from one cell to another is a very important problem from a system-level safety perspective. While thermal runaway limited to a single cell is undesirable but potentially manageable, on the other hand, propagation to neighboring cells, then further to their neighbors and so on results in destruction of the entire battery pack and a widespread fire at a much larger scale. Therefore, understanding the nature of thermal runaway propagation and the parameters that affect this process is of paramount importance. Accordingly, a number of experimental and computational studies in this direction have been reported.[6] Thermal runaway characteristics for $LiFePO_4$, $Li(Ni_{0.45}Mn_{0.45}Co_{0.10})O_2$ and combination of $LiCoO_2$ and $Li(Ni_{0.5}Mn_{0.25}Co_{0.25})O_2$ chemistries has been studied[7]. For $Li(Ni_xCo_yMn_z)O_2$ type cathode cell, redox reaction between cathode and carbon based anode at high temperatures was identified as the major heat source[8]. The influence of ageing on thermal runaway mechanism has been investigated[9]. Several studies have investigated mitigation of cascade failure following thermal runaway onset in one of the cells in a battery pack. Thermal runaway propagation in a battery pack for different module configurations has been studied using heat-to-vent setting for a single cell[10]. The impact of heating power and heating area on thermal runaway onset has been studied[11]. While experiments provide useful insights into realistic scenarios, simulations-based investigations are equally important due to the cost and complexity of measurements. Analytical [12–14] and numerical models[15,16] to predict thermal runaway have been studied, with the goal to delay or prevent thermal runaway propagation. The importance of thermal properties of the interstitial material between cells in a battery pack has been recognized, and it has been shown that an intermediate thermal conductivity results in an optimum balance between the risks of thermal runaway initiation and thermal runaway propagation[17]. The importance of radiative heat transfer has been recognized[18] and the use of radiative shields for heat removal and thermal runaway prevention has been investigated[19].

The flow of vent gases following rupture of a failed cell is an important event in thermal runaway, as high-speed flow of extremely hot vent gases may spread heat to neighboring cells even in presence of thermal insulation between cells. Moreover, combustion of the volatile vent gases may further contribute towards thermal runaway propagation. Experimentally validated lumped models for single cell have been used to characterize thermal runaway onset during venting in a single cell[20,21]. A mathematical model for predicting temperature-pressure dependence and gas generation within 18650 cell has been developed[5]. The impact of vent gas flow on thermal runaway propagation in battery pack has been studied through simulations[22].

Kinetic mechanisms, gas generation and venting, and subsequent fire and thermal runaway propagation have been studied extensively. Heat of combustion has been measured as a function of SOC using fire propagation apparatus for commercial pouch cells[23]. Dependence of heat release rate and toxic gas emissions on SOC has also been reported using short circuit, propane fire test and external heating test[24]. Investigations on fire induced toxicity for Li-ion cells using Tewarson calorimeter have highlighted the role of anion salt in dictating toxicity[25,26]. Mitigation techniques for Li-ion battery fire suppression using water mist with CO_2 and HFC-227EA[27], and water and $C_6F_{12}O$[28] have been studied. Effect of arrangement of cells in the pack on fire behavior for $LiCoO_2$ 18650 cells has been studied using heat flux, mass flowrate and heat release rate measurements[29]. Experimentally validated analytical models[30] for 21700 NMC cells and 3D heat simulation model[31] for 18650 cells for battery fire characterization have been presented.

Despite the literature cited above, several challenges in the modeling of combustion during thermal runaway remain. For example, thermal runaway kinetic mechanisms frequently involve semi-global reactions, for which, there is a lack of understanding and quantification of elementary reaction pathways. Further, while experimental measurements of vent gas generation have been reported, such measurements are frequently global instead of local, and integrated instead of *in-situ*. Finally, without reliable venting gas models, the modeling of subsequent venting fire and thermal runaway propagation is frequently decoupled with venting gas generation, and the important interaction between venting fire and venting gas generation is not effectively modeled. In general, numerical simulation of thermal runaway in a battery pack is computationally challenging due to the non-linear nature of several processes involved in thermal runaway. Around the time of thermal runaway initiation, heat generation rate increases very rapidly with temperature, and, therefore, an extremely small timestep is needed to properly resolve the problem. In addition, radiative heat transfer is also a non-linear transport process. Such challenges are exacerbated with the inclusion of venting gas combustion, which not only provides non-linear thermal feedback to the upstream thermal runaway initiation, but also affects flow and heat transfer downstream leading to thermal runaway propagation. Despite such challenges, development of robust numerical simulation tools continues to be very important, because such simulations can help design thermal runaway experiments, and contribute towards optimized battery packs for reduced risk of thermal runaway propagation.

This work presents numerical simulation of the onset and propagation of thermal runaway in a Li-ion battery pack, with specific emphasis on investigation of the effects of combustion of vent gases. All three modes of heat transfer – conduction, convection and radiation – are accounted for. Arrhenius heat generation due to four decomposition reactions is modeled. The non-premixed combustion of venting gas is modeled using the standard k-ε model for turbulence and finite rate detailed chemical kinetics. Following validation of the numerical simulation framework by comparison with a benchmark experimental data, the simulation is used for understanding the impact of the combustion process on propagation of thermal runaway from the trigger cell to its neighbors.

The next section presents describes the simulation setup, including the governing physics modeled in the simulations, geometry of the battery pack and computational details. Key results, including validation and parametric analysis are presented in the subsequent section, followed by concluding remarks.

5.1 Simulation set up

5.1.1 Geometry

The geometry considered here comprises a 5 by 5 matrix of cylindrical 18650 cells in a cuboidal box, as shown schematically in Figure 1(a). By taking advantage of symmetry, only the unshaded right half of the geometry shown in Figure 1(a) is simulated. The bottom left cell is taken to be the trigger cell that undergoes thermal runaway first. High speed flow and combustion of hot vent gases emerging from a vent hole on the trigger cell is of particular interest in the present work. Key geometrical parameters here include cell-to-cell gap, overhead gap and position of vent on the trigger cell, as shown in the ZX plane cross-section in Figure 1(b). The area of the circular vent is taken to be 7 mm^2. In order to investigate the effects of various geometrical and other parameters, two distinct positions of the vent hole are considered. The first one is at the center of the top surface of the trigger cell, which may represent opening of the pressure vent or outright failure of the top cap of the cell. The second is located at 62.5 mm height on the curved surface of the cell pointing towards cell 2, which may represent failure of the cell body due to pressure accumulation within the cell during thermal runaway. The entire battery pack is placed inside a cuboidal box. Due to complexity of simulation and extensive computational requirements, venting is only considered from the trigger cell. Also, these simulations model a battery storage scenario, and therefore, charging/discharging of cells is neglected.

Finite-volume heat transfer and fluid flow simulations are carried out in ANSYS Fluent to account for heat generation due to combustion of hot ejecta flowing out at high velocity from the trigger cell. Radiative heat transfer between cells is modeled using surface-to-surface radiation method. Thermal runaway propagation due to thermal abuse and temperature-dependent heat generation in each cell is modeled using Arrhenius chemistry. The next sub-section describes the governing equations for each of these phenomena that are solved to investigate the propagation of thermal runaway in these conditions.

5.2 Governing equations

5.2.1 Non premixed combustion transport equations

Non-premixed combustion model relates the instantaneous thermochemical state of a species to mixture fraction, which is modeled as a conserved scalar quantity[32]. This combustion modeling approach, therefore, involves solving the mixture fraction transport equations, and not the individual species equations. The mixture fraction is defined as:

$$\mathrm{f} = \frac{\mathrm{Z_i} - \mathrm{Z_{i,ox}}}{\mathrm{Z_{i,fuel}} - \mathrm{Z_{i,ox}}} \tag{1}$$

Where $\mathrm{Z_i}$ is the mass fraction for element *i*. Subscripts *ox* and *fuel* represent the oxidizer and fuel, respectively. Due to very high vent speed, flow is assumed to be turbulent, based on which, the assumption of equal diffusivities for individual species is reasonable, since turbulent convection generally overwhelms molecular diffusion. Following this assumption, transport equation for the density averaged mixture fraction f' may be written as

$$\frac{\partial[\rho \mathrm{f}']}{\partial \mathrm{t}} + \nabla \cdot [\rho \mathrm{u} \mathrm{f}'] = \nabla \cdot \left[\left[\frac{k}{C_p} + \frac{v_t}{\mathrm{Pr}}\right] \nabla \mathrm{f}'\right] + S_m \tag{2}$$

where k, C_p, and Pr are mixture thermal conductivity, specific heat and Prandtl number, respectively. $\mathrm{S_m}$ is the rate of transfer of mass from the fuel to the gas phase.

In addition, the conservation equation for mass fraction variance is given by

$$\frac{\partial[\rho f''^2]}{\partial \mathrm{t}} + \nabla \cdot [\rho \mathrm{u} \mathrm{f}''^2] = \nabla \cdot \left[\left[\frac{k}{C_p} + \frac{v_t}{\mu_t}\right] \nabla \mathrm{f}''^2\right] + C_g v_t [\nabla \mathrm{f}']^2 - C_d \rho \frac{\mathcal{E}}{k} f''^2 \tag{3}$$

f''^2 is the mixture fraction variance, with f''=f - f'. Values for constants C_g, C_d are 2.86 and 2.0 respectively. Thermal diffusivity for the turbulent flow is considered equal to the mass diffusivity.

Mass fraction, density and temperature are assumed to be functions of the mixture fraction. In this case, heat gain/loss is parameterized as follows

$$\Phi_\mathrm{i} = \Phi_i(\mathrm{f}', \mathrm{H}) \tag{4}$$

where Φ_i represents mass fraction, density or temperature and H represents the instantaneous enthalpy. Mean scalars for each species are calculated as:

$$\Phi_i' = \int_0^1 \Phi_i(\mathrm{f}', \mathrm{H})\mathrm{p}(\mathrm{f}')\mathrm{df}' \tag{5}$$

where $\mathrm{p}(\mathrm{f}')$ is a probability density function. Finally, energy equation for the non-premixed combustion model is written in the mean enthalpy form as follows:

$$\frac{\partial[\rho\mathrm{H}]}{\partial\mathrm{t}} + \nabla\cdot[\rho\mathrm{uH}] = \nabla\cdot\left[\frac{k_{eff}}{C_p}\,\nabla\mathrm{H}\right] + S_h \tag{6}$$

Here, species diffusion and conduction collectively contribute towards the first term on the right-hand side. Equation (4) is written in terms of the total enthalpy H. Total enthalpy of individual species is defined as:

$$\mathrm{H_i} = \int_{\mathrm{T_{ref,i}}}^{\mathrm{T}} \mathrm{C_{p,i}dT} + \mathrm{h_i^0}[\mathrm{T_{ref,i}}] \tag{7}$$

Where, $\mathrm{h_i^0}[\mathrm{T_{ref,i}}]$ is the enthalpy of formation of species *i* and $\mathrm{T_{ref,i}}$ is the reference temperature. Combustion model is described by finite rate chemistry, where a reduced C_2H_4 combustion model including 32 species and 206 elementary reactions is adopted to simulate the venting flame. This model has been extensively validated against C0-C2 combustion targets[33].

5.2.2 Thermal conduction

High speed flow of ejecta combined with combustion presents stability challenges in numerical computation. As a result, the $k - \varepsilon$ model is used[34], which offers high numerical stability without the need for damping functions. This turbulent flow model comprises two equations, which solve for turbulent kinetic energy and specific dissipation rate. This model also accounts for the effects of stream turbulence and mass injection. The mass conservation equation is written as:

$$\nabla \cdot (\rho \mathbf{V}) = 0 \tag{8}$$

The transport equations for turbulent kinetic energy (E_t) and specific dissipation rate (ε) are given by:

$$\frac{\partial(\rho E_t)}{\partial \mathrm{t}} + \nabla \cdot (\rho E_t u) = \nabla \cdot [\left(\mu + \frac{\mu_t}{Pr_k}\right) \nabla E_t] + \mathrm{G_k} + \mathrm{G}_b - \mathrm{Y_m} + \mathrm{S_k} - \rho\varepsilon \tag{9}$$

$$\frac{\partial(\rho\varepsilon)}{\partial \mathrm{t}} + \nabla \cdot (\rho\varepsilon u) = \nabla \cdot \left[\left(\mu + \frac{\mu_t}{Pr_\varepsilon}\right) \nabla\varepsilon\right] + C_{1\varepsilon} \frac{\varepsilon}{E_t} \left[G_k + C_{3\varepsilon} G_b\right] - C_{2\varepsilon} \frac{\rho\varepsilon^2}{E_t} + S_\varepsilon \tag{10}$$

Here, G_k represents the generation of turbulence kinetic energy due to mean velocity gradients, G_b is the generation turbulent kinetic energy due to buoyancy and Y_m represents fluctuating dilatation in compressible turbulence to overall dissipation rate. Pr_k and Pr_ε represent turbulent Prandtl numbers for kinetic energy and dissipation rate, respectively. $\mathrm{S_k}$ and S_ε denote user defined source terms. $C_{1\varepsilon}$, $C_{2\varepsilon}, Pr_k$ and Pr_ε are constants with experimentally determined values of 1.44, 1.92, 1.0 and 1.3 respectively.

Similarly, turbulent heat transport equation for the turbulent flow can be written as

$$\frac{\partial(\rho \mathrm{E})}{\partial \mathrm{t}} + \nabla \cdot \left[u\left(\rho \mathrm{E} + \mathrm{p}\right)\right] = \nabla \cdot \left[\left(\mathrm{k} + \frac{\mathrm{C_p}\mu}{Pr}\right)\nabla \mathrm{T} + u \cdot \bar{\bar{\tau}}\right] + \mathrm{S_{hs}} \tag{11}$$

where k is the effective thermal conductivity, E is total energy, S_{hs} is the heat source term and $\bar{\bar{\tau}}$ is a deviatoric stress tensor.

5.2.3 Heat generation

Heat transfer within each solid cell is governed by the three-dimensional thermal conduction equation in cylindrical coordinates, given by

$$\frac{\mathrm{k_r}}{\mathrm{r}}\frac{\partial}{\partial \mathrm{r}}\left(\mathrm{r}\frac{\partial \mathrm{T}}{\partial \mathrm{r}}\right) + \frac{\mathrm{k_\theta}}{\mathrm{r}^2}\frac{\partial^2 \mathrm{T}}{\partial \theta^2} + \mathrm{k_z}\frac{\partial^2 \mathrm{T}}{\partial \mathrm{z}^2} + \mathrm{q}''' = \rho \mathrm{c_p}\frac{\partial \mathrm{T}}{\partial \mathrm{t}} \tag{12}$$

where thermal conductivity within the cell is taken to be homogeneous and cylindrically orthotropic. All properties are assumed to be independent of temperature. In equation (12), $\mathbf{q}'''$ represents volumetric heat generation within the cell due to decomposition reactions, as discussed in more detail next. Values of thermal properties appearing in equation (12) are taken from past work[35].

5.2.4 Radiative heat transfer

Heat is generated within each cell due to decomposition reactions, including SEI decomposition, negative solvent reaction, positive solvent reaction and electrolyte decomposition reactions respectively. Arrhenius-based reaction parameters for these standard set of equations corresponding to $LiCoO_2$ cell chemistry are used. The governing equations and values of reaction parameters are readily available in past work[22].

5.2.5 Radiation heat transfer

Radiative heat transfer between surfaces of cells is explicitly modeled based on surface-to-surface radiative heat exchange. View factors are calculated using the ray tracing method. Details of the radiation model, including validation are described in a past paper[16].

5.2.6 Isentropic flow equations

Temperature and velocity distribution of the hot ejecta from the vent hole are determined as functions of time using isentropic flow equations. These equations are based on mass flow rate and stagnation pressure measurements from previous experimental work[36]. Thermophysical properties of the ejecta are calculated using weighted average using an open source software[37]. The individual gaseous species (CO_2, H_2, C_2H_4, CO, CH_4, C_2H_6) correspond to LCO type cathode 18650 cells[38]. The ejecta originating from trigger cell is assumed to contain 17.5% H_2, 33.8% CO_2, 39.9% CO, 5.2% CH_4, 3.2% C_2H_4 and 0.4% C_2H_6 by mole respectively. The hot ejecta leaving the trigger cell is treated to be a calorically perfect gas. The equations derived based on stagnation flow analysis establish direct relationship between stagnation pressure and Mach number, and an inverse relationship between venting temperature and stagnation pressure. The inverse relationship between temperature and velocity of the ejecta signifies the conversion of pressure energy into intermolecular energy. More details on isentropic flow calculations are available in a past paper[22].

5.2.7 Meshing and other simulation details

Appropriate discretization of the simulation domain is critical for obtaining good convergence, particularly in the present case that combines multiple non-linear processes. All simulations in this work use 3D polyhedral mesh due to low numerical diffusivity and semi-automatic generation. These characteristics not only result in better approximation of gradients across the elements, but also offer better mesh resolution in complex geometries. Polyhedral elements are less sensitive to stretching, which results in improved numerical stability and more accurate solution with lower cell count as compared to other types of meshing elements. In these simulations, upwards of 10.1 million elements are used with a growth rate of 1.05, squish index of 0.38 and orthogonal quality of 0.67. Temperature and pressure boundary conditions for the vent are obtained using isentropic flow analysis, as described in previous work[22]. While the vent temperature increases monotonically with time, vent velocity rises, reaches a peak, and then reduces as the cell runs out of vent gas to eject. Natural convective cooling boundary condition is used for all surfaces of the battery pack except the diagonal symmetry plane shown in Figure 1(a), which is modeled as adiabatic surface.

Combustion and supersonic flow of ejecta around cells results in tremendous heat release in a very short span of time. These peculiar characteristics escalate the non-convergent behavior of energy equation, requiring very small time steps, especially close to thermal runaway. This is addressed by using a 10 μs constant time stepping with 10^{-4} relative tolerance. As described in the next section, a comprehensive time step sensitivity analysis is performed, and time step is determined based on the tradeoff between numerical accuracy and efficiency.

5.3 Results and discussion

Appropriate discretization of the simulation domain is critical for obtaining good convergence, particularly in the present case that combines multiple non-linear processes. All simulations in this work use 3D polyhedral mesh due to low numerical diffusivity and semi-automatic generation. These characteristics not only result in better approximation of gradients across the elements, but also offer better mesh resolution in complex geometries. Polyhedral elements are less sensitive to stretching, which results in improved numerical stability and more accurate solution with lower cell count as compared to other types of meshing elements. In these simulations, upwards of 10.1 million elements are used with a growth rate of 1.05, squish index of 0.38 and orthogonal quality of 0.67. Temperature and pressure boundary conditions for the vent are obtained using isentropic flow analysis, as described in previous work[22]. While the vent temperature increases monotonically with time, vent velocity rises, reaches a peak, and then reduces as the cell runs out of vent gas to eject. Natural convective cooling boundary condition is used for all surfaces of the battery pack except the diagonal symmetry plane shown in Figure 1(a), which is modeled as adiabatic surface.

Combustion and supersonic flow of ejecta around cells results in tremendous heat release in a very short span of time. These peculiar characteristics escalate the non-convergent behavior of energy equation, requiring very small-time steps, especially close to thermal runaway. This is addressed by using a 10 µs constant time stepping with 10^{-4} relative tolerance. As described in the next section, a comprehensive time step sensitivity analysis is performed, and time step is determined based on the tradeoff between numerical accuracy and efficiency.

Due to the considerable complexity of the simulation model described in the previous section, including multiple coupled and non-linear phenomena, it is important to carry out a robust validation of the simulation model. This is done by comparison with classical Raman/Rayleigh/LIF measurements in a benchmark turbulent $CH_4/H_2/N_2$ jet diffusion flame[39]. These measurements have been reported for combustion of a fuel exiting from an 8 mm diameter nozzle. The fuel used for combustion consists of 22.1% methane, 33.2% hydrogen and 44.7% nitrogen by mole. The average flow velocity of the fuel is 42.2 m/s and the Reynolds number is *Re*=15200. The stoichiometric mixture fraction is 0.167 and the flame adiabatic temperature is 2130 K. Under these conditions, measurements of temperature and mass fraction of combustion products reported in the past are used for validation of the simulation model.

The simulation model is computed for the same set of conditions as the experiments. Comparison between the two is carried out in terms of radial distribution of temperature, as shown in Figure 3, and of H_2O and CO_2 concentrations, as shown in Figures 4(a) and 4(b), respectively, at a 40 mm distance from the nozzle tip. These plots show very good agreement between simulations and experimental data[39] for both temperature and species concentration. The thermal and chemical structures of the non-premixed flame reflect the dominant physical-chemical processes of chemical kinetics, molecular and turbulent diffusion. This validation exercise provides good confidence in the combustion modeling utilized in this work.

In order to further investigate the combustion phenomenon and to ensure that the simulation correctly captures the combustion process, distributions of key combustion products as well as the temperature distribution are examined as functions of time. Figures 5(a) and 5(b) present contours of the concentration distribution of H_2O and OH radicals, respectively, on the XY plane above the top end of cells at multiple times Figure 6 presents similar temperature profiles. H_2O is a major product of the combustion process, and the OH radical is a good indicator of the reaction front location. At early times, say, t = 0.001s, the peak of H_2O and OH in Figure 5 and the temperature profile in Figure 6 all indicate a regular flame structure with a thin reaction zone. Due to the very large vent velocity, venting gas, fresh air entrainment and hot combustion products quickly mix with each other and form a partially premixed reacting mixture. As time passes, the reaction region becomes much thicker and starts propagating into the rest of the domain, as seen in the plots at t =

0.01 s, when the venting flame has spread to nearly 2/3rds of the domain along the X direction. Within 0.1 s, the high temperature region has already occupied near half of the XY plane, leading to exposure to high temperature (greater than 1000 K) for the rest of cells.

In order to characterize the impact of combustion on the propagation of thermal runaway, two sets of simulations are carried out for a nominal set of conditions. The vent gas is assumed to eject from a 7 mm^2 hole at the center of top surface of the trigger cell. The vent duration is 2 s, and the overhead and cell-to-cell gap are 5 mm and 4 mm, respectively. In the first case, combustion of the venting gases is modeled, whereas, in the second case, the gases are assumed to vent out of the cell but not undergo combustion. For these two cases, Figures 7 and 8 plot maximum temperatures in various cells in the battery pack as functions of time. It is seen clearly from Figure 8 that when only venting is modeled, several cells, such as cells 2, 3 and 4 attain high temperature, but the thermal runaway is not sustained in any neighboring cell. At the end of the venting event, i.e., t=2 s, all cells start to cool down. Eventually, there is no propagation of thermal runaway from the trigger cell into any other cells. On the other hand, as shown in Figure 7, when the combustion of the venting gases is correctly modeled, the additional heat generated due to combustion is sufficient to cause thermal runaway to propagate into cell 2, as characterized by sustained high temperature on cell 2.

These results clearly indicate the importance of the combustion process during thermal runaway propagation and, therefore, the need to include combustion calculations in simulation models. A simulation model without combustion incorrectly predicts no thermal runaway propagation, whereas, when combustion is modeled, it is found that thermal runaway propagation indeed occurs.

It is of much interest to understand how the location of the vent hole influences the propagation of thermal runaway. In general, vent gases may eject out of a hole on the top surface of the cell when the pressure in the cell rises too much and the relief valve located on the top cap opens to release the vent gases. On the other hand, excessive pressure is the cell may also cause rupture in the cell body, which may cause rupture and ejection from the weakest point, which may be located anywhere on the cell body[40]. Given the uncertainty of the location of failure, it is of interest to understand how differently the thermal runaway propagation process may occur in these cases. Two particular cases are considered here – in the first case, a 7 mm^2 vent hole is located at the center of the top surface of the trigger cell. In the second case, a vent hole of the same size is located on the curved surface of the trigger cell, 2.5 mm below top end and directly facing cell 2. All other problem parameters in the two cases are the same as each other, corresponding to the parameters used in Figure 2. Figures 9(a) and 9(b) plot temperature curves for various cells for the two cases respectively. These plots clearly show that when the vent hole is located on the top surface of the cell, thermal runaway propagation occurs only to cell 2, while other cells do not undergo thermal runaway despite getting hotter. This may be attributed to the upwards pointing vent hole, due to which, vent gases exit upwards, and the combustion process occurs above the trigger cell, thereby having a limited impact on other cells. On the other hand, when the vent hole is located on the curved surface facing cell 2, combustion occurs in the thin space between the cells, which particularly impacts cells 2 and 7 the two cells that are closest to the trigger cell. As Figure 9(b) shows, thermal runaway propagates to both cells 2 and 7 in this case. This clearly highlights the distinction in thermal runaway propagation depending on the location and direction of the venting event. For further illustration and comparison, temperature contour plots for the two cases is presented at different times in Figure 10. These plots show spreading of thermal runaway to only cell 2 when the vent hole is located at the top of the trigger cell, and to both cells 2 and 7 when the vent hole is located on the side wall. Note that in this work, secondary thermal runaway propagation is not accounted for. Once the neighboring cells enter thermal runaway and combustion of gases venting from neighboring cells occurs, it is quite likely, based on the results from this work further outwards propagation of thermal runaway will occur.

List of Figures

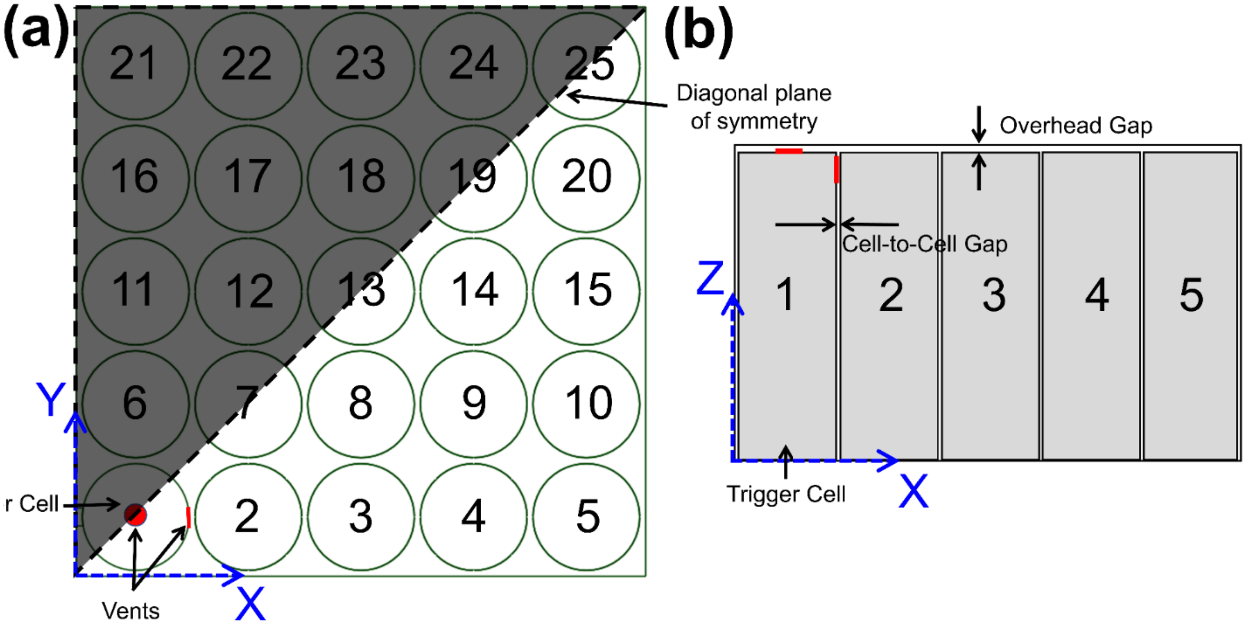

Figure 1. (a) Schematic of the simulation geometry for a 5 by 5 Li-ion battery pack. The half-geometry modeled in this work based on symmetry is indicated; (b) Cross-section view of the geometry in the XZ plane. Cell1 is the trigger cell, with the vent hole located either at the top end or on the curved surface, as shown.

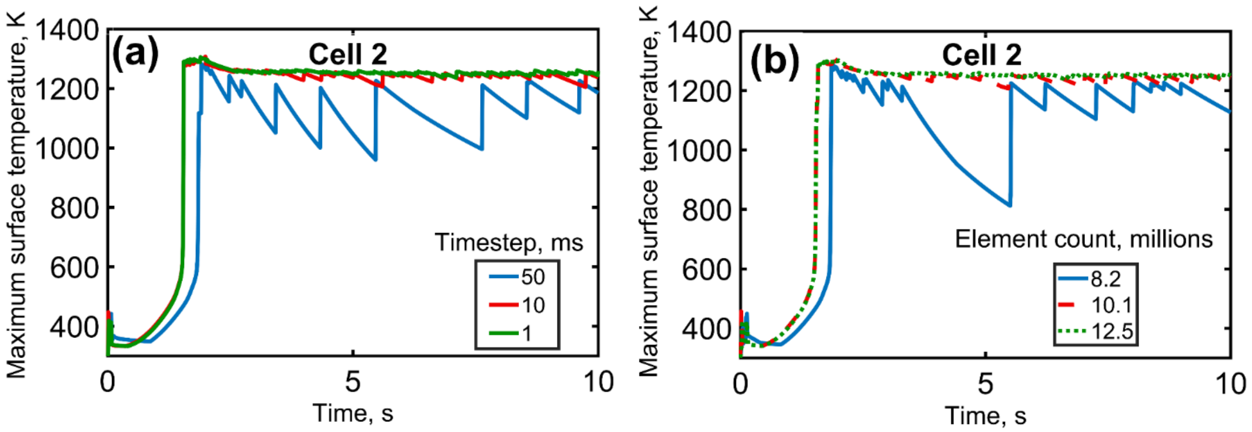

Figure 2. Simulation results to establish time step sensitivity and grid independence: Maximum surface temperature on cell 2 as a function of time for (a) different time steps, and (b) different mesh sizes. Problem parameters include 1 mm overhead gap, 4 mm cell-to-cell gap, 2 s venting time , LCO cathode and 7 mm^2 vent placed at center of top surface of Cell 1. In (a), the element count is 12.5 million, and in (b), the timestep is 1 μs.

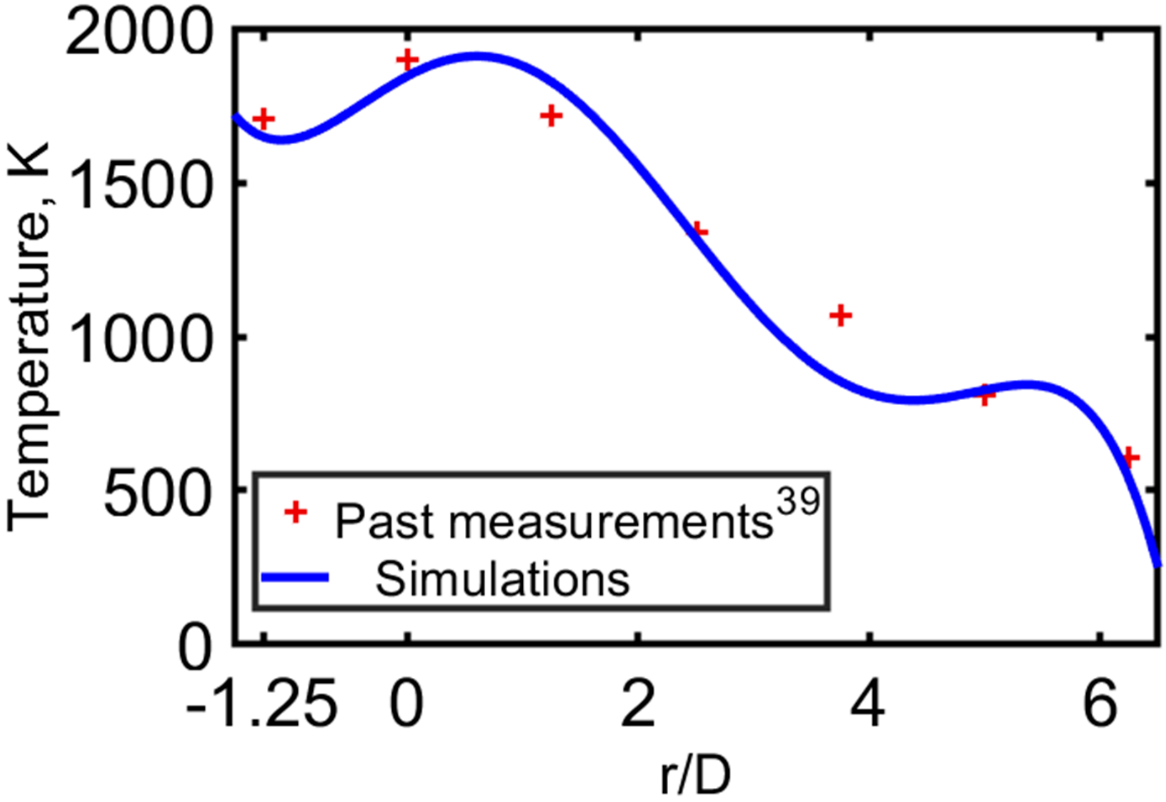

Figure 3. Validation plots for the combustion model: Radial variation in temperature at 40 mm distance from nozzle for Raman/Rayleigh combustion process. Numerical simulation results are compared with past experimental data[39]. Fuel molar composition is 22.1% CH_4, 33.2% H_2, 44.7% N_2. Other simulation parameters include 42.2 ms^{-1} jet velocity, Reynolds number of 15200 and 8 mm nozzle diameter.

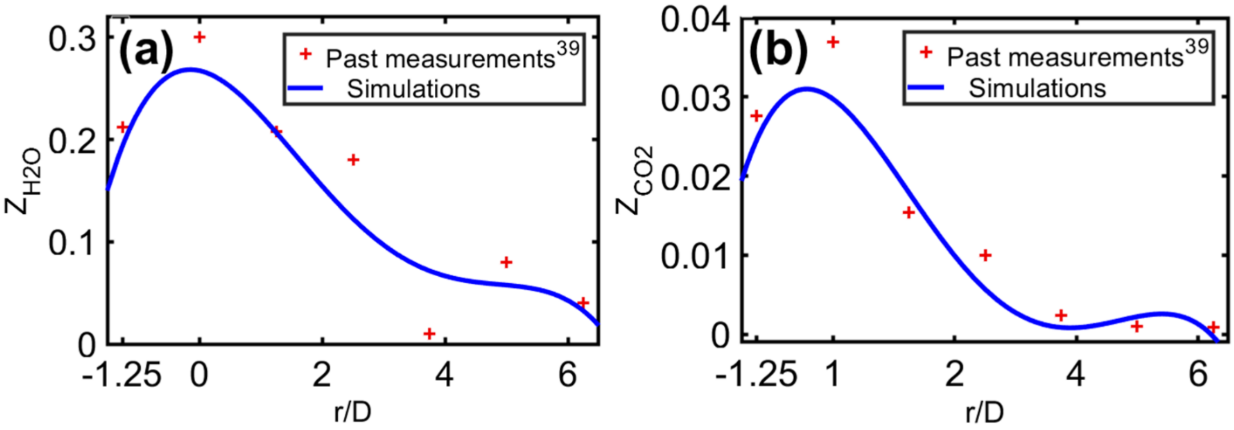

Figure 4. Validation plots for the combustion model: Radial variation in mass fraction for (a) water and (b) carbon dioxide at 40 mm distance from nozzle for Raman/Rayleigh combustion process. Numerical simulation results are compared with past experimental data[39]. Fuel molar composition is 22.1% CH_4, 33.2% H_2, 44.7% N_2 composition. Other simulation parameters include 42.2 ms^{-1} jet velocity, Reynolds number of 15200 and 8 mm nozzle diameter.

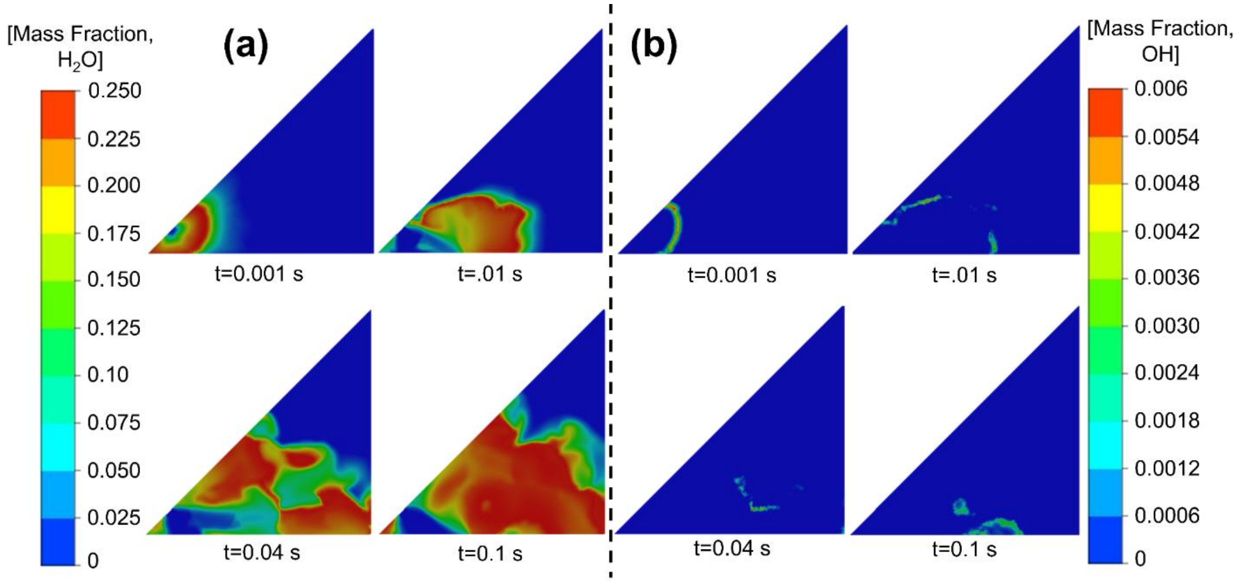

Figure 5. Color plots showing (a) H_2O and (b) OH radical concentrations at multiple times on an XY cross-section plane 1 mm above the top end of cells. Problem parameters correspond to Figure 2.

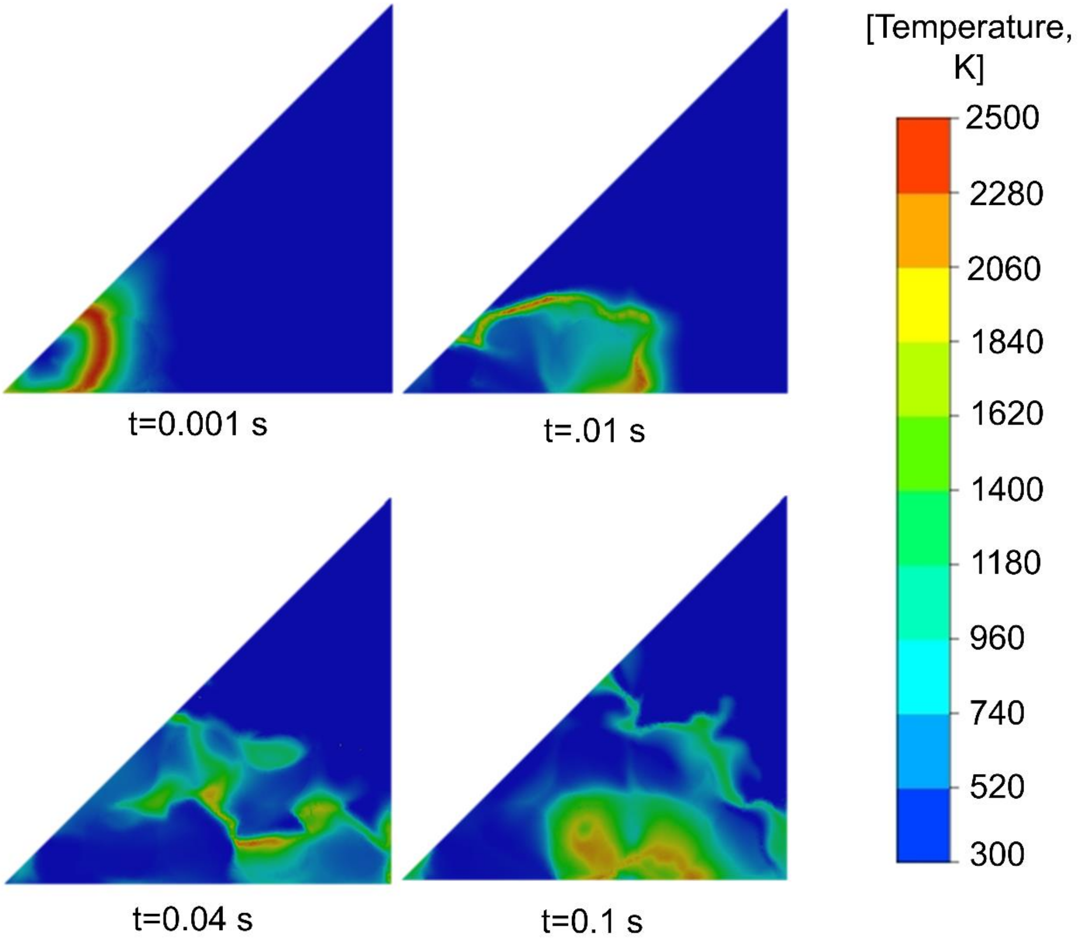

Figure 6.

Figure 6. Color plots showing temperature distribution at multiple times on an XY cross-section plane 1 mm above the top end of cells. Problem parameters correspond to Figure 4.

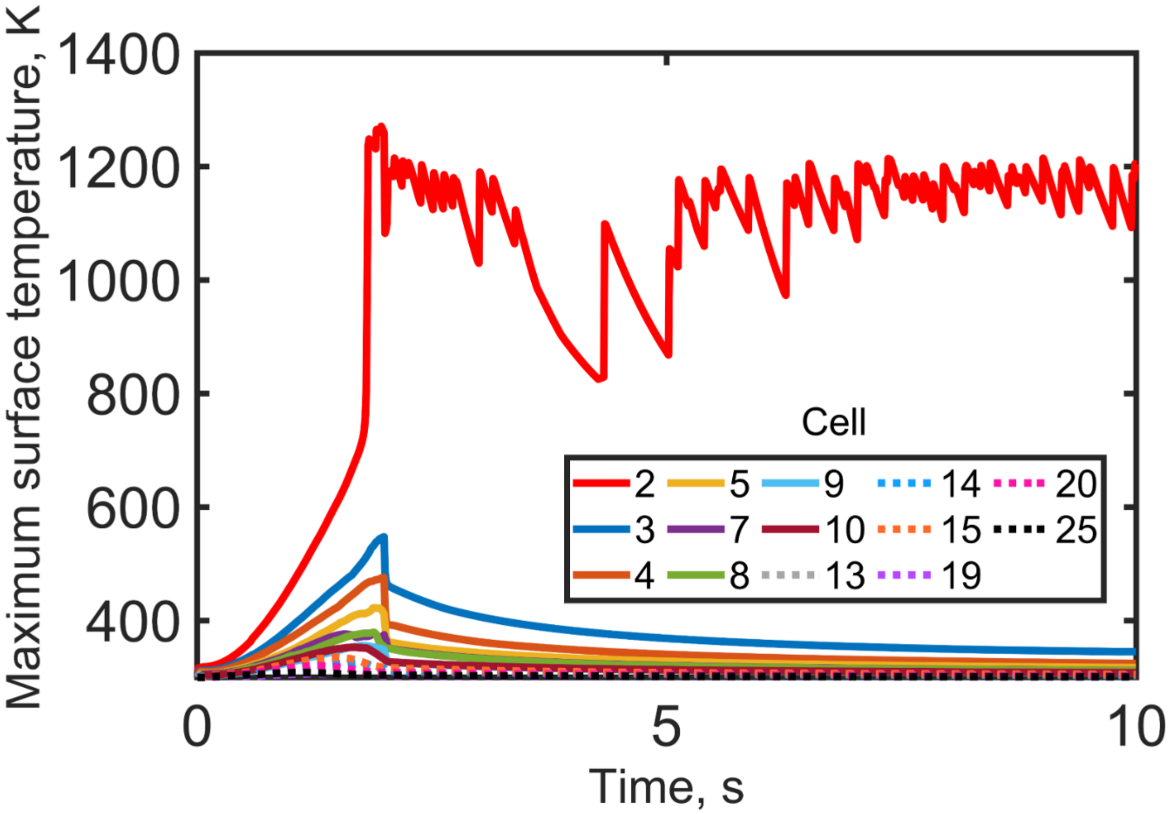

Figure 7: Temperature field when venting and combustion are both modeled: Temperature plots for the case of 2 s venting from a 7 mm^2 vent placed at center of top surface of cell 1. Overhead gap and cell-cell gap are 5 mm and 4 mm, respectively.

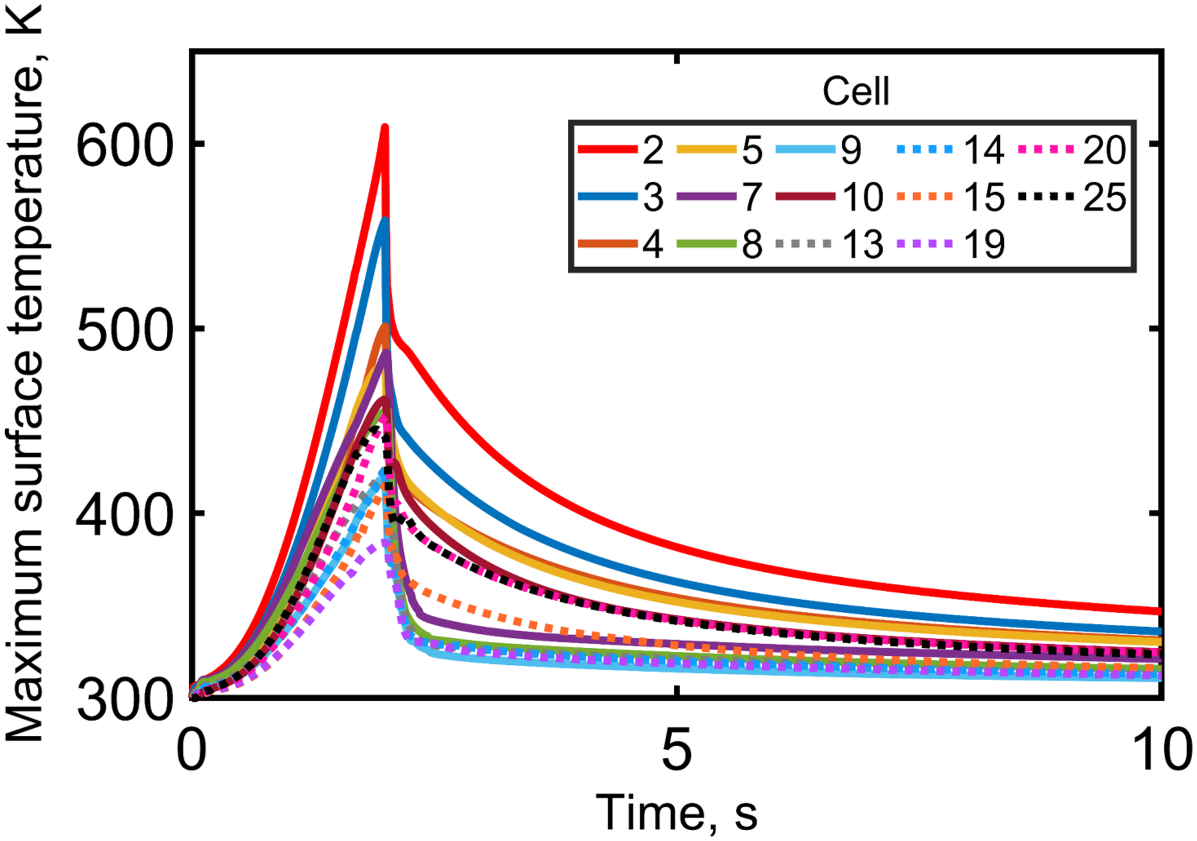

Figure 8: Temperature field when venting is modeled without combustion: Temperature plots for the case of 2 s venting from a 7 mm^2 vent placed at center of top surface of cell 1. Overhead gap and cell-cell gap are 5 mm and 4 mm, respectively.

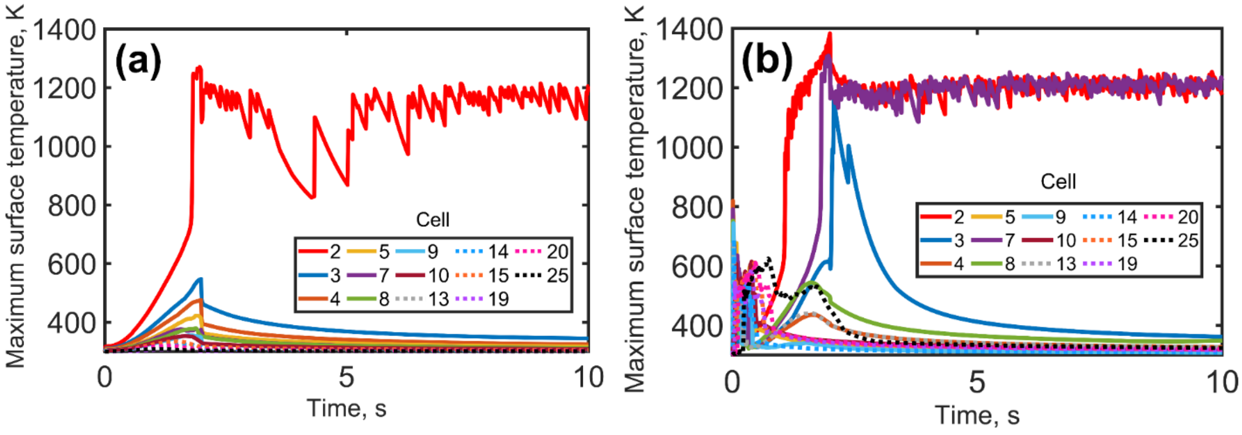

Figure 9: Effect of location of vent: Temperature plots for 1 mm overhead and cell-to-cell gap, 2 s venting time and 7 mm^2 vent placed at (a) center of top surface of trigger cell, and (b) 63.5 mm height on curved surface of trigger cell directly facing cell 2.

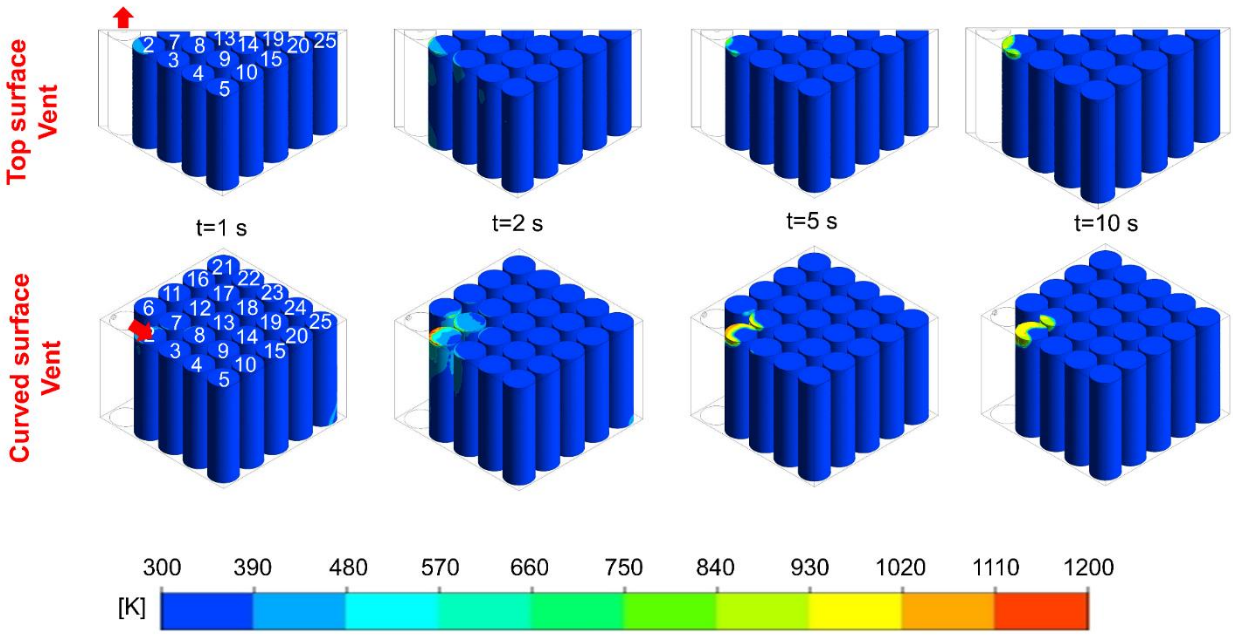

Figure 10: Colorplots at different timesteps for the two vent locations presented in Figure 9.

References:

1. K. Shah, V. Vishwakarma, and A. Jain, “Measurement of multiscale thermal transport phenomena in Li-ion cells: a review.” J Electrochem Energy Convers Storage., 13, 030801 (2016).

2. T. M. Bandhauer, S. Garimella, and T. F. Fuller, “A critical review of thermal issues in Lithium-ion batteries.” J. Electrochem. Soc., 158, R1 (2011).

3. R. Spotnitz and J. Franklin, “Abuse behavior of high-power, lithium-ion cells.” J. Power Sources, 113, 81 (2003).

4. A. Melcher, C. Ziebert, M. Rohde, and H. J. Seifert, “Modeling and simulation of the thermal runaway behavior of cylindrical Li-ion cells-computing of critical parameters.” Energies., 9, 1 (2016).

5. P. T. Coman, S. Mátéfi-Tempfli, C. T. Veje, and R. E. White, “Modeling vaporization, gas generation and venting in Li-ion battery cells with a dimethyl carbonate electrolyte.” J. Electrochem. Soc., 164, A1858 (2017).

6. P. Jindal and J. Bhattacharya, “Review—understanding the thermal runaway behavior of Li-ion batteries through experimental techniques.” J. Electrochem. Soc., 166, A2165 (2019).

7. A. W. Golubkov, D. Fuchs, J. Wagner, H. Wiltsche, C. Stangl, G. Fauler, G. Voitic, A. Thler, and V. Hacker, “Thermal-runaway experiments on consumer Li-ion batteries with metal-oxide and olivin-type cathodes.” RSC Adv., 4, 3633 (2014).

8. X. Feng et al., “Investigating the thermal runaway mechanisms of lithium-ion batteries based on thermal analysis database.” Appl. Energy, 246, 53 (2019).

9. S. Abada, M. Petit, A. Lecocq, G. Marlair, V. Sauvant-Moynot, and F. Huet, “Combined experimental and modeling approaches of the thermal runaway of fresh and aged lithium-ion batteries.” J. Power Sources, 399, 264 (2018).

10. A. O. Said, C. Lee, S. I. Stoliarov, and A. W. Marshall, “Comprehensive analysis of dynamics and hazards associated with cascading failure in 18650 lithium ion cell arrays.” Appl. Energy, 248, 415 (2019).

11. C. F. Lopez, J. A. Jeevarajan, and P. P. Mukherjee, “Evaluation of combined active and passive thermal management strategies for lithium-ion batteries.” J Electrochem Energy Convers Storage., 13, 031007 (2016).

12. C. Jin et al., “Model and experiments to investigate thermal runaway characterization of lithium-ion batteries induced by external heating method.” J. Power Sources, 504, 230065 (2021).

13. Z. Huang, C. Zhao, H. Li, W. Peng, Z. Zhang, and Q. Wang, “Experimental study on thermal runaway and its propagation in the large format Lithium ion battery module with two electrical connection modes.” Energy, 205, 117906 (2020).

14. Z. Huang, X. Li, Q. Wang, Q. Duan, Y. Li, L. Li, and Q. Wang, “Experimental investigation on thermal runaway propagation of large format lithium ion battery modules with two cathodes.” Int J Heat Mass Transf., 172, 121077 (2021).

15. X. Feng, J. Sun, M. Ouyang, F. Wang, X. He, L. Lu, and H. Peng, “Characterization of penetration induced thermal runaway propagation process within a large format lithium ion battery module.” J. Power Sources, 275, 261 (2015).

16. K. Shah, D. Chalise, and A. Jain, “Experimental and theoretical analysis of a method to predict thermal runaway in Li-ion cells.” J. Power Sources, 330, 167 (2016).

17. D. Ren, X. Liu, X. Feng, L. Lu, M. Ouyang, J. Li, and X. He, “Model-based thermal runaway prediction of lithium-ion batteries from kinetics analysis of cell components.” Appl. Energy, 228, 633 (2018).

18. M. Parhizi, M. B. Ahmed, and A. Jain, “Determination of the core temperature of a Li-ion cell during thermal runaway.” J. Power Sources, 370, 27 (2017).

19. L. Zhang, P. Zhao, M. Xu, and X. Wang, “Computational identification of the safety regime of Li-ion battery thermal runaway.” Appl. Energy, 261, 114440 (2020).

20. X. Feng, L. Lu, M. Ouyang, J. Li, and X. He, “A 3D thermal runaway propagation model for a large format lithium ion battery module.” Energy, 115, 194 (2016).

21. D. Mishra and A. Jain, “Multi-mode heat transfer simulations of the onset and propagation of thermal runaway in a pack of cylindrical li-ion cells.” J. Electrochem. Soc., 168, 20504 (2021).

22. T. D. Hatchard, D. D. MacNeil, D. A. Stevens, L. Christensen, and J. Dahn, “Importance of heat transfer by radiation in Li-ion batteries during thermal abuse.” Electrochem. Solid-State Lett., 3, 305 (2000).

23. D. Mishra, K. Shah, and A. Jain, “Investigation of the impact of radiative shielding by internal partitions walls on propagation of thermal runaway in a matrix of cylindrical li-ion cells.” J. Electrochem. Soc., 168, 120507 (2021).

24. H. Zhai, H. Li, P. Ping, Z. Huang, and Q. Wang, "An experimental-based domino prediction model of thermal runaway propagation in 18,650 lithium-ion battery modules." Int J Heat Mass Transf., 181, 122024 (2021).

25. J. K. Ostanek, W. Li, P. P. Mukherjee, K. R. Crompton, and C. Hacker, "Simulating onset and evolution of thermal runaway in Li-ion cells using a coupled thermal and venting model." Appl. Energy, 268, 114972 (2020).

26. P. T. Coman, S. Rayman, and R. E. White, "A lumped model of venting during thermal runaway in a cylindrical Lithium Cobalt Oxide lithium-ion cell." J. Power Sources, 307, 56 (2016).

27. D. Mishra, K. Shah, and A. Jain, "Investigation of the impact of flow of vented gas on propagation of thermal runaway in a li-ion battery pack." J. Electrochem. Soc., 168, 060555 (2021).

28. D. Kong, G. Wang, P. Ping, and J. Wen, "A coupled conjugate heat transfer and CFD model for the thermal runaway evolution and jet fire of 18650 lithium-ion battery under thermal abuse." eTransportation., 12, 100157 (2022).

29. P. Ribière, S. Grugeon, M. Morcrette, S. Boyanov, S. Laruelle, and G. Marlair, "Investigation on the fire-induced hazards of Li-ion battery cells by fire calorimetry." Energy Environ. Sci., 5, 5271 (2012).

30. F. Larsson, P. Andersson, and B. E. Mellander, "Lithium-ion battery aspects on fires in electrified vehicles on the basis of experimental abuse tests." Batteries., 2, 1 (2016).

31. A. Lecocq, G. G. Eshetu, S. Grugeon, N. Martin, S. Laruelle, and G. Marlair, "Scenario-based prediction of Li-ion batteries fire-induced toxicity." J. Power Sources, 316, 197 (2016).

32. G. G. Eshetu, J. P. Bertrand, A. Lecocq, S. Grugeon, S. Laruelle, M. Armand, and G. MArlair, “Fire behavior of carbonates-based electrolytes used in Li-ion rechargeable batteries with a focus on the role of the LiPF6 and LiFSI salts.” J. Power Sources, 269, 804 (2014).

33. J. Xu, P. Guo, Q. Duan, X. Yu, L. Zhang, Y. Liu, and Q. Wang, “Experimental study of the effectiveness of three kinds of extinguishing agents on suppressing lithium-ion battery fires.” Appl. Therm. Eng., 171, 115076 (2020).

34. Y. Liu, Q. Duan, J. Xu, H. Li, J. Sun, and Q. Wang, “Experimental study on a novel safety strategy of lithium-ion battery integrating fire suppression and rapid cooling.” J Energy Storage., 28, 101185 (2020). 35. M. Chen, R. Yuen, and J. Wang, “An experimental study about the effect of arrangement on the fire behaviors of lithium-ion batteries.” J. Therm. Anal. Calorim., 129, 181 (2017).

36. C. M. R. Vendra, A. V. Shelke, J. E. H. Buston, J. Gill, D. Howard, E. Read, A. Abaza, B. Cooper, and J. X. Wen, “Numerical and experimental characterisation of high energy density 21700 lithium-ion battery fires.” Process Saf. Environ. Prot., 160, 153 (2022).

37. Y. Takagishi, Y. Tozuka, T. Yamanaka, and T. Yamaue, “Heating simulation of a Li-ion battery cylindrical cell and module with consideration of gas ejection.” Energy Reports., 8, 3176 (2022).

38. F. A. Mier, M. J. Hargather, and S. Ferreira, “Experimental quantification of vent mechanism flow parameters in 18650 format lithium ion batteries.” J Fluids Eng Trans ASME., 141, 1 (2019).

39. F. A. Williams, Combustion Theory. (Boca Raton, FL)(CRC Press) (2018).

40. Z. Luo, C. S. Yoo, E. S. Richardson, J. H. Chen, C. K. Law, and T. Lu, “Chemical explosive mode analysis for a turbulent lifted ethylene jet flame in highly-heated coflow.” Combust. Flame, 159, 265 (2012).

41. Z. Yang and T. H. Shih, AIAAJ, 31, 11752 (2012) .

42. S. J. Drake, D. A. Wetz, J. K. Ostanek, S. P. Miller, J. M. Heinzel, and A. Jain, “Measurement of anisotropic thermophysical properties of cylindrical Li-ion cells.” J. Power Sources, 252, 298 (2014).

43. I. H. Bell, S. Quoilin, J. Wronski, and V. Lemort, “Coolprop: an open-source reference-quality thermophysical property library.” ASME ORC 2nd International Seminar on ORC Power Systems. (2013). 44. A. W. Golubkov, S. Scheikl, R. Planteu, G. Voitic, H. Wiltsche, C. Stangl, G. Fauler, A. Thaler, and V. Hacker, “Thermal runaway of commercial 18650 Li-ion batteries with LFP and NCA cathodes - impact of state of charge and overcharge.” RSC Adv., 5, 57171 (2015).

45. W. Meier, R. S. Barlow, Y. L. Chen, and J. Y. Chen, “Raman/Rayleigh/LIF measurements in a turbulent CH4/H2/N2 jet diffusion flame: experimental techniques and turbulence-chemistry interaction.” Combust. Flame, 123, 326 (2000).

46. H. Wang, “Consistent flamelet modeling of differential molecular diffusion for turbulent non-premixed flames.” Phys. Fluids, 28, 035102 (2016).

47. A. K. Chatzopoulos and S. Rigopoulos, “A chemistry tabulation approach via rate controlled constrained equilibrium (RCCE) and artificial neural networks (ANNs), with application to turbulent non-premixed CH4/H2/N2 flames.” Proc. Combust. Inst., 34, 1465 (2013).

48. J. Kim, A. Mallarapu, D. P. Finegan, and S. Santhanagopalan, “Modeling cell venting and gas-phase reactions in 18650 lithium ion batteries during thermal runaway.” J. Power Sources, 489, 229496 (2021).

CHAPTER 6

Investigation of Propagation of Thermal Runaway during Large-Scale Storage and Transportation of Li-ion Batteries.

Li-ion cells are used commonly for electrochemical energy conversion and storage in automobiles,[1] spacecraft,[2] renewable grid energy storage[3] and consumer electronics. Li-ion cells offer excellent energy storage characteristics, including high energy storage density, excellent cyclability, low self-discharge rate and minimal memory effect. However, Li-ion cells are known to be very temperature-sensitive, with rapid deterioration in performance at low or high temperatures.[4] In addition, overheating of a Li-ion cell also presents the risk of thermal runaway, which refers to a series of sustained decomposition reactions that are triggered at a high temperature and usually lead to fire and explosion.[5] These reactions, including decomposition of the electrode materials, binders, separator and the electrolyte have strongly temperature-dependent reaction rates, which sets up positive feedback between temperature rise and heat generation. The prediction[6] and prevention[7,8] of thermal runaway remains a key challenge in Li-ion battery safety.

Due to its critical importance in battery safety, thermal runaway has been heavily studied through both measurements and modeling. The key decomposition reactions that occur during thermal runaway onset have been experimentally characterized,[9] and well-known reaction models have been proposed. Due to the hazards and cost associated with experimental measurements, theoretical models have been heavily used to predict the nature of thermal runaway and to guide the design of thermal runaway experiments. Within a single cell, temperature-dependent heat generation models containing a single reaction[10,11] or multiple reactions[9,12] are often used along with anisotropic thermal transport properties.[13] Lumped[14,15] as well as one [16] or multi-dimensional[17,18] models have been used to characterize thermal runaway in a single cell. It is well-known that the state-of-charge (SoC) of the cell plays a key role in determining its thermal runaway characteristics. For most of cell chemistries, cells at higher SOC exhibit severe and more catastrophic response to abuse scenarios as compared to cells at lower SOC[19]. Increase in SOC increases the number of gases vented out of the cell and explosion limits during thermal runaway onset and propagation[20]. This not only increases the amount of energy released from the cell but also increases the critical spacing distance for both vertical and horizontal thermal runaway propagation[21].

In the context of a battery pack comprising multiple cells, the propagation of thermal runaway from one cell to its neighbors is an important problem because such propagation can destroy the entire pack. Propagation of thermal runaway may occur due to multiple non-linear and often highly coupled transport processes, including thermal conduction through the interstitial material,[18] radiation heat transfer,[22] thermal advection due to hot venting gases from a ruptured cell [23] and combustion of volatile gases ejecting from the cell.[24] Accordingly, some of the key aspects that determine whether propagation occurs or not include the rupture location, whether the vent gases catch fire,[24] the nature of interstitial material, including the material of the partition sleeves commonly used for packing cells[22] and the cell-to-cell gap in the battery pack.[25] The impact of each of these aspects on thermal runaway propagation has been studied in the past. Several aspects of the underlying transport processes make the modeling of thermal runaway propagation in a battery pack a computationally challenging task. For example, around the onset of thermal runaway, the extremely large heat release rate and temperature rise requires very small-time steps, which significantly slows down simulations. Further, high speed often supersonic turbulent flow of vent gases,[26] combustion of multiple vent gases[24] and radiation[22] each of which are non-linear by themselves when combined result in an extremely difficult simulation problem. Therefore, the number of cells considered in such simulations is often limited to only a few, whereas practical battery packs often contain thousands of cells, and the number of cells during storage and transportation may be even greater. Optimizing and reducing the computational burden remains an important challenge[27] in order to produce simulations that can be conveniently used as design tools.

While the literature cited above covers thermal runaway in a single cell and propagation within a small pack of cells, there is only limited literature available on very large Electric Vehicle (EV) modules or pallets containing many small-sized cells during storage and transportation. Rigorous fire test methods[28] have identified a direct relationship between state of charge of the cell and catastrophic fire behavior in such scenarios. Studies have shown that the maximum value for heat of combustion can be as high as 18 MJ with heat release rate as high as 49.4 kW.[29] As a result, steps to retard fire propagation are largely implemented at both small scale by adding flame retardant additives,[30] separators[31] and at large scale by implementing fire suppression mechanisms in large storage/transportation facilities.[32,33] Simulation models involving fire onset and propagation are computationally expensive.[34] A recent work has presented simulation of thermal runaway related fire in a battery storage facility [33]. However, the modeling of chemical kinetics related to thermal runaway was empirical rather than physics-based in this work, thereby limiting its applicability for studying other battery fire scenarios. While the sub modeling technique has been used for modeling thermal management of a pack containing thousands of cells,[35] this technique is limited only to linear processes and will not work well in modeling thermal runaway. There is clearly a need for understanding the large-scale propagation of thermal runaway and fire in such energy storage systems. In doing so, it may be necessary to sacrifice small-scale details, such as at the length scale of electrodes within each cell, or even cells themselves in order to execute such simulations within a reasonable time. Such simulations may contribute towards ensuring the safety of the storage and transportation processes.

This work presents a numerical simulations-based investigation of large-scale thermal runaway propagation during large-scale storage or transportation of Li-ion batteries. The model captures thermal runaway onset and fire due to combustion of vent gases and predicts the transient temperature field in proximity of pallets containing many cells. The model is used to understand the parameters that affect thermal runaway propagation and potential techniques for fire suppression.

6.1 Simulation set up

6.1.1. Geometry and General Modeling Framework

Figure 1 shows a schematic of the simulation geometry that comprises two pallets of 18650 Li-ion cells kept next to each other in a large storage facility. Each pallet contains one hundred 18650 NCA Li-ion cells arranged in a 10 × 10 array. The goal of the simulations is to understand the outcome of thermal abuse of one of the pallets, referred to as the trigger pallet. Specifically, it is of interest to determine the resulting temperature field in the storage facility and specifically predict whether propagation of thermal runaway and fire occurs to the adjacent pallet or not.

There are several computational challenges associated with such a simulation. Firstly, the length scales in this problem range across multiple orders, from the thin electrode layers within each layer that generate heat to the length scale of the storage facility itself. This multiscale nature of the problem makes it computationally very expensive to model the fine geometrical details while also modeling larger length scales. To address this, the geometrical details of each cell are ignored, and each pallet is assumed to have the same thermal properties as individual cells. Crucially, the temperature-dependent heat generation due to decomposition reactions in the cells that is ultimately responsible for thermal runaway is preserved in its original form within each pallet, and so is the anisotropic thermal conduction within the pallet. While this lumping may introduce some computational errors, if executed properly, it offers a reasonable compromise between accuracy and computational cost, as evidenced by its use in several past papers on computational modeling of large multiscale systems[35,36].

Further complications arise in this problem from the several non-linear phenomena relevant to this problem that are also highly coupled with each other. These include combustion, turbulent flow, and radiative heat transfer. Details of the physics models for these processes are discussed in subsequent sub-sections. Key computational and meshing challenges in this work are also discussed.

6.2. Governing Equations

6.2.1 Abuse model and vent gas generation

The four-equation thermal abuse model for a Li-ion cell presented by Hatchard and Kim,[9] which has been empirically lumped to a one-step reaction model by Kim, et al.[11] is used in this work. The rate of reaction is defined by

$$\frac{d\alpha}{dt} = -A \cdot \alpha^{m} \cdot (1-\alpha)^{n} \cdot \exp\left(\frac{-E_a}{RT}\right) \cdot \exp(B \cdot \alpha) \tag{1}$$

where A is the frequency factor, E_a is the activation energy, R is the universal gas constant and m, n and b are predefined reaction constants. The values of abuse reaction parameters used in equation 1 correspond to NCA 18650 cells at 25% SOC[11] and are tabulated in Table 1. Following equation (1), the source term for the energy equation is given by

$$Q_{abuse} = H \cdot \frac{d\alpha}{dt} \tag{3}$$

where H is the specific heat release.

The initial temperature of trigger pallet is 500 °C, which initiates the decomposition reactions. As time passes, the adjacent pallet experiences thermal abuse by virtue of heat released due to combustion of vent gases from the trigger pallet. Due to large size of simulation domain and computational constraints, specific details of each material inside a cell are not modeled. Each pallet is considered thermally lumped. These assumptions are necessary due to the large scale of the overall geometry. Temperature rise in each pallet is calculated using lumped energy equation as follows:

$$Q = M \cdot C_p \cdot \frac{dT}{dt} \tag{2}$$

It is assumed that gases are generated in proportion to the rate of abuse reaction. M is the mass of gases generated during combustion which plays a crucial role in total heat release calculation using equation (2). Equations governing the generation of gases from the pallet are given by

$$M_{cell} = x \cdot M_{gas} + (1 - x) \cdot M_{residue} \tag{4}$$

$$\frac{dM_{gen,total}}{dt} = x \cdot W \cdot \frac{d\alpha}{dt} \tag{5}$$

$$\frac{dM_{gen,species}}{dt} = Y_{species} \cdot M_{gen,total} \tag{6}$$

where x is the mass fraction of the cell changing to gas, W is the active material content and $x \cdot W$ is the specific content of the gas. $Y_{species}$ refers to the experimentally determined mass fraction. These volatile gases ignite once ignition temperature is surpassed. Once the gases are generated, the isotropic diffusion model given by Fick's law governs the diffusion of gases into the free stream. Depending on simulation conditions, the heat sinking effect of the adjacent pallet may be overwhelmed by the thermal runaway heat generation in the trigger pallet. Based on past work, gaseous species involved in the combustion are take to be H_2, CO_2, CO, CH_4, C_2H_4 and C_2H_6 respectively.[5] Mean mass fractions for these species for NCA type 18650 Li-ion cell are widely available. Also, based on past experimental work, it is assumed that 1% of the total cell mass converts to soot.[37] Total mass of a single 18650 cell is taken to be 45 grams.

Boundary surfaces of the simulation geometry are open to atmosphere, except the floor, in order to realistically capture combustion in large storage facilities. Open boundaries allow flow of gases and heat out of the simulation domain.

6.2.2 Impact of SoC

Since the state-of-charge (SoC) of the cell determines its energy storage, therefore, the SoC is likely to play a key role in determining its thermal runaway characteristics. With the increase in SOC, total heat release, total mass loss and the severity of ejection increases[20]. These adverse characteristics not only make cell more vulnerable to environmental pressure but also enhance the probability of cascade and fire propagation[21]. Increase in SOC increases the availability of lithium in the anode which react with electrolytes after SEI decomposition to generate more flammable gases. This further leads to increase in specific combustion heat of gases during venting thus, increasing the severity of combustion Arrhenius kinetic parameters for different SoCs are determined from curve-fitting the experimental data[38] and are described in detail in the past work[11].

6.2.3. Governing equations in the free stream

LES turbulence model[39] is used in these simulations to model the buoyant fumes and low Mach number flow of species undergoing combustion. This model significantly reduces computational cost of the simulation due to direct computation of large-scale motion in the flow. Conservation of mass in the flow field, species conservation in the flow field, variation of momentum and conservation of energy in the free stream are modeled as follows

$$\frac{\partial \rho}{\partial t} + \nabla \cdot (\rho \cdot V) = \frac{dm'''}{dt} \tag{7}$$

$$\frac{\partial(\rho \cdot Y_{\text{species}})}{dt} + \nabla \cdot \left(\rho \cdot Y_{\text{species}} \cdot V\right) = \nabla\left(\rho \cdot D_{\text{species}} \cdot \nabla \cdot Y_{\text{species}}\right) + \frac{dM_{\text{chem}}}{dt} + \frac{dM_{\text{evap}}}{dt} \tag{8}$$

$$\frac{\partial(\rho \cdot V)}{dt} + \nabla \cdot (\rho \cdot V \cdot V) = -\nabla P_{\text{pr}} - \nabla\tau + (\rho - \rho_o)g + S_p + S_{evap} \tag{9}$$

$$\frac{\partial(\rho \cdot h_s)}{\partial t} + \nabla \cdot (\rho \cdot h_s \cdot V) = \frac{DP}{Dt} + \frac{dQ'''_{\text{release}}}{dt} - \nabla \cdot Q''_{\text{flow}} \tag{10}$$

Description of variables appearing in equations above is provided in Table 2.

6.2.4. Finite rate combustion

A mixing-controlled combustion model with infinite reaction rate is used to model heat generation during to combustion, including consumption of reactants during thermal runaway onset and propagation. In order to accurately model change in concentration of volatile species, the rate of combustion is considered to be a function of both temperature and concentration. An Arrhenius finite rate kinetics based single-step reaction model is used. Reaction parameters for finite rate combustion of various species are summarized in Table 3. Equations defining single step combustion are as follows:

$$\frac{dC_s}{dt} = -k\prod C_s^{N_s} \tag{11}$$

$$k = A * T^p * e^{-Ea/RT} \tag{12}$$

Values of N_s and p is taken to be 1 and 0, respectively.[40]

6.2.5. Meshing and other simulation details

All simulations are carried out in Fire Dynamics Simulator (FDS).[41], which has been used in several past papers related to combustion and fire propagation[42–44]. Simulations involving buoyant fumes and fires usually require extremely fine discretization to achieve reasonable accuracy. In these simulation studies, a non-uniform mesh resolution is used with 0.0015 m as the largest element length to reduce total simulation time. Non uniformity is modeled in *z* direction using piecewise linear mesh transformation technique. As a result of this technique, mesh resolution is maximum in the vicinity of the pallet and reduces with height. Higher resolution results in greater number of elements covering characteristic fire length which in turn enhances numerical stability.

These simulations also use adaptive time stepping. The largest timestep is restricted at 10 ms to ensure CFL[45] and von Neumann stability criteria[46] are satisfied. Element sizes and time steps refrain these constants from achieving values greater than 0.7.

6.3. Results and discussion

Due to the highly non-linear nature of various processes associated with thermal runaway propagation that are being accounted for in the simulation model, it is important to first establish the accuracy of the computational model. Specifically, it must be verified that the computed results are not influenced by the grid size and/or the timestep used in simulations. To do so, a representative thermal runaway and fire propagation simulation is carried out. This simulation comprises two pallets with a distance 0.8 m between the two pallets. Dimensions of each pallet is assumed to be 0.184 m × 0.184 m × 0.069 m. Each pallet is assumed to contain one hundred 18650 NCA Li-ion cells arranged in a 10 × 10 array with no cell-to-cell gap. The array of cells is wrapped in a 2 mm thick polyethylene sheet from all sides. Length, width and height of the storage room are assumed to be 3 m × 3 m × 5 m respectively. The trigger pallet is kept 0.6 m from the left boundary and 0.2 m from the front boundary, while the adjacent pallet is kept at the similar distance from front wall and 1.93 m from the right boundary of the simulation geometry. For computational simplicity and due to extremely small airgaps in the pallet, all cells in a pallet as well as the pallet material itself are lumped together and modeled as a single material in simulations. Based on past work, density and heat capacity of the material are taken to be 2280 kgm^{-3} and 715 kJkg^{-1}K^{-1} respectively.[13,47] Thermal conductivity for the pallet material is 0.2 Wm^{-1}K^{-1} in X and Y directions and 32 Wm^{-1}K^{-1} in Z direction.[13] Standard thermal properties for polyethylene are assumed.[48,49]

In order to examine the influence of the grid and timestep, simulations are carried out with a number of values of the maximum element size and maximum timestep. Keeping one of these parameters constant, the other parameter is reduced until the computed temperature field does not change significantly any more. Results are plotted in Figure 2(a) and 2(b), in which, temperature at 0.5 m height above the trigger pallet is plotted as a function of time for multiple values of the maximum element size and maximum timestep, respectively. In these plots, the maximum timestep size is fixed at 0.0015 m for Figure 2(a) and maximum element size is fixed at 0.01 s for Figure 2(b). These results show that the temperature field changes somewhat when these parameters are changed, but becomes largely independent when the maximum element size is around 1.5 mm or lower, and the maximum timestep is 10 ms or lower. Given the large physical size of the room and the long time period of interest, both of these are relatively small numbers, implying the considerable computational cost associated with these simulations. The very tight computational constraints needed to ensure grid- and timestep-independence is, however, not surprising, given the highly non-linear nature of combustion, turbulent flow as well as Arrhenius heat generation in this problem.

All further simulations discussed in this work are carried out with a maximum element size of 1.5 mm and a timestep of 10 ms.

In general, it is always desirable to validate a numerical computation framework, such as the one used in this work, by comparison with experimental measurements. Unfortunately, in the present case, there is a lack of sufficient experimental measurements on battery thermal runaway and fire propagation at the large length scales considered in this work. Therefore, a limited comparison of the present numerical framework with a previously reported experimental measurement on a single Li-ion cell[12] is carried out. Despite the smaller length scale involved in this comparison, this exercise helps establish the fundamental capability of the numerical computation framework to capture the key features of a thermal runaway event.

This comparison pertains to a thermal abuse measurement on a single 18650 cell in a fire calorimeter.. Experimental measurement captures surface temperature of a single 18650 NCA cathode type cell at 75% SoC. During a fire test using cone calorimetry. External heating through

0.6kw ceramic heater acts as he triggering factor to push cell into thermal runaway in well ventilated test chamber measuring 1.1m x 1.1 m by 1.4 m.The conditions of this experiment are numerically simulated in the FDS computational framework, using the same governing equations as the rest of this work. All parameters, such as geometry and kinetics parameters of the cell are selected to match the conditions specified in the past experimental measurement[12]. A comparison of measured surface temperature as a function of time with predictions from the numerical simulations is presented in Figure 3. Arrhenius kinetic parameters for single reaction thermal runaway model at 75% SoC are approximated based on 50% and 100% SoC data. Numerically obtained surface temperature plot in Figure 1 stands in reasonable agreement with the measured experimental data[12]. Note that both experimental measurements and numerical simulations present some noise, mainly due to measurement and data acquisition noise in the experiment and the non-linear nature of the equations being solved in the simulation model. Nevertheless, Figure 3 clearly shows very good agreement between the two both in terms of the time at which thermal runaway onset occurs, as well as the steep temperature rise and peak temperature attained during thermal runaway.

Despite the limited nature of the validation carried out here, mainly due to lack of sufficient experimental data at the length scale of interest, nevertheless, the comparison establishes the capability of the numerical simulation framework to capture the thermal runaway phenomenon. Other papers in the past have also used FDS simulation framework to simulate fires originating from batteries and other sources[42–44] which further enhances the confidence in the present simulation framework.

Figure 4 presents colorplots of the temperature field in a cross-section plane of the geometry at multiple times for a representative thermal runaway propagation scenario. For this simulation, the distance between trigger pallet and adjacent pallet is 0.6 m. Single step abuse reaction model coupled with LES combustion model is implemented. Walls and ceiling of the simulation geometry are open to atmosphere. This mimics realistic fire propagation in a large storage facility where the concentration of oxygen is extremely large compared to concentration of reactants. The colorplots in Figure 4 show the trigger pallet (on the left) catch fire almost immediately. As time passes, heat transfer to the neighboring pallet causes its temperature to rise as well, eventually resulting in thermal runaway in the neighboring pallet as well. In Figure 4(b), total heat release rate is plotted along with a soot density color plot to show fire propagation. These quantities are plotted based on the combustion of volatile gases released during thermal runaway as well as the pallet material.

The temperature data in colorplots in Figure 4 can be plotted in order to provide a more comprehensive visualization of the temperature field over space and time. Figure 5(a) plots temperature as a function of time at multiple locations above the trigger pallet for the set of conditions considered in Figure 4. As expected, the highest temperature is encountered closest to the trigger pallet. Over time, temperature at each location first increases sharply due to rapid heat release during the thermal runaway process. After reaching a peak, the temperature then gradually comes down over a long period as the reactants are slowly consumed. A minor bump in the temperature curves around *t*=500 s is associated with heat received from combustion of the neighboring pallet, which has a lag compared to combustion of the trigger pallet.

Figure 5(b) plots temperature distributions above the trigger pallet at multiple times. The first curve shown, at *t*=200 s, is close to the peak of fire in the trigger pallet, and, therefore, is the highest. Afterwards, the temperature field cools down as reactants get consumed. At each time, there is a gradual reduction in temperature as the vertical distance from the trigger pallet increases.

A similar plot of temperature as a function of time and space above the adjacent pallet is presented in Figure 6. Figures 6(a) and 6(b) plot temperature as a function of time at multiple locations above the adjacent pallet, and as a function of distance away from the adjacent pallet at multiple times, respectively. Figure 6(a) shows a short period of no temperature rise above the adjacent pallet, followed by a large rise in temperature, and, finally, a gradual reduction. This short initial period corresponds to when the trigger pallet is on fire, but the fire has not yet spread to the adjacent pallet. Once the adjacent pallet catches fire, Figure 6(a) shows a sharp temperature rise, which lasts until the peak of combustion of the adjacent pallet. Afterwards, similar to the trigger pallet shown in Figure 5(a), there is also a gradual reduction in the temperature field above the adjacent pallet. The spatial temperature distribution above the adjacent pallet at multiple times shown in Figure 6(b) is somewhat more complicated than that above the trigger pallet because it is influenced by the time lag between fire in the trigger pallet and in the adjacent pallet. Each curve in Figure 6(b) goes up, then down, which corresponds to the location of the flame. The temperature is the largest at the flame, and is lower both below and above the flame. As shown in these curves, the location of peak, i.e., the flame, reduces as time passes, which corresponds to the burnout of the flame once the reactants are consumed. It is interesting to note that the surface temperature of the adjacent pallet remains nearly constant. The small non-monotonicity of the surface temperature is explainable because the surface temperature first increases up to a certain time, and then reduces once the reactants begin to be consumed.

The State-of-Charge of a Li-ion cell plays a key role in determining its thermal runaway characteristics, and, therefore, is of much practical interest. For example, the ideal SoC of cells during long-term storage or transportation has been widely debated[20,21]. Due to the practical importance of SoC, a number of simulations are carried out to characterize the role of SoC on the onset and propagation of fire from one pallet to another.

As described in Section 2.2.2, the effect of SoC is modeled in this work on the basis of previously reported values at different SoCs of activation energy and other kinetics parameters related to the thermal runaway reactions[11]. Data corresponding to NCA chemistry are used. Based on this, a number of simulations at three different SoCs (25%, 50% and 100%) are carried out. Figure 7 presents plots of heat release rate as a function of time for a single pallet of cells undergoing thermal runaway for these values of SoC. As expected, the greater the SoC, the larger is the heat release rate, which is mainly due to greater energy content at higher SoC.

The greater heat release rate at higher SoC shown in Figure 7 is expected to result in faster onset of thermal runaway and possibly greater temperature rise. This is confirmed by determining the temperature distribution in and around the trigger pallet for each SoC considered in Figure 7. Figure 8(a) presents temperature colorplots at *t*=400 s for each SoC, whereas Figure 8(b) plots temperature 1.0 m above the surface of the trigger pallet as a function for time for each SoC. As expected, thermal runaway is faster and more vigorous for the 100% SOC case, and there is propagation of thermal runaway to the adjacent pallet. The effect of SOC and pallet-to-pallet gap on thermal runaway propagation is analyzed in more detail in the next sub-section.

A key geometrical parameter of much practical relevance in this problem is the distance between adjacent pallets. Space is often limited in both storage and transportation of cells, and, therefore, in general, it is desirable to pack the battery pallets as close as possible to each other in order to increase the packing density. However, placing the pallets too close to each may increase heat transfer between adjacent cells, resulting in greater likelihood of propagation of thermal runaway from a trigger pallet to its neighbor.

In order to evaluate this interesting and important trade-off, temperature and fire color plots for a case with a large 0.8 m gap are plotted in Figure 9. Compared to the baseline case of 0.6 m gap shown in Figure 4, these colorplots clearly show that the larger gap results in the fire remaining isolated to only the trigger pallet. While the temperature field above the trigger pallet shown in Figure 9(a) is similar to the 0.6 m gap case, there is clearly no propagation of fire to the adjacent pallet as the pallet-to-pallet gap is too large for the fire to jump. This results in the impact of fire remaining somewhat isolated. This shows that the pallet-to-pallet gap plays a key role in determining the nature of fire in the storage facility. While on one hand, it may be desirable to reduce the pallet-to-pallet gap for more efficient packing, on the other hand, simulations presented here clearly show that a small pallet-to-pallet gap may risk the propagation of thermal runaway and fire from one pallet to the other.

In order to further illustrate the impact of pallet-to-pallet gap on thermal runaway and fire propagation, a number of simulations are carried out with different values of the gap between the trigger pallet and adjacent pallet, while keeping all other parameters fixed. Results are summarized in Figure 10, where temperature at the surface of the adjacent pallet is plotted as a function of time for multiple values of the gap between the two pallets. It is found that for very small values of the gap, propagation of thermal runaway to the adjacent cell occurs very quickly, due to which, a rapid rise in temperature occurs, as shown in Figure 10. As the value of the gap increases, propagation of thermal runaway still occurs, but with an increasing time delay. Eventually, at a cut-off value of the gap, there is a sudden change in the thermal runaway propagation characteristics of the system, so that for gaps beyond the cut-off value, there is no propagation of thermal runaway at all. There is still a minor increase in temperature in the adjacent pallet, but it is insufficient to initiate or sustain thermal runaway. For the parameter values considered here, Figure 10 shows that the threshold value of the pallet-to-pallet gap is around 0.8 m.

Another interesting way to visualize the impact of pallet-to-pallet gap on thermal runaway propagation is to plot t_{prop}, the time taken for propagation as a function of the pallet-to-pallet gap. This is plotted in Figure 11, where the y axis represents the reciprocal of the time taken for propagation. This curve dips downwards as the gap increases, indicating a gradual increase in the time taken for propagation, until the cut-off value of the gap is reached. Beyond this cut-off, the curve abruptly drops to zero, indicating that there is no propagation of thermal runaway at all when the gap is greater than the cut-off value.

The existence of a sharp cut-off value of the gap has significant implications in the design of large-scale storage and transportation systems for Li-ion cells. The gap between pallets must clearly be kept above the cut-off gap because placing the pallets even slightly closer than dictated by the cut-off value results in a significant risk for thermal runaway propagation. If the current design of a storage facility has a pallet-to-pallet gap that is just below the threshold predicted by the simulations, it may be helpful to increase the gap slightly in order to go above the threshold and significantly improve safety with only an incremental impact on storage density.

Note that the cut-off value of the gap identified by Figures 9 and 10 above is specific to the cell chemistry, pallet size, number of cells and other parameter values assumed in these simulations. For example, if the energy density of the pallet increases, the cut-off gap will likely grow as well due to greater heat released during thermal runaway. This will necessitate placing the pallets with greater gap.

While Section 3.4 investigated the impact of SoC mainly on the onset of thermal runaway, it is also of interest to determine how the SoC of cells in the pallet affects the propagation of thermal runaway and fire from the trigger pallet to its neighbors. This is of much practical interest, since thermal runaway and fire limited to a single pallet, while not desirable, is a lot more acceptable than the other storage facility catching fire. Numerical simulations similar to those described in Section 3.5 are carried out at three different values of the SoC (25%, 50% and 100%). In each case, the pallet-to-pallet gap is kept fixed at 0.8 m. Figure 12 presents plots of temperature on the surface of the adjacent pallet as a function of time for each SoC considered here. It is found that there is clearly propagation of thermal runaway and fire from the trigger pallet to adjacent pallet in the 100% SoC case. In contrast, the 50% and 25% SoC cases do not involve propagation, and while the trigger pallet undergoes thermal runaway, there is no spread of fire to the adjacent pallet. This is an important practical insight that may influence the design of SoC of cells under large-scale storage and/or transportation.

List of figures

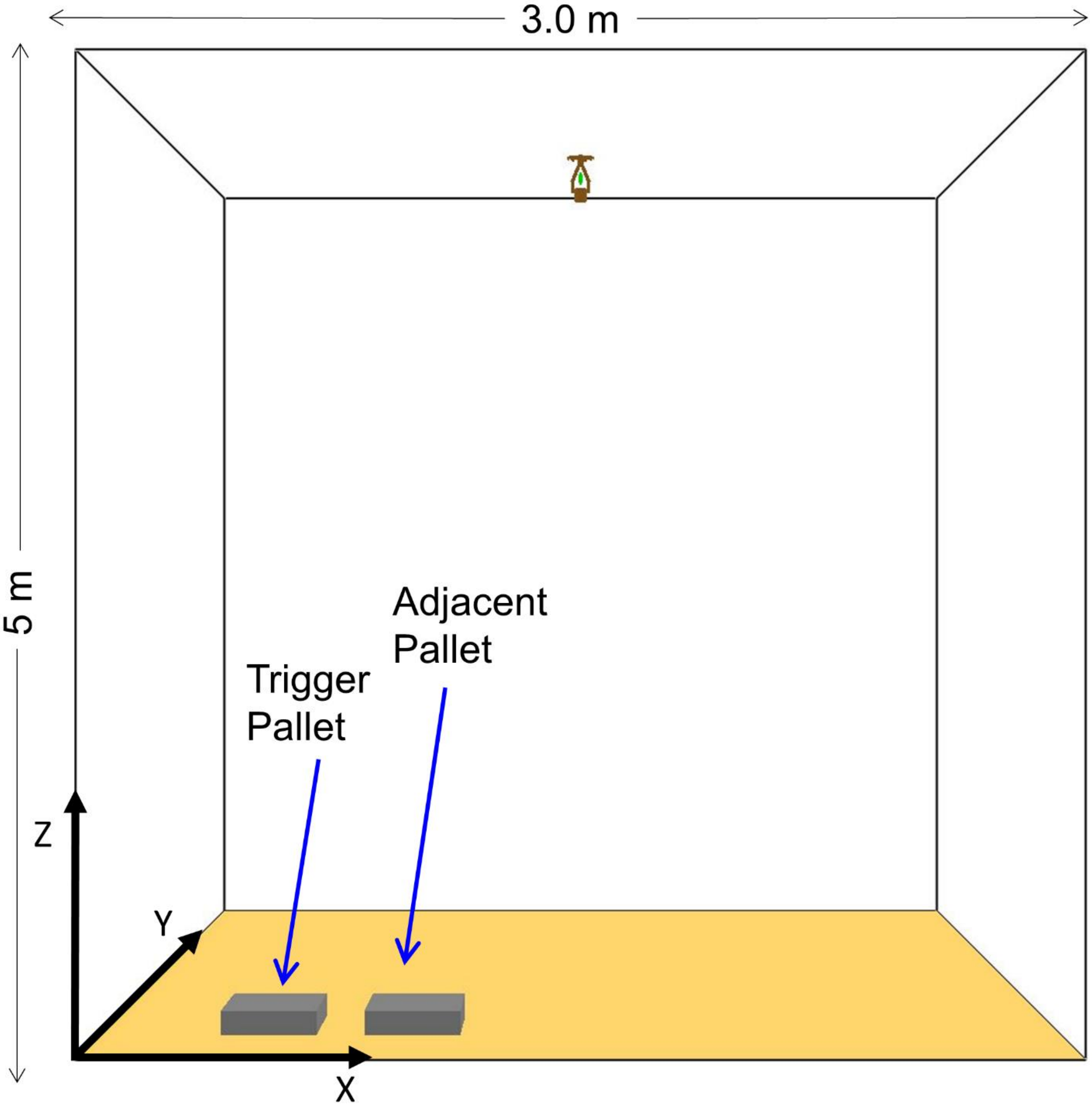

Figure 1: Schematic of two 0.184 m × 0.184 m × 0.069 m pallets containing 18650 Li-ion battery packs kept in a storage facility showing overall simulation geometry showing the trigger and adjacent pallet.

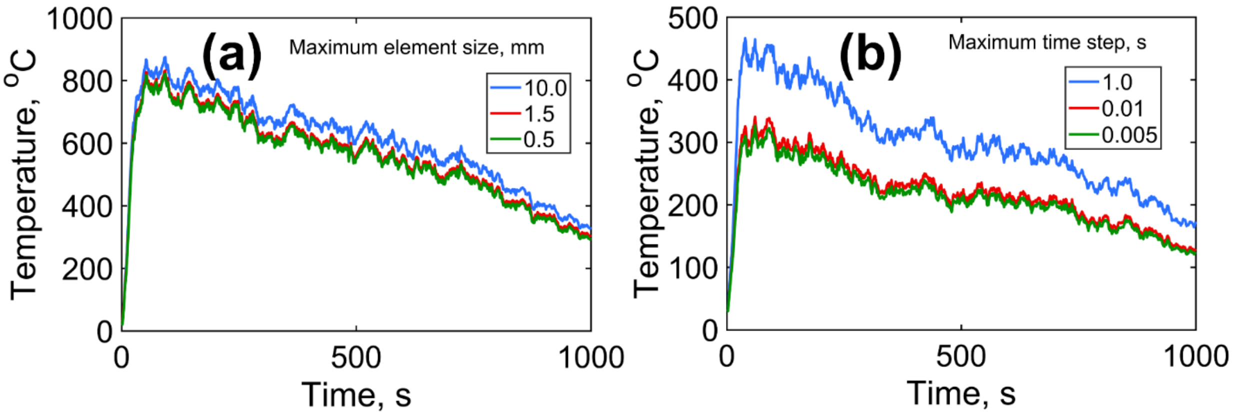

Figure 2: Simulation results to establish mesh and time sensitivity: Temperature vs time plot at 0.5 m height from the trigger pallet for (a) different element sizes and (b) for different maximum timestep bound in adaptive time stepping. Maximum timestep for (a) is 0.01 s and element size for (b) is 0.0015 m.

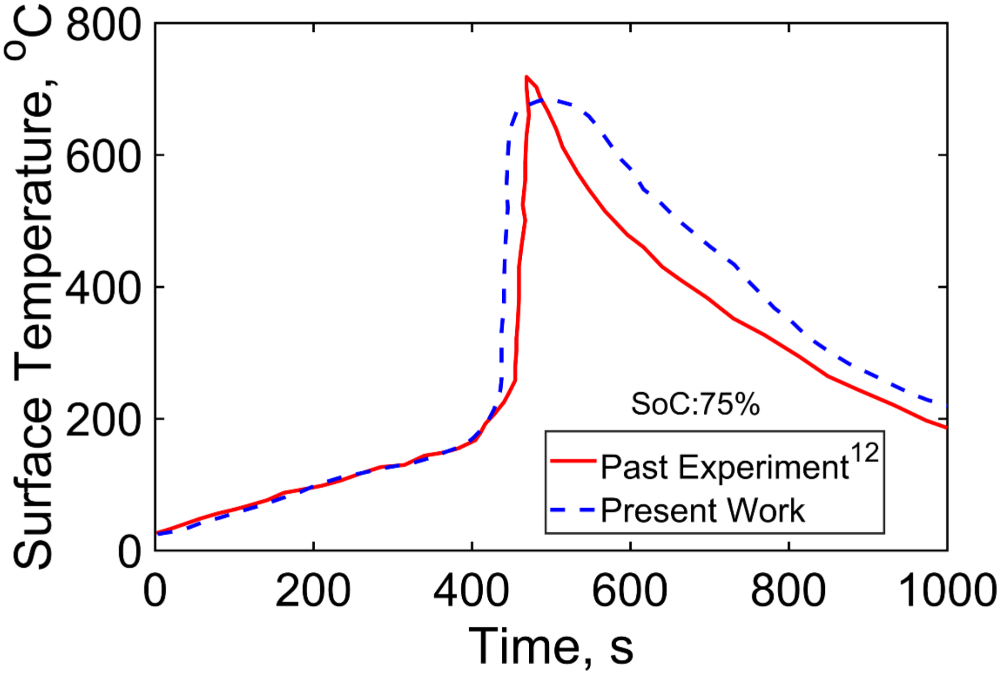

Figure 3: Temperature as a function of time for single NCA cathode type 18650 cell undergoing thermal runaway at different SOC.

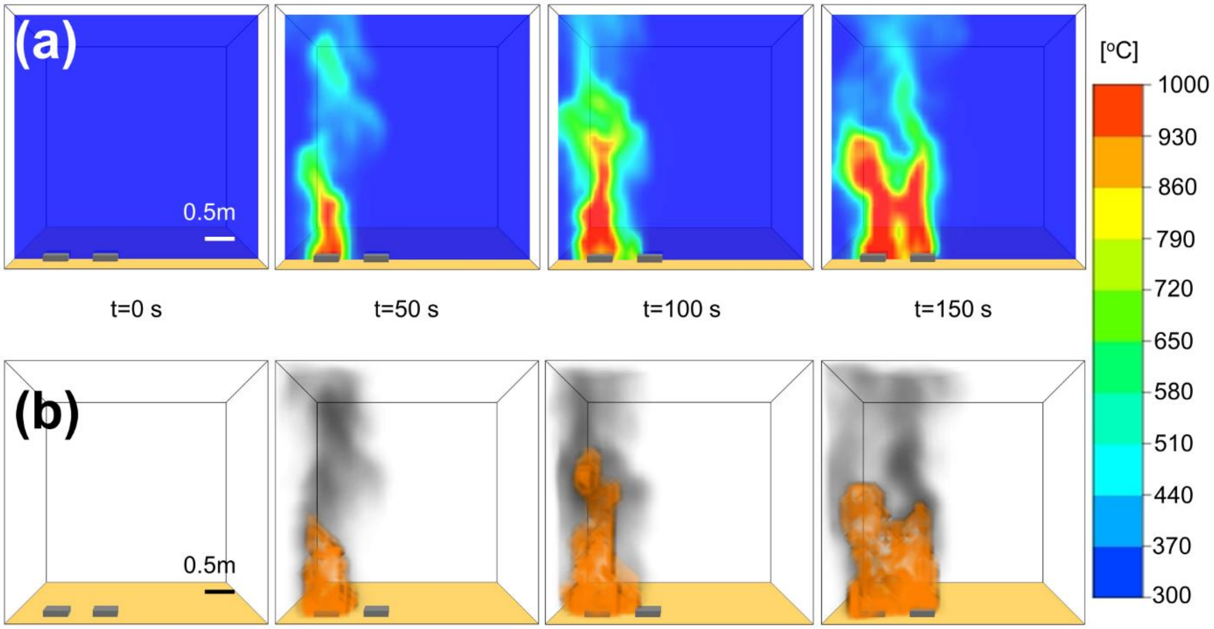

Figure 4: (a) Temperature and (b) fire propagation color plots for the case of 0.6 m distance between trigger and adjacent pallets resulting in fire propagation.

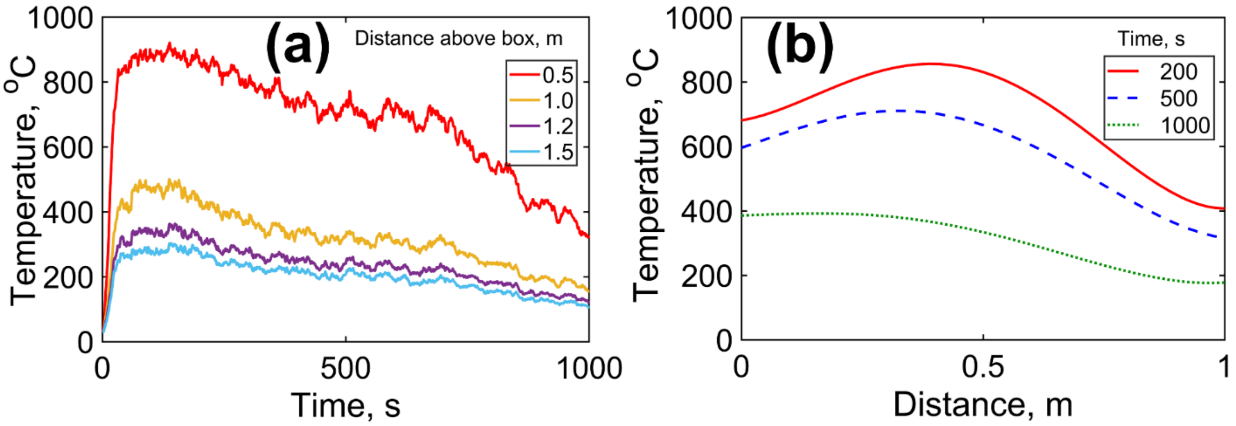

Figure 5: Temperature plots above the trigger pallet: (a) Temperature as a function of time at different heights above the trigger pallet, and (b) temperature as a function of distance above the trigger pallet at multiple times.

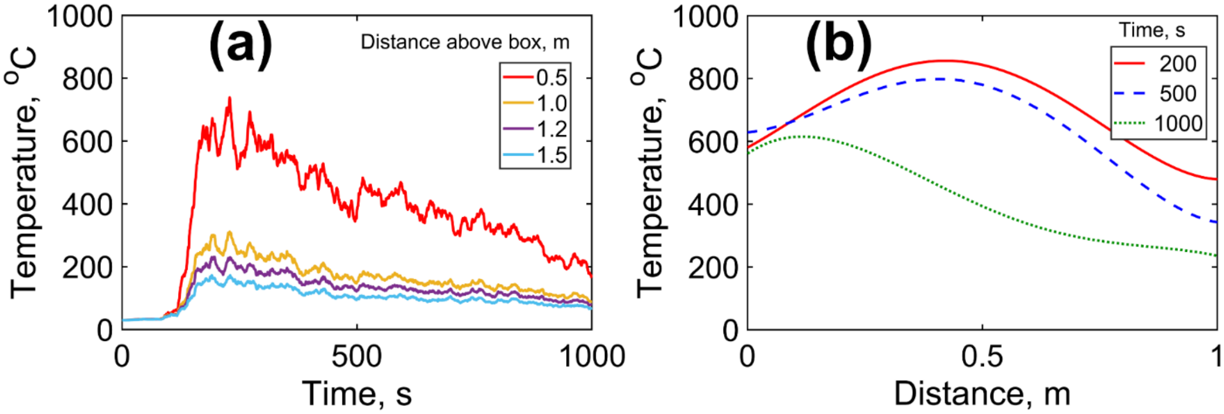

Figure 6: Temperature plots above the adjacent pallet: (a) Temperature as a function of time at different heights above the adjacent pallet, and (b) temperature as a function of distance above the adjacent pallet at multiple times.

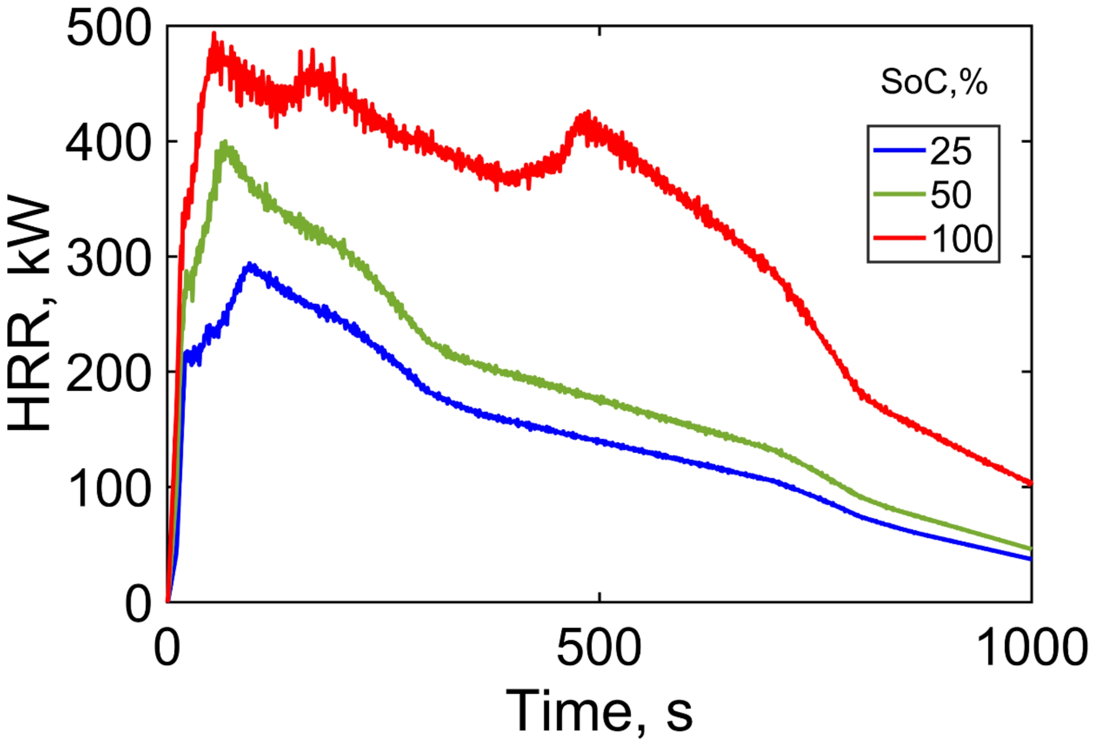

Figure 7: Total heat release rate plot as a function of time for trigger pallet undergoing thermal runaway at different SOC.

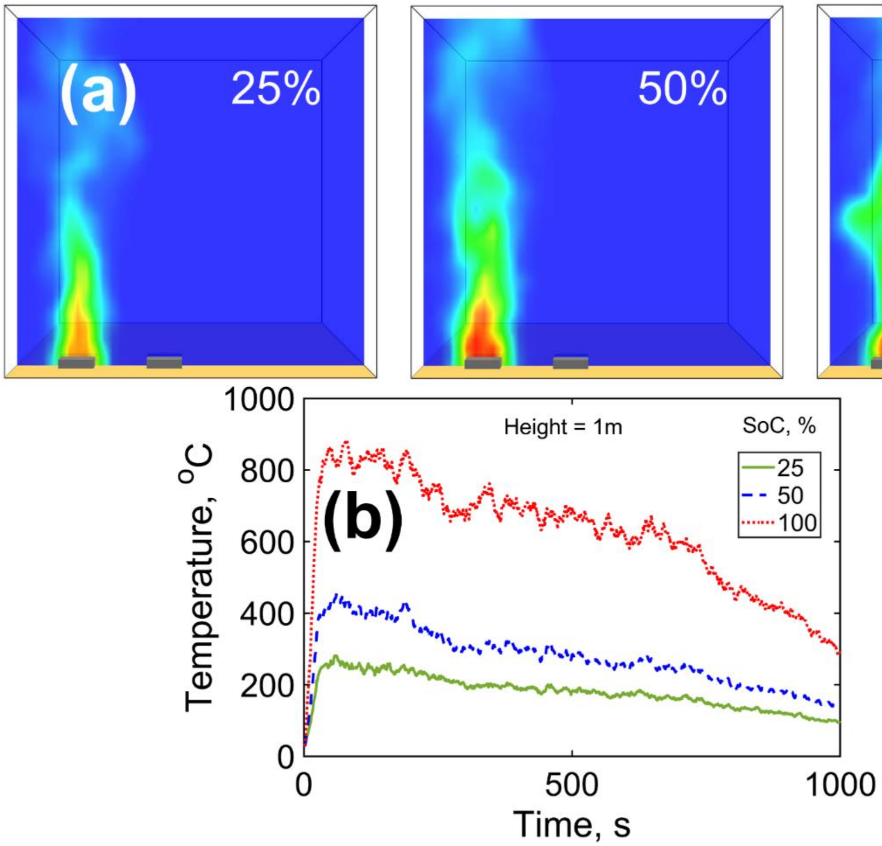

Figure 8: (a) Temperature propagation color plots for the case of 0.8 m distance between trigger and adjacent pallet at different SOC at 400 s and (b) Temperature as a function of SoC at 1m height above trigger pallet.

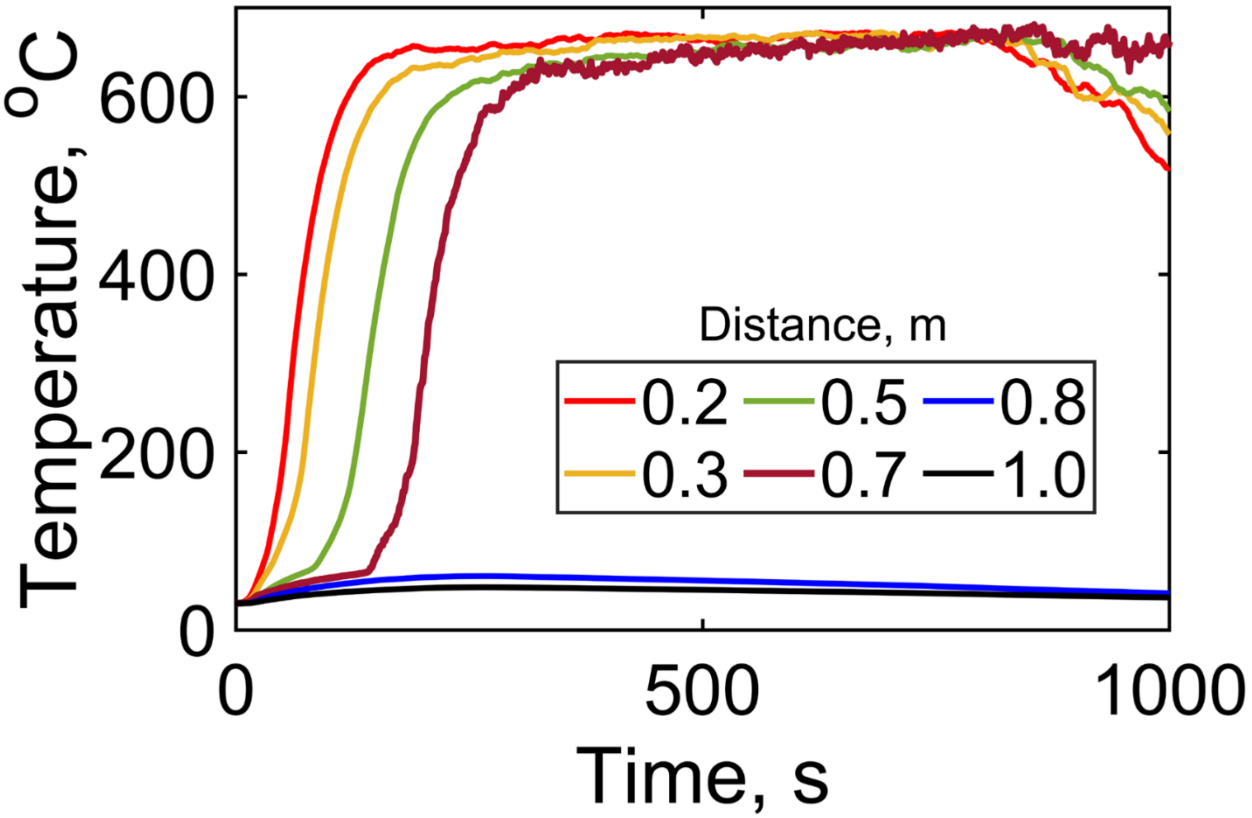

Figure 9. Peak temperature at the top surface of the adjacent pallet as a function of time for different values of distance between trigger and adjacent pallets.

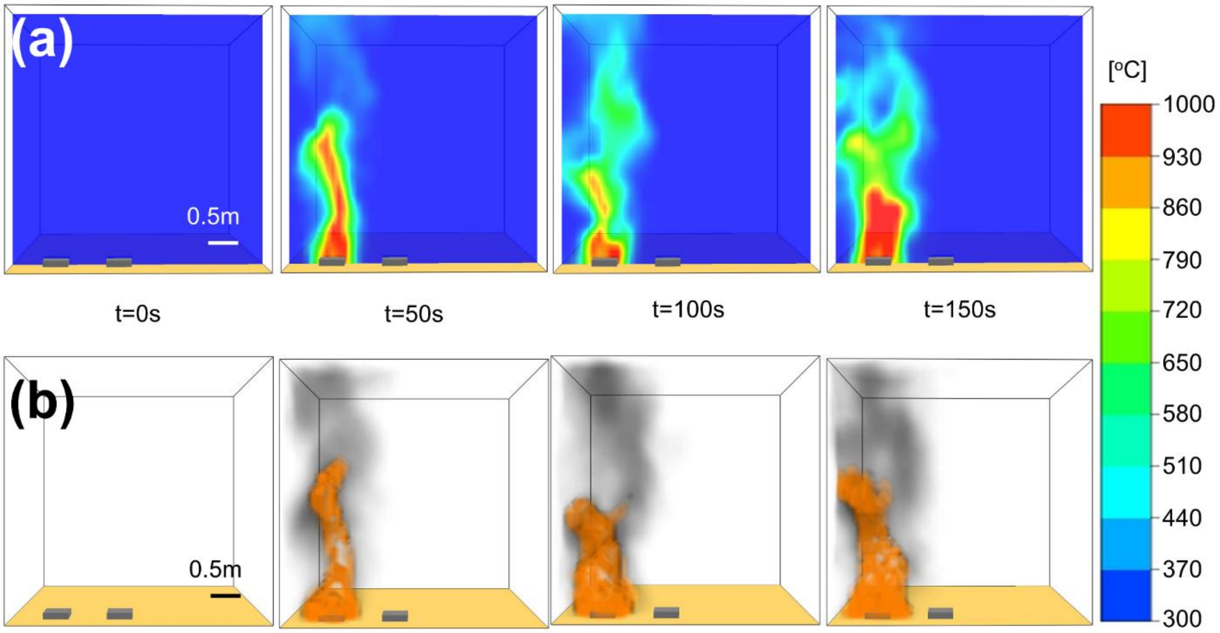

Figure 10. (a) Temperature and (b) fire propagation color plots for the case of 0.8 m distance between trigger and adjacent pallets, resulting in no propagation of fire.

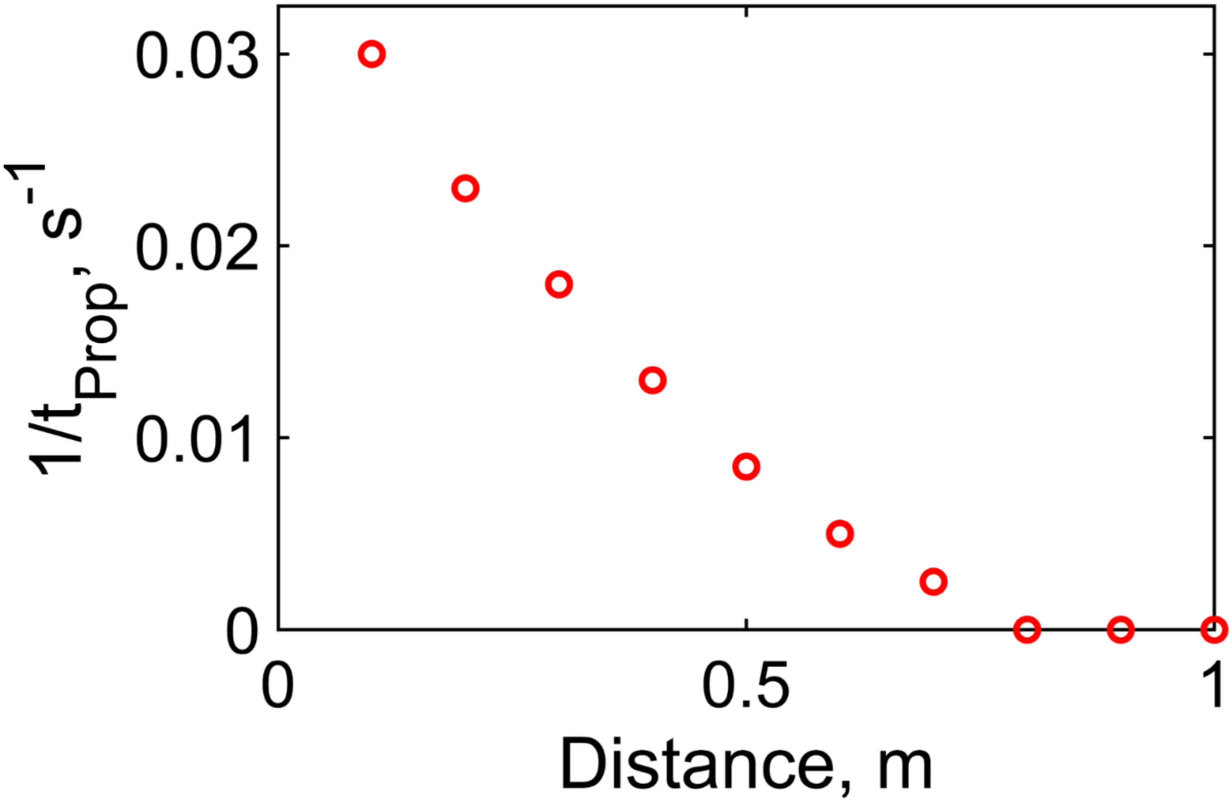

Figure 11. Reciprocal of time taken for fire propagation to adjacent pallet as a function of distance between trigger pallet and adjacent pallet.

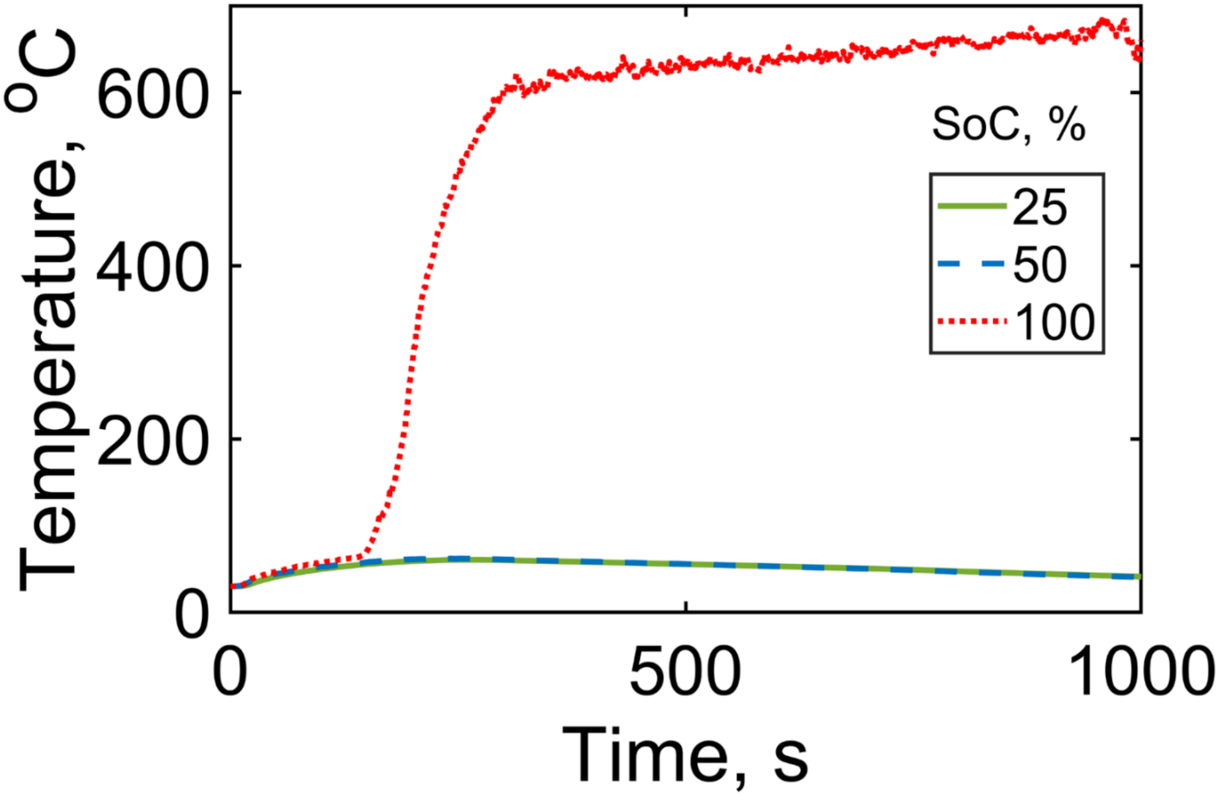

Figure 12. Temperature at the surface of adjacent pallet kept at 0.8 m from the trigger pallet at different SoC for NCA 18650 cells.

CONCLUSIONS

The onset and propagation of thermal runaway involves multiple non-linear thermal processes. It is important to develop a systematic simulation framework to account for these processes and their interactions with each other, in order to ultimately be able to accurately predict whether thermal runaway propagation will occur or not. This work shows that cell-to-cell gap and thermal conductivity of the interstitial medium both play a key role in determining the nature of thermal runaway in the battery pack. While a large value of the cell-to-cell gap may help prevent propagation, it also reduces the energy storage density of the battery pack. In different thermal abuse scenarios, both very low and very high values of thermal conductivity are found to be undesirable, with an intermediate range being the most desirable. The effect of location of the trigger cell within the pack is also investigated, and it is found that either the center or the corner location may be desirable, depending on the nature of thermal abuse. Further, results related to the effect of neglecting radiation or natural convection clearly show that these effects must be properly accounted for in order to ensure accuracy of the simulation. It is expected that the results discussed here may be helpful for practical thermal design of the battery pack, as well as for the developing practical thermal simulation tools for battery packs.

The simulation of venting gas ejecting from a ruptured Li-ion cell in a battery pack presents several technical difficulties. The vent gas flow is supersonic and turbulent. The resulting conservation equations are highly non-linear. Moreover, the key boundary conditions including temperature and flowrate at the vent are not well known. This work addresses these challenges by first estimating the vent gas temperature and flowrate as it exits the trigger cell based on isentropic flow assumption. Further, a multi-physics simulation framework is developed to predict the resulting thermal and fluid flow fields in the battery pack. This helps predict how the vent gas transfers thermal energy to neighboring cells, which may cause propagation of thermal runaway. The impact of geometrical parameters such as cell-to-cell gap, overhead gap as well as the location of the vent hole (top surface vs side wall) on thermal runaway propagation predicted by this model may be of much practical interest. Note that the results presented in this work are based on previously-reported stagnation pressure measurements underlying the calculation of temperature and flow boundary conditions, which may vary significantly from one abuse condition to the other. The impact of cell capacity and SOC is also not captured in the present model. Another limitation of the present work is that only venting from the trigger cell is considered. Secondary venting events that may occur as neighboring cell get impacted are not modeled here. Finally, the presence of solid particles in the vent gas flow has been ignored. Measurements and modeling of solid particles in the flow, while quite challenging, is a potential direction for future work. This work addresses a key gap in the literature by developing a simulation model that predicts the spreading of venting gases in the battery pack and consequently the propagation of thermal runaway to neighboring cells. It is expected that design guidelines based on such a simulation tool may be helpful for designing battery packs that can better withstand thermal runaway propagation, resulting in more reliable electrochemical energy conversion and storage systems.

Thermal runaway is a considerably complicated phenomenon, the modeling of which presents several practical challenges. Given the non-linear nature of radiative heat transfer, it has often been neglected in past work, despite its likely importance at high temperatures reached during thermal runaway. By explicitly modeling radiative heat transfer through surface-to-surface view factors, this work highlights the importance of radiative heat transfer in determining the thermal fate of a battery pack. Specifically, it is shown that radiative properties of the internal partition walls in the battery pack may play a key role in determining whether the onset and propagation of thermal runaway occurs or not. This information may have practical applications in the thermal design of the battery pack. Radiative properties of the partition walls, such as emissivity, can be easily controlled, such as by painting the walls black. This represents a passive, low-cost thermal management approach that does not add to system weight. This work shows that heat transfer through the internal partition is particularly enhanced when the thermal conductivity of the partition is very high, such as for typical metals. However, the trade-off of increased weight must be carefully considered in the use of metal partition walls. It is important to note that the present work primarily considered thermal abuse of the cell, whereas other types of abuse that may occur, such as mechanical or electrical abuse are not accounted for. Several phenomena that may occur during thermal runaway, such as cell rupture, vapor venting, combustion and flame have also been neglected. Carrying out combined modeling of such processes each of which is highly non-linear is an important challenge in this field.

The key contribution of this work is in comprehensive modeling of combustion of vent gases during thermal runaway and the subsequent impact on thermal runaway propagation. This modeling has been carried out within a comprehensive simulations framework that accounts for multiple other non-linear phenomena such as Arrhenius heat generation, radiation and turbulent mixing. Good agreement with experimental data for a test case provides validation of the simulation approach, based on which, it is shown that combustion of vent gases is a very important process to model in studying thermal runaway propagation. It is important to note the key limitations and assumptions inherent in this work. The Reynolds-averaged Navier–Stokes (RANS) based turbulent combustion modeling cannot accurately resolve the fine reaction zone and turbulent-chemistry interaction at small length scales. In the meantime, the boundary layer at the surface of the battery can strongly affect the heat transfer process, and its separation can lead to more complexity in the flow field. Therefore, an ideal simulation would be Direct Numerical Simulation (DNS) that fully resolves flow, mixing, chemistry, heat transfer and thermal runaway. This is, however, very challenging due to the substantial computational resources needed. This work expands the fundamental understanding of combustion during thermal runaway in a Li-ion battery pack, particularly the impact of combustion on thermal runaway propagation. In addition to these fundamental insights, the results presented here are also of considerable practical importance in the thermal design and optimization of battery packs, towards preventing thermal runaway propagation. It is expected that guidelines based on this work may help improve the safety and performance of electrochemical energy conversion and storage systems.

BIOGRAPHICAL INFORMATION

Dhananjay Mishra received a Bachelor of Engineering in Mechanical Engineering from The University of Petroleum and Energy Studies. He started his Master of Engineering in Mechanical Engineering in Fall 2017 and finished in Fall 2019 from the University of Texas at Arlington (UT Arlington). Immediately after the Master of Engineering, he started his Ph.D. in Mechanical Engineering at the same university. He worked as a Risk Mitigation intern at General Motors during the spring of 2022 and Summer intern at Underwriters Laboratories during summer of 2022 . His research at UT Arlington focused on the understanding of thermal runaway fire onset and propagation. In the near future, he aspires to pursue his career in industry.

Email: dhananjay.mishra@mavs.uta.edu